AN ABSTRACT OF THE THESIS OF

Seung-Bae Kim for the degree of Doctor of Philosophy in Electrical & Computer Engineering presented on July 11, 1991.

Title: Electrical Characterization of n-Type Aluminum Gallium Arsenide

Redacted for Privacy

Abstract approved: _____

Professor John F. Wager

In this thesis, two experimental approaches are employed to investigate the nature of the DX center in Te- and Si-doped $Al_{0.3}Ga_{0.7}As$.

The first experimental investigation involves the minority carrier capture (MCC) technique which is employed, for the first time, in order to estimate the capture cross-section of holes for the DX center in Te- and Si-doped $Al_{0.3}Ga_{0.7}As$. The measured hole capture cross-sections for Te- and Si-doped $Al_{0.3}Ga_{0.7}As$ are approximately 2×10^{-19} and 1.5×10^{-17} cm^2, respectively, and are independent of temperature below ~ 70 K. The discrepancy in the magnitudes of these capture cross-section is explained in terms of multiphonon emission (MPE) theory. The magnitude and temperature-dependence of these capture cross-sections indicates that the

rate-limiting step for hole capture involves DX in a neutral charge state.

The second experimental investigation concerns optically-controlled dislocation-glide and -climb which is employed for external gettering to reduce the DX concentration in $Al_{0.3}Ga_{0.7}As$:Te device regions. Cathodo-luminescence analysis clearly indicates the formation of misfit dislocation networks due to glide after processing with an optical power density of approximately 9×10^4 W/cm^2. The DX center concentrations of optically-processed samples and samples not subjected to any optical-processing are evaluated by deep-level transient spectroscopy (DLTS), capacitance-voltage (C-V) analysis, deep-level admittance spectroscopy (DLAS), and thermally stimulated capacitance (TSCAP). DLTS analysis indicates that the DX center concentration of optically-processed samples is approximately 30% smaller than that of samples not subjected to any optical-processing. DLAS and TSCAP measurements also confirm that the DX concentration is reduced by optical-processing, although a quantitative estimate of the extent of this reduction is not possible from these measurements. Additionally, the net positive charge concentration, as measured from C-V analysis, increases by approximately 3-17% after optical-processing.

Electrical Characterization of n-Type Aluminum Gallium Arsenide

by

Seung-Bae Kim

A THESIS

submitted to

Oregon State University

in partial fulfillment of
the requirements for the
degree of

Doctor of Philosophy

Completed July 11, 1991

Commencement June 1992

APPROVED:

Redacted for Privacy

Associate Professor of Electrical and Computer Engineering

Redacted for Privacy

Head of Department of Electrical and Computer Engineering

Redacted for Privacy

Dean of Graduate School

Date thesis is presented: July 11, 1991

Typed by Seung-Bae Kim for: Seung-Bae Kim

ACKNOWLEDGEMENT

I would like to express my sincere gratitude to my my advisor, Professor John F. Wager, for the support, guidance, and encouragement he has given me throughout this work, and to Professor J. A. Van Vechten for the idea of employing optically-controlled dislocation-glide and -climb to reduce the DX concentration out of AlGaAs device region.

Special thanks to Professor S. J. T. Owen, Professor J. A. Arthur, and Professor J. R. Welty for being on my graduate committee and for providing useful suggestions.

I also would like to thank C. Meitle and A. Neeley for making accessaries for experiment and assisting with trouble shooting the equipment.

thanks to Rick Matson of SERI and quinseng

The financial support provided by the U. S. Air Force through a NSF grant MSM-8806051.

TABLE OF CONTENTS

LIST OF FIGURES

LIST OF TABLES

Electrical Characterization of n-Type Aluminum Gallium Arsenide

Chapter 1. Introduction

From the time of the demonstration of the bipolar transistor in 1947, demand for increased levels of integration and for higher speed performance has driven progress both in the development of devices and in the exploration of materials. Thus device and materials development have an inherent inter-relationship, since device yields are dependent upon the adequacy of the properties of materials. Evidence for the importance of materials development is supported by the fact that the use of ternary and quaternary compound semiconductors has become crucial to the development of modern devices, including those in opto-electronics, such as lasers, and in high-speed electronics, such as the high electron mobility transistor (HEMT).

This investigation is limited to n-type aluminum gallium arsenide, $Al_xGa_{1-x}As$, a ternary compound semiconductor. Ternary alloys, such as $Al_xGa_{1-x}As$, offer more flexibility in certain device applications than binary compounds due to their compositionally-dependent properties, such as energy bandgap. However, n-type $Al_xGa_{1-x}As$ exhibits peculiar electric and optical properties, such as a persistent photoconductivity (PPC) effect [1-8] and a large Franck-Condon shift [9,10]

(i.e., the photoionization threshold is much larger than the thermal ionization depth).

The PPC effect occurs in n-type $Al_xGa_{1-x}As$ at temperatures below 100 K. When n-type $Al_xGa_{1-x}As$ is exposed to above bandgap light, photogenerated carriers contribute to a large increase in the conductivity, as is the usual case for semiconductor materials. When the light source is removed, however, the photogenerated carriers persist in the conduction band for hours and even days, dependent upon the ambient temperature. The PPC effect is attributed to characteristic metastable deep states, the so-called DX centers where D and X refer to a complex composed of, respectively, a donor and an unknown defect as named by Lang *et al.*[9,10] in 1979. Since that time, numerous DX studies have been undertaken to establish the basic physics underlying this peculiar defect. In particular, the limited understanding of the fundamental physics of this effect has led to increased research interest on this subject over the past decade.

At present, the model proposed [11,12] by Chadi and Chang has gained wide acceptance as an explanation of DX behavior. According to this model, donor dopants, including Si, Te, and Sn, act as DX centers when the dopant atom is distorted away from its normal tetrahedral position into an interstitial position which becomes metastable concomitant with the trapping of an extra electron so that an occupied DX center is negatively charged. Although the model of Chadi and

Chang has gained wide acceptance, there are certain issues which lead some researchers to question the validity of this model. For example, Yu *et al.* [13] have observed that there is no off-center displacement of Te and Sn larger than 0.14 Å from the substitutional site when investigated by particle-induced x-ray emission (PIXE). This observation stands in contrast to the 1.17 Å distortion calculated by Chadi and Chang [11,12] for the group-IV dopant, Si.

In addition to PIXE analysis, many other experimental techniques have been employed to characterize the DX center including deep level transient spectroscopy (DLTS), Mossbauer spectroscopy, deep level admittance spectroscopy (DLAS), Hall (including photo-Hall) measurements, photocapacitance, photoconductance, and thermally stimulated capacitance (TSCAP) measurements. These measurements have been performed for various alloy compositions and under varying degrees of hydrostatic pressure. In spite of detailed scrutinization by a variety of experimental techniques and theoretical analyses, the atomic nature of DX remains a subject of debate.

Generally deep levels, such as the DX center, play an important role in establishing the properties of semiconductors. For example, deep levels often determine the minority carrier lifetime of a semiconductor. Also deep levels are often related to semiconductor device instabilities [14-24]. At low temperatures the PPC effect can destroy the functionality of an HEMT which employs an n-$Al_xGa_{1-x}As$ layer because of electron trapping in the AlGaAs

and associated threshold instabilities. Theis and Parker [25], Hofmann and Kohn [26], and Nathan *et al.* [27] have reported on device instabilities associated with DX centers at room temperature.

The principal purpose of this investigation is to develop an alternative method, based upon the minority carrier capture (MCC) technique, for measurement of the hole capture cross-section of the DX center and for identification of the charge state of the DX center at low temperatures. In the MCC process, photogenerated minority carriers, positively charged holes, diffuse into the space-charge region of a Schottky barrier diode sample, and are thus captured by DX centers. Consequently, positive charge accumulates in the space-charge region and the shrinkage of this region causes a subsequent increase in capacitance. Accordingly, the atomic nature of the DX center has been investigated through determination of the magnitude of the low-temperature hole capture cross-section of n-$Al_xGa_{1-x}As$:Te and n-$Al_xGa_{1-x}As$:Si.

A second purpose of this investigation is to undertake a study of a means to minimize DX centers, or other defects incorporated into n-$Al_xGa_{1-x}As$ layers, by optically-induced dislocation-glide and -climb processes. In the glide and climb processes, optical scanning is carried out using a CW krypton-ion laser at room temperature. The DX concentration of optically-processed samples and of samples which have not been subjected to any optical processing is then evaluated by C-V, DLTS, TSCAP, and DLAS techniques.

A review of the literature of the DX center associated with AlGaAs, the minority carrier capture (MCC) technique, and optically-induced dislocation-glide and -climb is presented in Chapter 2. Experimental procedures and techniques are described in Chapter 3. Subsequently, the experimental results and a discussion of the results of MCC measurements, are included in Chapter 4. The experimental results for optically-controlled dislocation-glide and -climb experiments are presented in Chapter 5. Finally, Chapter 6 includes conclusions and recommendations for future research.

Chapter 2. Literature Review

2.1 DX Centers in n-Type $Al_xGa_{1-x}As$

This review includes a discussion of the published data relevant to the electrical and optical properties of $Al_xGa_{1-x}As$ associated with DX centers as well as device effects due to DX. The essential properties of the DX center in n-type $Al_xGa_{1-x}As$ at $x \geq 0.22$, are:

(1) persistent photoconductivity (PPC) at low temperatures, and

(2) large Franck-Condon shift (i.e., a large difference in the energies of optical and thermal electron emission from the DX state to the conduction band).

Lang [28], Mooney [29], Bhattacharya [30], and Bourgoin [31] have provided extensive reviews of the properties of the DX center.

In general, it is accepted that most of the commonly used donor impurities (e.g., group IV, including Si, Ge, and Sn and group VI, including S, Se, and Te) give rise to large concentrations of deep level defects, called DX centers, in n-type $Al_xGa_{1-x}As$ used for the alloy composition of Al, $x \geq 0.22$. In 1975, the deepening of the donor ionization energy in Te-doped $Al_xGa_{1-x}As$ grown by liquid-phase-epitaxy (LPE) for $x \geq 0.22$, was first recognized by Springthrope *et al.* [32]. Subsequently the PPC effect was first observed in 1977 by

Nelson [2] in Te-doped $Al_xGa_{1-x}As$ ($0.25 \leq x \leq 0.7$) at low temperatures. The PPC effect was observed in S-doped $GaAs_{1-x}P_x$ as early as 1968 by Craford *et al.*[33].

In 1977, Lang *et al.* [9,10] proposed that charge capture and emission from deep donors occurs as a multiphonon process, and that a large relaxation of the crystal lattice resulted in the PPC effect. To account for the atomic nature of the large lattice relaxation (LLR), Lang *et al.* suggested that the origin of the AlGaAs deep level was a complex formed by the substitutional donor atom (D) complexed with an unknown lattice defect (X), quite possibly an As vacancy. The distorted $Al_xGa_{1-x}As$ conduction band and its corresponding generalized configuration coordinate diagrams, as proposed by Lang *et al.* [9,10] are shown in Figs. 2.1(a) and 2.1(b), respectively. In this diagram, four energies are used to characterize the DX center, including:

1) E_e = thermal emission activation energy,
2) E_{cap} = capture barrier for e^- (or capture activation energy),
3) E_d = binding energy, and
4) E_{hv} = optical emission energy.

Using a simple configuration-coordinate diagram, it was demonstrated that the measured barriers for electron capture and emission led to the prediction of a large optical energy

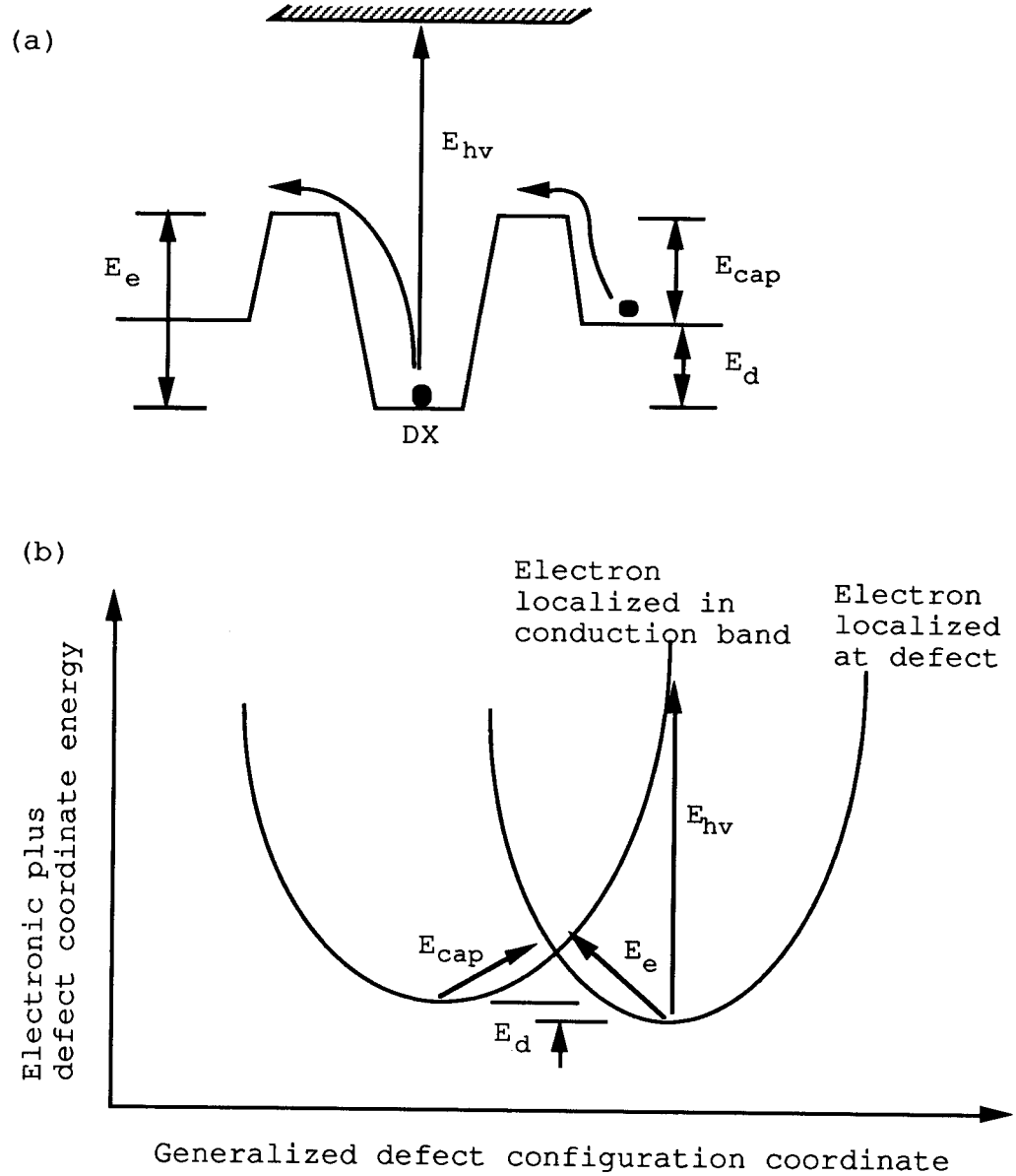

Figure 2.1 (a) Distorted $Al_xGa_{1-x}As$ conduction band edge, relating the PPC effect and large differences in optical and thermal emission energies; (b) Configuration coordinates corresponding to (a) [9].

E_{hv}, of 1.1 eV for the DX center, which was in good agreement with experimental results of 1.2 eV.

The activation energy, E_e, of Si-doped AlGaAs for the thermal emission of an electron from the DX level to the conduction band, as shown in Fig. 2.2, is independent of the alloy composition and doping concentration [34-36]. It was also found to be independent of applied hydrostatic pressure for Si-doped samples [37]. The values of the thermal emission energy of the DX center for various donor atoms are listed in Table 2.1.

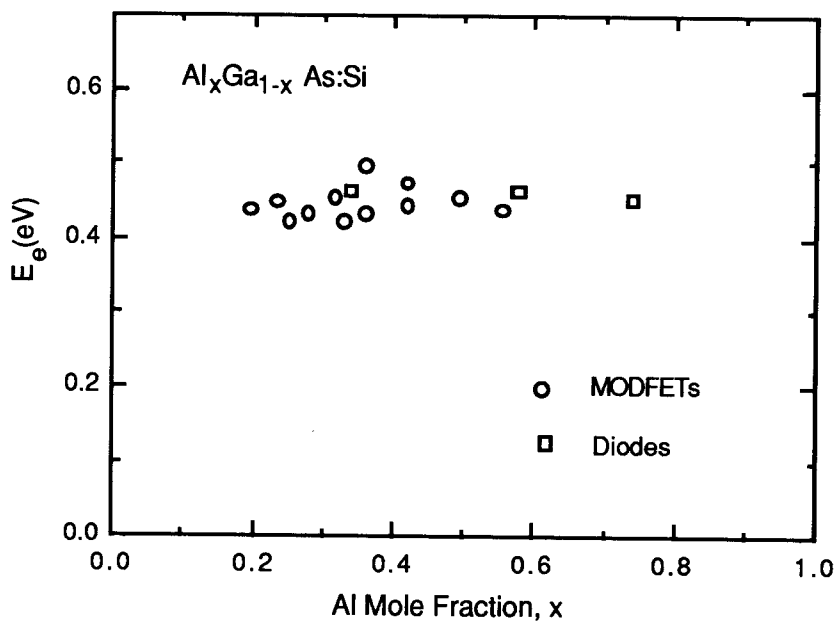

Figure 2.2. Thermal emission energy of the DX level in Si-doped AlGaAs [34].

Table 2.1. Values of DX center energies in AlGaAs for different donor species [29].

Donor species	E_e (eV) (DLTS)	E_{cap} (eV)	E_d (eV) (Hall)	E_e-E_{cap} (eV)	E_{hv} (eV)
Group VI					
S	0.28	-	0.150	-	-
Se	0.28	0.14	0.18	0.14	0.85
Te	0.28	0.14	0.177,0.186	0.14	0.85
Group IV					
Si	0.43	0.21	0.175-0.205	0.22	1.25,1.45
Ge	0.33	-	-	-	-
Sn	0.19,0.21	0.02	0.172,0.201	0.17,0.19	1.11

The binding energy, E_d, which determines the equilibrium concentration of ionized donors in Si-doped AlGaAs are measured by temperature-dependent Hall-effect measurements for various Al compositions [1, 38-42]. As may be seen from the schematic diagram in Fig. 2.3, the binding energy of the effective-mass-like shallow level follows the conduction band minimum, and the DX level lies about 160 meV below the L minimum of the conduction band. When $x < 0.22$, the DX level lies above both the conduction band minima and the effective-mass-like shallow level, and may be considered to be a so-called resonant state [43-46]. The existence of this level in n-GaAs is demonstrated by the observation of thermally activated electron capture and emission when they are brought into the direct gap by the application of hydrostatic pressure [47,48].

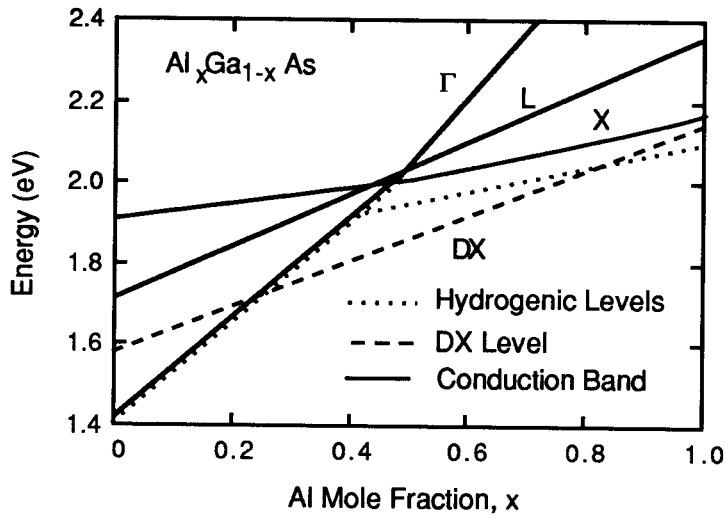

Figure 2.3. Energies of three conduction band minima, hydrogenic levels, and the DX level as a function of the composition of AlGaAs [29].

For $x > 0.22$, up to about 0.45 the binding energy increases as x is increased. Beyond the crossover from the direct to the indirect band gap, the DX center moves closer to the bottom of the conduction band. This correlation between binding energy and the band structure is independent of the donor species, and is also observed when the band structure is modified by hydrostatic pressure [36,48]. In other words, a DX center can be created even in GaAs, if GaAs is subjected to hydrostatic pressure [49]. The values of the DX center binding energies for various donor species are also listed in Table 2.1.

The capture barrier energy, E_{cap}, which is responsible for the PPC effect at low temperatures, is plotted as a function of the alloy composition for Si-doped AlGaAs in Fig. 2.4. The capture barrier has a minimum value of about 0.2 eV at approximately x = 0.35, near the crossover point from direct to indirect gap material. A steep decrease of E_{cap} can be expected when the alloy composition is increased from x = 0.27 to x = 0.32 because of the relation between E_e, E_{cap}, and E_d; the shape of the E_{cap} composition dependence is the inverse of E_d. This change is opposite to the variation in the conduction band offset between AlGaAs and GaAs, and the same trapping behavior can also be observed in thick AlGaAs layers. Thus, it is clear that this capture barrier is a property of the DX center, and not of the heterojunction structure [34]. When hydrostatic pressure is applied, the change in E_{cap} clearly demonstrates that its variation is in accordance with the alloy composition and is due to the changing band structure [36]. The capture activation energy can be measured by the transient decay of persistent photoconductivity (TDPPC) technique [50]. Capture emission energy values of the DX center for various donor species are also listed in Table 2.1.

Large optical emission energy, E_{hv}, which provides evidence for the large lattice relaxation (LLR) model, is one of the peculiar optical properties of the AlGaAs DX center. The magnitude of the lattice relaxation energy, which is the difference between the photoionization and donor thermal

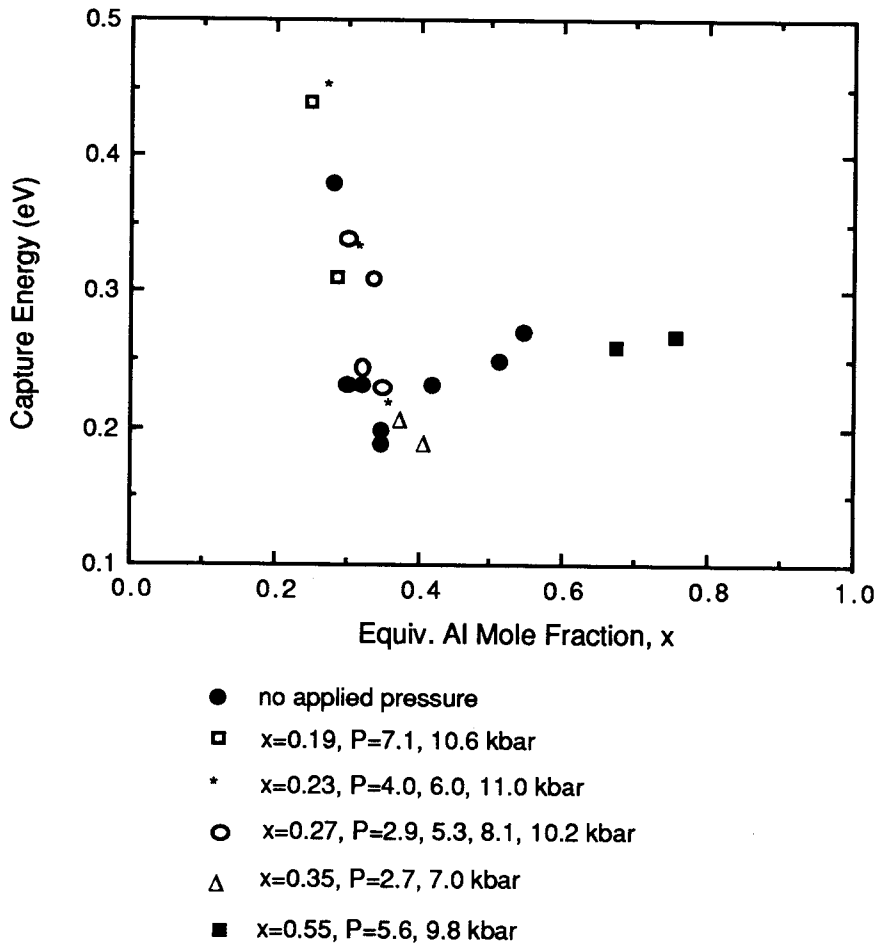

Figure 2.4. Capture activation energy as a function of composition and applied pressure [36].

binding energies, is an important DX center property. Measurement of the energy dependence of the photoionization cross section, σ_n^o, is a key experiment for determination of the lattice relaxation energy. The threshold for photoionization and for thermal emission, is dependent upon the dopant species [51], but not to any great upon alloy composition [9]. The large difference between the

photoionization threshold and donor binding energy, as well as the temperature dependence of σ_n^o, are in agreement with the model for multiphonon capture and emission [29]. A plot of the photoionization cross-section versus photon energy is shown in Fig. 2.5.

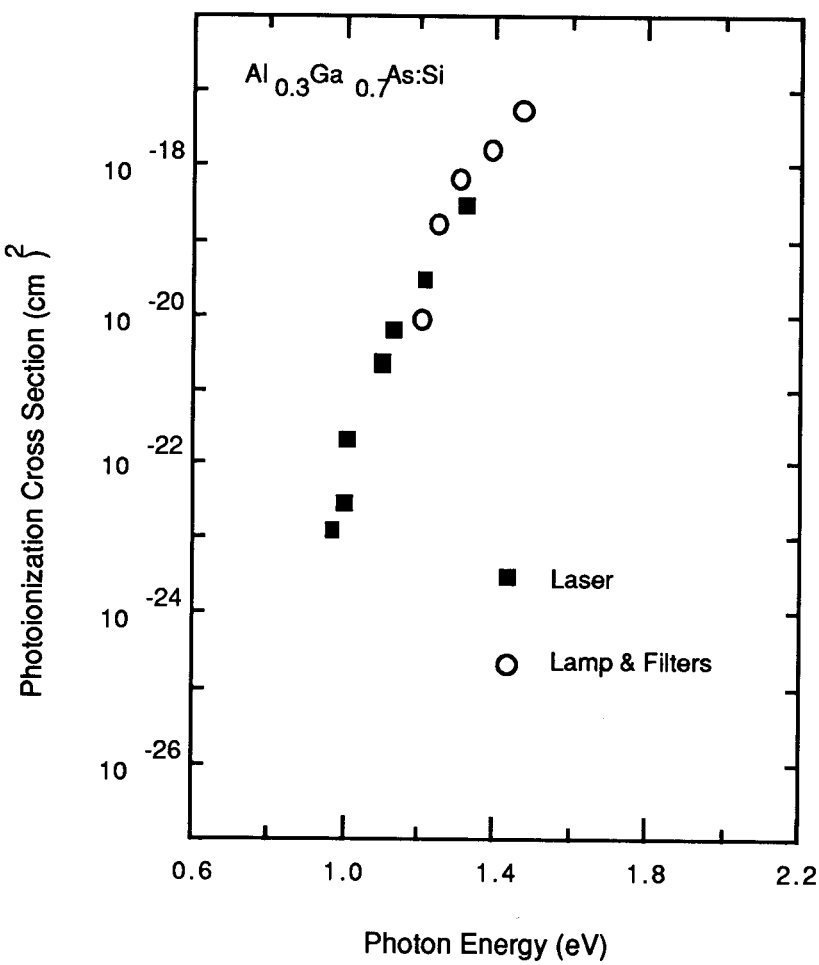

Figure 2.5. Dependence of the photoionization cross-section on photon energy for Si-doped $Al_{0.3}Ga_{0.7}As$ [63].

In 1980, Lifshitz *et al.* [52] reported an extensive set of Hall measurements over a wide range of composition and hydrostatic pressure for Sn-doped $Al_xGa_{1-x}As$. They proposed that donors have three levels, one associated with each of the conduction bands, Γ, L, and X, and with the following energies, $E_\Gamma - E_{d\Gamma} = 6$ meV, $E_L - E_{dL} = 150$ meV, and $E_X - E_{dX} = 100$ meV, respectively.

In 1982, Rochette *et al.* [53] examined the influence of DX centers in $Al_xGa_{1-x}As$ on the performance of HEMTs. In 1986, Nathan [54] reviewed the relationship of the PPC effect to HEMT performance. Between 1982 and 1990, experimentally observed effects of DX centers on HEMTs, in addition to the collapse of I-V characteristics at cryogenic temperatures [15], include the following:

1) PPC effect observed in two-dimensional electron gas (2DEG) structures [53];
2) Threshold voltage shift as a function of temperature due to steady-state occupation of DX [14];
3) Threshold voltage shift due to gate pulsing and the resulting drain transients [26,27,55];
4) Hot electron capture and related transient response due to drain bias pulsing [24,25,56]; and
5) The kink effect (i.e., a sudden rise in the drain current due to the tunneling of trapped electrons from AlGaAs near the AlGaAs/GaAs interface back into the bulk n-AlGaAs layer [20]).

In 1984, the results of extensive Hall measurements over the entire composition range ($0<x<1$) of Si-doped $Al_xGa_{1-x}As$ were reported by Chand *et al.* [38], and the existence of shallow and deep donor states associated with the DX center was analyzed by Watanabe *et al.* [42,57] and Schubert *et al.* [39]. Concurrently, the first measurements of far infrared (FIR) absorption of Si-doped $Al_xGa_{1-x}As$ were reported by Theis *et al.* [58]. When all DX centers are filled at low temperatures, FIR absorption is zero. However, FIR absorption increases after DX photoionization by 1 eV radiation. Thus, it was proposed that photoionized DX centers act as shallow donors, with the spectral response of FIR absorption indicating the energy of the shallow donor.

In 1985, Van Vechten [59,60] proposed a DX model consistent with the original model of Lang *et al.* [9,10]. But he additionally proposed a specific mechanism for the transition from the stable to metastable state in terms of nearest-neighbor hopping.

In the same year, PPC effects of Si-doped GaAs subjected to various hydrostatic pressures were first observed by Mizuta *et al.* [49]. It was shown that DLTS signals characteristic of DX-like centers start to appear in Si-doped GaAs at a pressure of about 24 kbar and grew in intensity as the pressure was increased; at the same time, the critical pressure at which the DX DLTS signal began decreased as Al was alloyed in small amounts. These findings brought into question the validity of the DX model proposed by Lang *et al.*

[9], and a new model for the DX center began to emerge. Mooney *et al.* [29,34,36,54,61-63] conducted a systematic study, using HEMT structures, and deduced the emission and capture barriers of the DX center over a wide range of Al composition. They found that the thermal emission activation energy is constant at E_e = ~0.43 eV, for a composition range of $0.2 < x < 0.7$. For $0.2 < x < 0.45$, the capture barrier decreases, increasing once again for $x > 0.45$, a finding consistent with Hall measurement results that the binding energy, E_d, increases for $0.2 < x < 0.45$ and decreases for $x > 0.45$.

In 1986, Theis *et al.* [56] observed hot-electron capture by DX centers in short channel GaAs/$Al_xGa_{1-x}As$ field effect transistors for $x < 0.2$. For these devices, electrons which were sufficiently heated were trapped in the Si-doped $Al_{0.14}Ga_{0.86}As$ layer and contributed to drain current transients. They proposed that resonant, localized states of the DX center exist, even for $x < 0.2$. These resonant DX states could be populated either by means of hot electron trapping or by raising the Fermi level closer to the resonant state by heavy doping.

In 1987, Henning and Ansems [64,65] remeasured the photoionization threshold (i.e., the optical emission energy, E_{hv}), using photoconductivity measurements rather than photo-capacitance measurements. They deduced a very weak photo-ionization threshold at an energy of 200 meV which they claimed as support for the small lattice relaxation (SRL)

model. Mooney *et al.* [63] repeated their photo-capacitance measurements, reconfirming the large photoionization threshold energies (1.4-1.8 eV).

In 1988, Chadi and Chang [11] proposed that donors incorporated into $Al_xGa_{1-x}As$ behave as a negative U center. The DX state is postulated to be highly localized and negatively charged, resulting from the reaction

$$2d^o \text{ ---> } d^+ + DX^-,$$

where d^o and d^+ represent, respectively, neutral and ionized substitutional donors. This reaction is energetically favored because of the negative U character of the donor. The DX^- state is produced by the displacement of the Si atom along the <111> direction toward an interstitial position [12] and the DX^- state is stabilized by the capture of one extra electron.

In 1989, Basmaji *et al.* [66] grew Sn-doped $Al_xGa_{1-x}As$ over a concentration range of $0.2 < x < 0.4$ by metalorganic vapor phase epitaxy (MOVPE) in a temperature range of 850-950°C. They claimed that Sn-doped $Al_xGa_{1-x}As$ epilayers grown at unusually high temperatures did not exhibit the PPC effect. In addition, a 10 meV binding energy was obtained from the temperature-dependence of Hall measurements.

Most recently, Yu *et al.* [13] employed particle-induced x-ray emission (PIXE) and ion-beam-channeling methods to determine the lattice locations of Te and Sn atoms, Both of which form DX centers in $Al_xGa_{1-x}As$. In this study, the group-VI dopant, Te atom, was found to occupy an As substitutional

site, while the Sn group-IV dopant was found in the Ga(Al) site. No off-center displacements of Te or Sn larger than 0.14 Å from the substitutional site were observed for either system. These experimental displacement values differ significantly from those for Si as calculated by Chadi and Chang [11,12] to be 1.17 Å.

Thus, over the past 20 years a number of experimental investigations of proposed models for the microscopic nature of the DX center have been conducted, and may be placed into two basic categories:

1) A defect complex, consisting of the donor atom and an intrinsic lattice defect which is possibly an arsenic vacancy, V_{As} [9,10]; and
2) A simple substitutional donor:
    a) with large lattice relaxation (LLR) [67-69],
    b) with small lattice relaxation (SLR) [3,38,70], or
    c) with a negative U property [71,72].

Despite vast research efforts, none of the proposed models offer a convincing explanation for the essential properties of the DX center, i.e., the PPC effect and the large Franck-Condon shift. Generally, it is believed that the DX center is negatively charged at low temperatures. However, there is still an unknown factor: How many electrons are present in the DX center? Accordingly, the microscopic structure of the DX center remains a controversial issue.

2.2 Minority Carrier Capture

The minority carrier capture (MCC) technique for n-type GaP was developed by Hamilton *et al.* [73-75] for the detection of nonradiative recombination centers, which are responsible for the low quantum efficiency of green-emitting GaP LEDs. The trap density, activation energy, and capture cross-section of deep levels in the n-type GaP semiconductor material were estimated by the MCC technique. In the MCC technique, near-band-gap-light was irradiated through a semitransparent Schottky contact to the GaP, and then the capacitance rise-time was measured as a means of estimating the activation energy and the hole capture cross-section. The capacitance decay time was measured by removing the light from the sample to deduce the trap density.

At present, the nature of the charge state of the DX center is the subject of some controversy. Although, Watanabe *et al.* [76] measured the temperature dependence of the hole capture cross-section for the DX center by DLTS using an AlGaAs:Si p^+-n structure and estimated the hole capture cross-section at 204 K as 1.3×10^{-17} cm^2, the charge state of the DX center was not addressed. Accordingly, verification of the charge state of the DX center is an issue in which further experimental investigation is required.

2.3 Optically-Induced Dislocation-Glide and -Climb

The presence of defects in the form of imperfections or impurities in active device regions is the source of various device problems including dark line defect (DLD) formation with associated degradation of double heterostructure (DH) lasers [77-80] and the collapse of I-V characteristics of HEMTs at low temperatures [15]. To reduce defect-related instabilities in silicon devices, "gettering" was first employed by Bemski [81] and Goetzberger and Shockley [82].

Gettering is generally defined as the removal of process-induced contaminants from the active region of a device. Traditionally, there are two categories of gettering: extrinsic (or external) and intrinsic (or internal) [83]. An example of extrinsic gettering is the introduction of defects onto the backside surface of a wafer and subsequent trapping of mobile defects at the damaged backside. In the case of intrinsic gettering in Si, these defects are closely related to the presence of SiO_2 precipitates, predominantly generated within the bulk of the Si wafer. Optically-controlled misfit dislocation-glide and -climb may be classified as an extrinsic gettering process.

The distinction between dislocation-glide and -climb is that glide involves conservative motion. That is, lattice sites are neither added to nor removed from the sample when glide occurs. Glide generally occurs as a means to relieve external stress (i.e., strain energy associated with a misfit

at the interface is relaxed by the formation of misfit dislocations [84]). Note that point defects are neither added to nor subtracted from the dislocation when the dislocation moves by glide. The strain energy present at interfaces between layers is the driving force for dislocation-glide.

In turn, climb is nonconservative motion of a dislocation. Lattice sites are either added to or subtracted from the sample during climb, and vacancies or interstitials are created or annihilated (i.e., a dislocation increases its length by absorption or emission of point defects.[85]). Supersaturation of point defects is the most common driving force for dislocation climb [77]. The differences between dislocation glide and climb are summarized in Table 2.2.

Table 2.2. Differentiation of dislocation-glide and -climb characteristics.

	Glide	Climb
Motion	Conservative	Non-conservative
Displacement of the dislocation	$dV = 0$ (V= volume)	$dV \neq 0$ (V= volume)
Driving force	Strain energy	Supersaturation of defects
Preferential moving directions	<110>[21]	<100>[86]
Dislocation velocity [87]	40-50 um/sec at $2x10^5$ W/cm^2 of optical power density	0.1-0.3 um/sec at $2x10^5$ W/cm^2 of optical power density
Threshold [87]	yes: sharp threshold	no

Investigations of dislocation glide and climb originated from observations of the degradation of GaAs-AlGaAs double heterostructure (DH) lasers and GaP green-LEDs during device operation. In 1973, Petroff and Hartman [86] observed nonluminescent areas in GaAs-AlGaAs DH lasers which appeared as DLD during device operation. Propagation of the dislocation network developed largely along directions close to <100> and, upon occasion, <110>, and was attributed to a climb mechanism induced by the operation of the device.

In 1974, Lang and Kimerling [88] first observed electron-hole recombination-enhanced defect annealing in GaAs. A significant amount of annealing was observed when the GaAs diode was in forward bias below 100°C. At nearly the same time, Petroff and Hartman [77] observed, from TEM analysis of degraded DH AlGaAs laser devices, that very large vacancy concentrations were involved in the climb process. AlGaAs and GaAs interface layers were attributed to be the main source of vacancies. Enhanced diffusion and drift of the vacancies causes a fast dislocation climb rate, accelerating device degradation.

Further experiments took advantage of the climb phenomenon, which had previously been viewed as an impediment to device operation, to improve device electrical properties and to minimize imperfections within crystals. Lang *et al.* [89] applied the climb phenomenon in reverse, observing a reduction of DX center concentrations in the vicinity of climb-induced <100> networks.

In 1976, Monemar and Woolhouse [21] observed DLD in GaAs/AlGaAs DH laser materials and found that the rapid DLD growth(10-100 μ/sec) was caused by the generation of misfit dislocation networks during external optical excitation. This was attributed to the glide mechanism. At nearly the same time, Matthews *et al.* [90] suggested that a misfit strain could be used to drive threading dislocations to the edge of epitaxial thin film, thus improving the perfection of the film. Matthews *et al.* also reported that threading dislocations in multilayers could be removed more effectively than for single layers.

In 1977, O'Hara *et al.* [91] proposed an alternative model for the driving force of climb in which the energy released by electron-hole recombination at the dislocation caused the emission of vacancies into the surrounding lattice. In this mechanism, it was envisioned that an atom in the lattice adjacent to the dislocation core would jump into the extra half-plane of the dipole, leaving a vacant site in the lattice, which would then migrate away from the dipole. The motivation behind this proposal was that if the material contained large concentrations of excess interstitials, then it could be expected that they would condense to form small dislocation loops during suitable high temperature annealing. However, this does not occur in laser materials [92].

In 1978, Monemar *et al.* [87] observed a sharp threshold for optically-induced glide processes in which the dislocation velocity changes by more than a factor of 10^3 as

the excitation intensity is changed by only 20%. As shown in Fig. 2.6, this effect is not related to either recombination-enhanced motion or to local heating. The effect was explained in terms of the reduction of frictional forces by interaction with unrecombined carriers.

In 1984, Van Vechten [93] provided an explanation of the CW-laser annealing process for the improvement of the

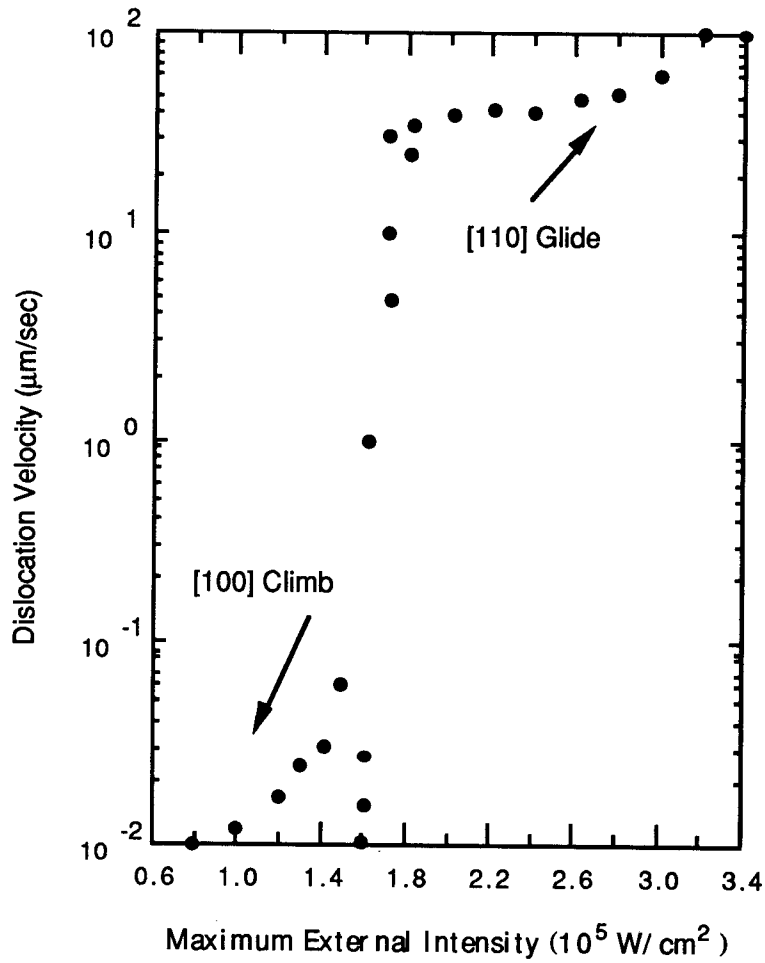

Figure 2.6. Rate of glide and climb of threading components of misfit dislocations on GaAs-AlGaAs hetero-structure versus optical irradiation intensity [87].

luminescent efficiency of LPE AlGaAs 3-layer heterostructures by as much as 80%. This was explained in terms of the redistribution of defects grown within the original material. In particular, the improvement in luminescent efficiency was attributed to the elimination of vacancies and interfacial mismatch stresses due to microsplit formations.

Salih *et al.* [94-96] introduced intentional interfacial misfit dislocation during Ge-doped Si epitaxy to obtain gettering of metallic impurities, which were then diffused toward the dislocations by annealing the sample at 900°C. Ge introduction into the Si epitaxial interface is a corresponding process to the optically-controlled dislocation-glide in terms of misfit dislocation generation at the interface between the epi-layer and bulk, whereas the high temperature annealing of the Si sample corresponds to optically-controlled dislocation-climb in terms of point defect gettering at the misfit dislocation.

Recently, Garosshen *et al.* [97] examined the influence of light on dislocation motion for CdS and $(Hg_{0.3}Cd_{0.7})Te$ semiconductors. Under illumination using either a 100 W halogen bulb or a ~ 2 mW helium-neon laser, the observed photoplastic effect (i.e., a change in flow stress during irradiation owing to the interaction of photo-induced charge carriers and dislocations) for CdS is larger than that for $(Hg_{0.3}Cd_{0.7})Te$. The photoplastic effect was greatest at light photon energies just below the band gap energy and increases with light intensity. It was suggested that the photoplastic

effect could be employed to control dislocation densities for semiconductors which exhibit photoplastic behavior.

Chapter 3. Experimental Procedure

In this chapter sample fabrication and experimental procedures for the minority carrier capture (MCC) and optically-controlled dislocation-glide and -climb experiments are described. Additionally, modifications of an expander module for a helium closed-cycle cryostat are detailed. Finally, the electrical characterization techniques employed for the characterization of optically-processed and -unprocessed samples (i.e., C-V, DLTS, DLAS, TSCAP, and I-V measurements) are described in the last section.

3.1. Minority Carrier Capture Experiment

3.1.1. Schottky Barrier Diode Fabrication

Two types of starting materials are used for MCC experiments: (1) 3μm-thick, Te-doped, n-type $Al_xGa_{1-x}As$ epi-layer with x = 0.3 and a doping concentration of 2.5×10^{17} cm^{-3}, grown at Boeing by V. Sundaram by metalorganic chemical vapor deposition (MOCVD) on a standard n^+-GaAs substrate with a (100) orientation; and (2) 2μm-thick, Si-doped, n-type $Al_xGa_{1-x}As$ epi-layer with x = 0.3 and a doping concentration of 2×10^{17} cm^{-3}, grown at Oregon State University by molecular beam epitaxy (MBE) on a standard n^+-GaAs substrate with a (100) orientation. The front side of the Si-doped wafer is covered with wax to protect its surface during chemical

etching; that is, the wafer is dipped in HCl to remove the indium which is used as a cement to firmly attach the wafer to the sample holder during MBE growth. A detailed indium removal procedure is provided in Procedure 3.1. The Te-doped wafer is cleaned by a standard procedure; that is, it is rinsed with trichlo-roethylene (TCE), acetone, methanol, and DI water. Care is taken to avoid contamination during the surface preparation.

Procedure 3.1. Indium removal.

1. Heat a clean glass plate, place the sample face down on melted wax, press the sample gently into the wax, then let the sample cool.
2. Dip the sample into an HCl solution for 1 hr.
3. Grind the back side of the sample with a smooth abrasive pad containing fine alumina powder until the indium can not longer be seen.
4. Remove the sample from the glass plate by the application of heat.
5. Thoroughly remove the wax by dipping the sample in a hot TCE bath.
6. Rinse the sample with acetone, methanol, and DI water.
7. Blow-dry the sample thoroughly with nitrogen air.

The Te- and Si-doped wafers are then immediately placed in a vacuum chamber for metal evaporation. A series of nickel (Ni), gold-germanium (Au/Ge), and gold (Au) metals are evaporated onto the back side of the n^+-GaAs substrate using a Veeco vacuum evaporator to form an ohmic contact. The

wafers are then annealed for 5 minutes at 420°C in forming gas. The wafers are scribed into small pieces to mount in a dual-in-line package (DIP). The scribed samples are rinsed using the standard cleaning procedure described previously, then placed into the vacuum chamber for metal deposition. Au is evaporated onto the sample surfaces by using either a shadow mask or a lift-off process, as shown in Procedure 3.2, to form the Schottky contact. The contact areas of the Te- and Si-doped samples are 3×10^{-3} cm^2 and 1×10^{-3} cm^2, respectively.

Procedure 3.2. Lift-off process.

1. Spin hexamethyldisilazane (HMDS) adhesion promoter onto the sample at 3000 rpm.
2. Spin photoresist onto the sample at 3000 rpm.
3. Softbake the sample for 15 min at 85°C.
4. Dip the sample in Chlorobenzene for 3.5 min.
5. Rinse the sample with DI water.
6. Expose the sample to a mercury lamp for 9 seconds.
7. Develop the sample for 5-10 seconds, depending upon the developer freshness (developer:DI water = 1:3).
8. Evaporate Au metal.
9. Dip the Au evaporated-sample in an acetone bath until the photoresist is completely lifted-off.

The Schottky barrier diodes are mounted on the DIP using silver conductive paste, and subsequently annealed at 250°C for 2 minutes to harden the paste. Finally, an ultrasonic Au wire bonder is used to connect the Schottky and ohmic contacts to the DIP bonding pads. To avoid possible damage

due to ultrasonic vibration from the bonder, the ultrasonic power is turned off and indium is used as a cement to adhere the Au ball to the Schottky dot. The tail portion of the Au wire is bonded to the DIP bonding pad, using regular ultrasonic power. A schematic diagram of a sample mounted on the DIP is shown in Fig. 3.1.

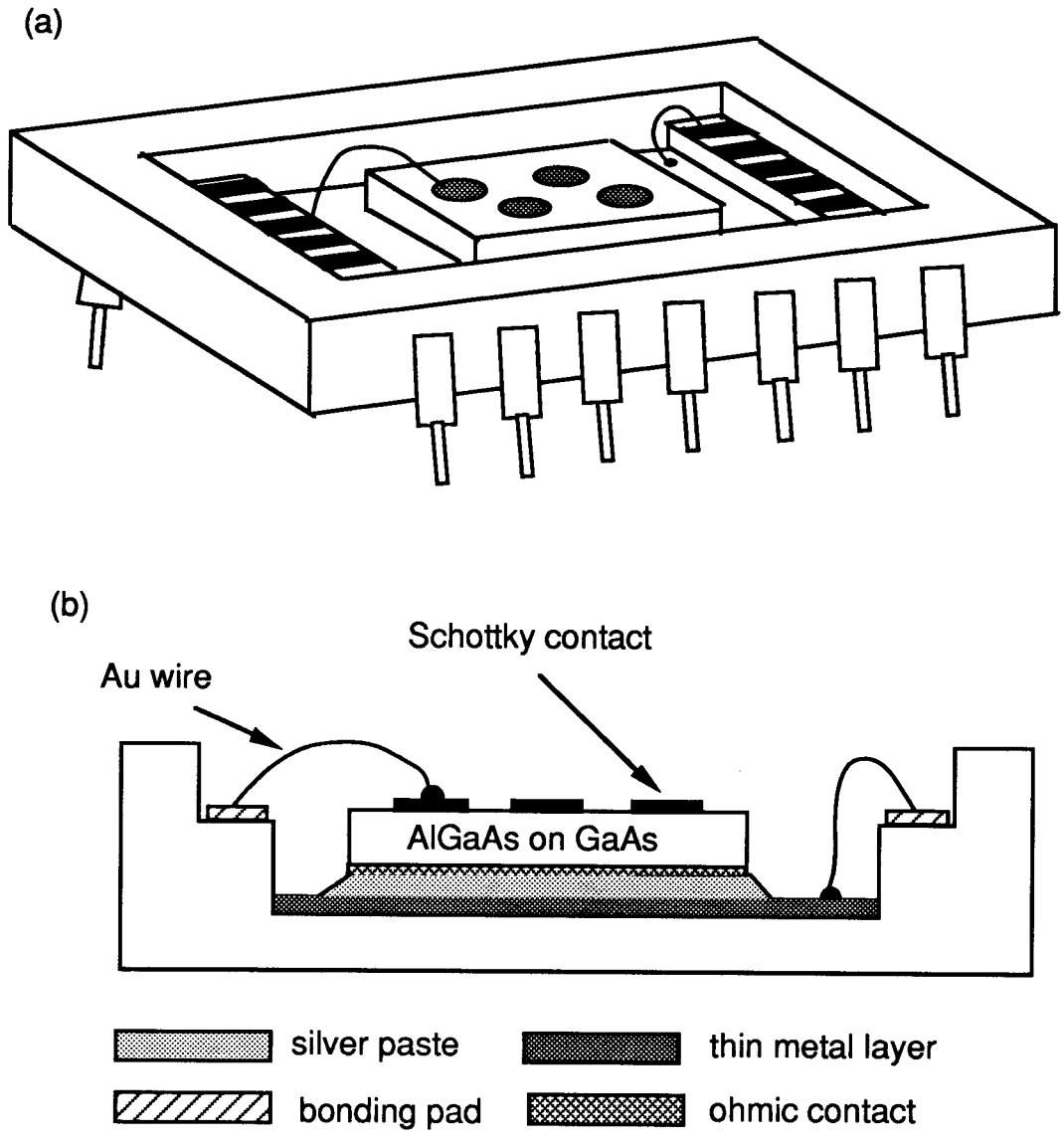

Figure 3.1. Schematic diagram of sample mounted on DIP. (a) overview of the sample; (b) cross-sectional view of the sample.

3.1.2 Modification of the Expander Module for a Helium Closed-Cycle Cryostat

3.1.2.1 Modification of the Expander Module Housing

To reduce pickup noise, the expander module housing is modified as shown in Fig. 3.2(b'). For the conventional back cover, the electrical wires run through the expander module, which is normally very cold during operations, to establish an electrical connection to the sample. Accordingly, the longer wires have a greater chance to pickup noise during the measurement of capacitance transients, and the resistance of the wire can be affected by cryogenic temperatures.

To surmount these problems, a modified back cover is designed as follows. The conventional back cover (Fig. 3.2(b)) is replaced by a modified cover, in which air-tightened BNC connectors are installed. A pair of wires, two inches in length, are sufficient to connect the sample to air-tightened BNC connectors. The use of short wire lengths served to reduce the possibility of noise pickup during measurements. In addition, the wire resistance remained stable under cryogenic temperatures since there is no need to run the wire through the cold expander module.

A conventional front cover with window is shown in Fig. 3.2(a). In general, the sample is exposed to monochromatic light through the window for excitation of the sample. However, extreme care should be taken to avoid ambient light leakage during low temperature measurements since the AlGaAs

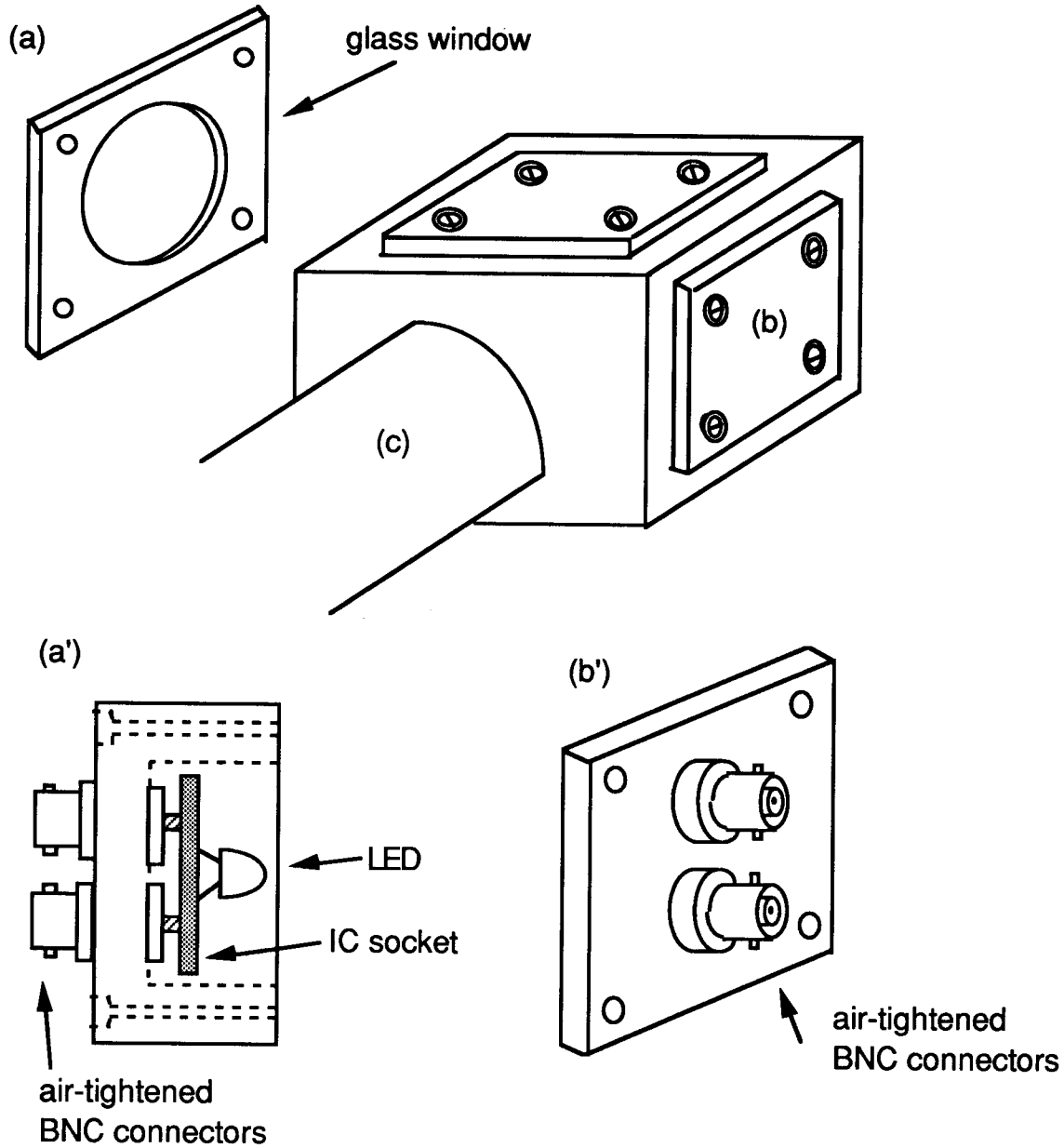

Figure 3.2. A schematic diagram of the modified expander housing unit. (a) conventional front cover with window; (b) conventional back cover; (a') modified front cover with built-in light source (this cover can be used in place of (a)); (b') modified back cover with air-tightened BNC connectors.

sample is very sensitive to weak ambient light.

Optical alignment poses a second problem. That is, it is difficult to focus the monochromatic light onto the Schottky dot of the sample. (Note: These problems were subsequently solved, respectively, by the installation of a dark box between the monochrometer and the glass-windowed front cover, and by the installation of a focussing lens installed on an xyz-translation stage. These solutions are indicated in Fig. 3.4.)

To alleviate these problems, a modified front cover with an IC socket (Fig. 3.2(a')) was designed. The IC socket pins are soldered to the BNC connector legs so that the LED could be easily replaced when a different wavelength LED is required. The modified front cover with an LED can be used in place of the conventional glass-windowed front cover (Fig. 3.2(a)).

3.1.2.2. Installation of a Second Thermocouple

A conventional expander module has one Au-Cr thermocouple, buried in the cold head of the expander module (Fig. 3.3). However, it is obvious that there are temperature differences between the cold head and the sample. Thus, the measured temperature would not reflect the sample temperature.

To measure the sample temperature with greater accuracy, a second thermocouple was installed on a dummy sample, as shown in Fig. 3.3. The dummy sample was also mounted on the

DIP, which was installed adjacent to the real sample on the cold head of the expander module. The measured temperature from thermocouple #2 was approximately 5°K higher than the temperature of thermocouple #1 at fixed cryogenic temperatures. However, due to thermal lag, a temperature difference of 10-13°K is observed from the two thermocouples when the temperature is continuously scanned.

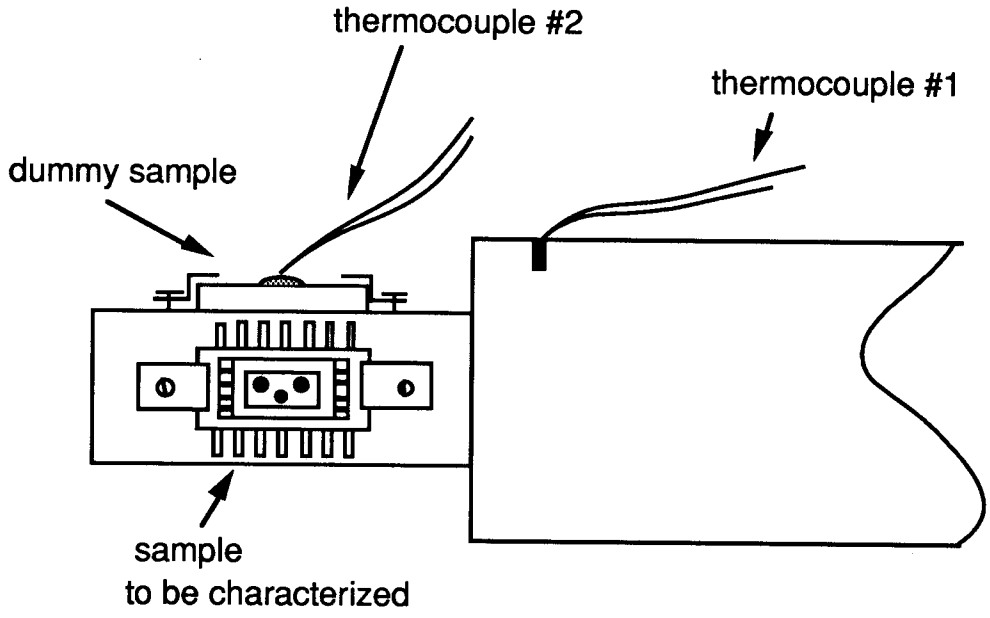

Figure 3.3. Schematic diagram of the installation of a second thermocouple onto the cold head of the expander module.

3.1.3. Minority Carrier Capture Experimental Setup and Procedure

A schematic diagram of the MCC experimental setup is shown in Fig. 3.4. The setup equipment included:

1) A fast capacitance meter (HP 4280A);
2) A desktop computer (HP 9326) for equipment control and data acquisition;
3) A pico-ammeter (HP 4140B);
4) A helium closed-cycle cryostat (DF 202, Air Products), a temperature controller (5500, Scientific Instruments, Inc), and a compressor unit (HC-4, Air Products);
5) A monochrometer (Jarrell-Ash); and
6) A light source (tungsten bulb).

A dark box is installed between the monochrometer and the glass-windowed front cover of the cryostat to completely shield the sample from possible ambient light leakage. A focusing lens is then installed on the xyz-translation stage, which is placed in the dark box, so that the monochromatic light could be easily focused onto the Schottky dot of the sample.

The Schottky barrier diode mounted on a DIP (Fig. 3.1) is installed on the cold head of the expander module, as shown in Fig. 3.3. The expander is evacuated by a vacuum pump for 30 minutes prior to turning on the compressor. The experimental procedure is then as follows:

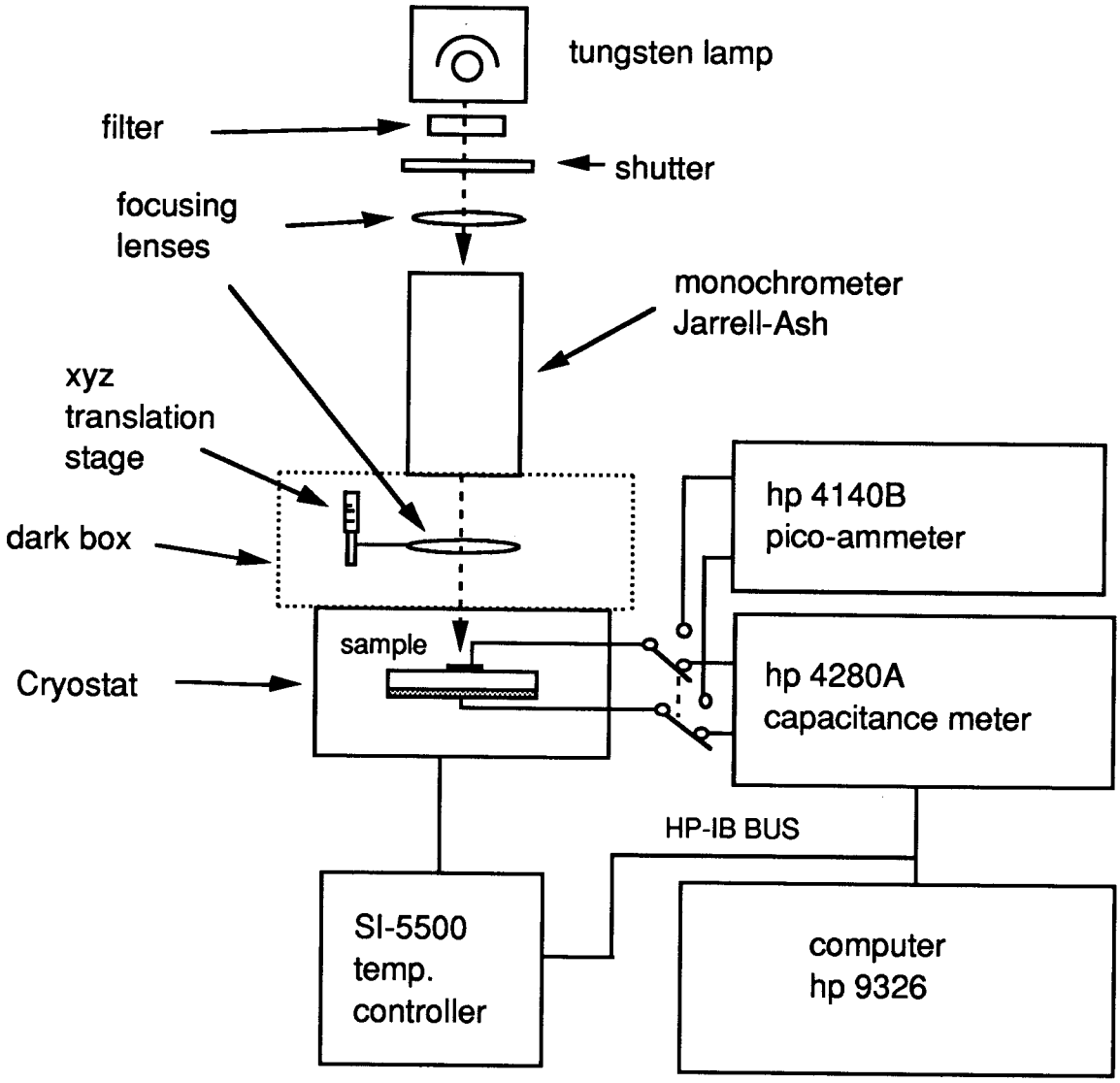

Figure 3.4. Schematic diagram of minority carrier capture experimental setup.

a) Cool the sample in dark.
b) Measure the sub-bandgap light photon flux using an optical power meter.
c) Measure the capacitance rise time, τ_{r2}, from the capacitance transient, using sub-bandgap light.
d) Heat the sample to room temperature to reset, then cool to its initial temperature as in step (a).
e) Adjust the near-bandgap light intensity to obtain the same photon flux as in step (b).
f) Measure the capacitance rise time, τ_{r1}, from the capacitance transient, using near-bandgap light and a photon flux identical to that in step (b).
g) Measure the short circuit current, J_{sc}, using near-bandgap light.
h) Repeat steps (a)-(g) for different temperatures.

The photon flux is estimated by measurement of the optical power of the monochromatic light with the quantum efficiency assumed to be 1. Based upon this assumption, the photon flux is,

$$\phi = \frac{P}{hv} = \frac{P\lambda}{hc},$$

where P = optical power of the monochromatic light,
h = Plank's constant,
λ = wavelength of the monochromatic light, and
c = speed of light.

3.2. Optically-Induced Dislocation-Glide and -Climb Experiment

3.2.1. Sample Preparation, Experimental Setup and Procedure for Optically-Controlled Dislocation-Glide and -Climb

An $Al_{0.3}Ga_{0.7}As$ epi-layer of tellurium (Te) doped ($n = 2.5 \times 10^{17}\ cm^{-3}$), 3μ in thickness, grown by MOCVD on the n^+-GaAs substrate at Boeing, is used as the sample for the optically-controlled dislocation-glide and -climb experiment.

Au/AuGe/Ni alloys were thermally evaporated onto the back side of the AlGaAs wafer and thermally annealed for 5 minutes at 420°C in forming gas (i.e., N_2 mixed with 2% H_2) to establish the ohmic contact. The ohmic-contacted AlGaAs wafer is then scribed in 2mm x 1.5mm sizes, and

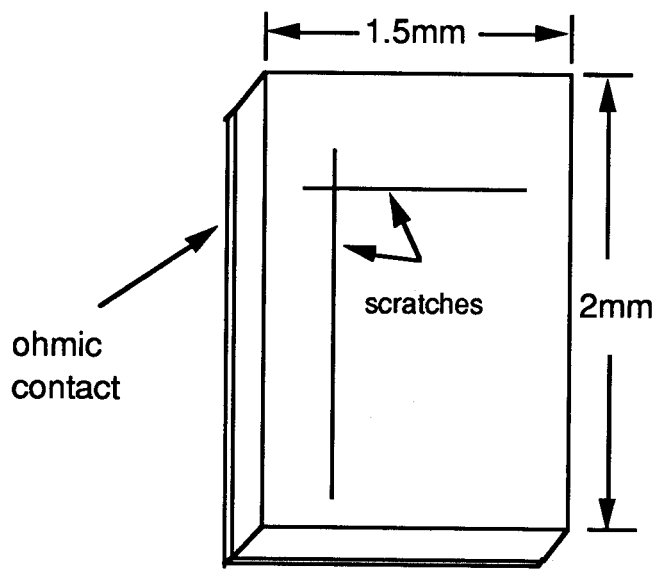

Figure 3.5. Dislocation-introduced sample.

dislocations were intentionally introduced in the AlGaAs sample by scratching the surface along the cleavage edges <011>, as shown in Fig. 3.5.

The experimental setup for dislocation-glide and -climb is shown in Fig. 3.6. A CW krypton-ion (Kr^+) laser (INNOVA 20) is used as an optical source. The maximum optical power and the wavelength of the CW Kr^+ laser are about 1.5 ~ 2

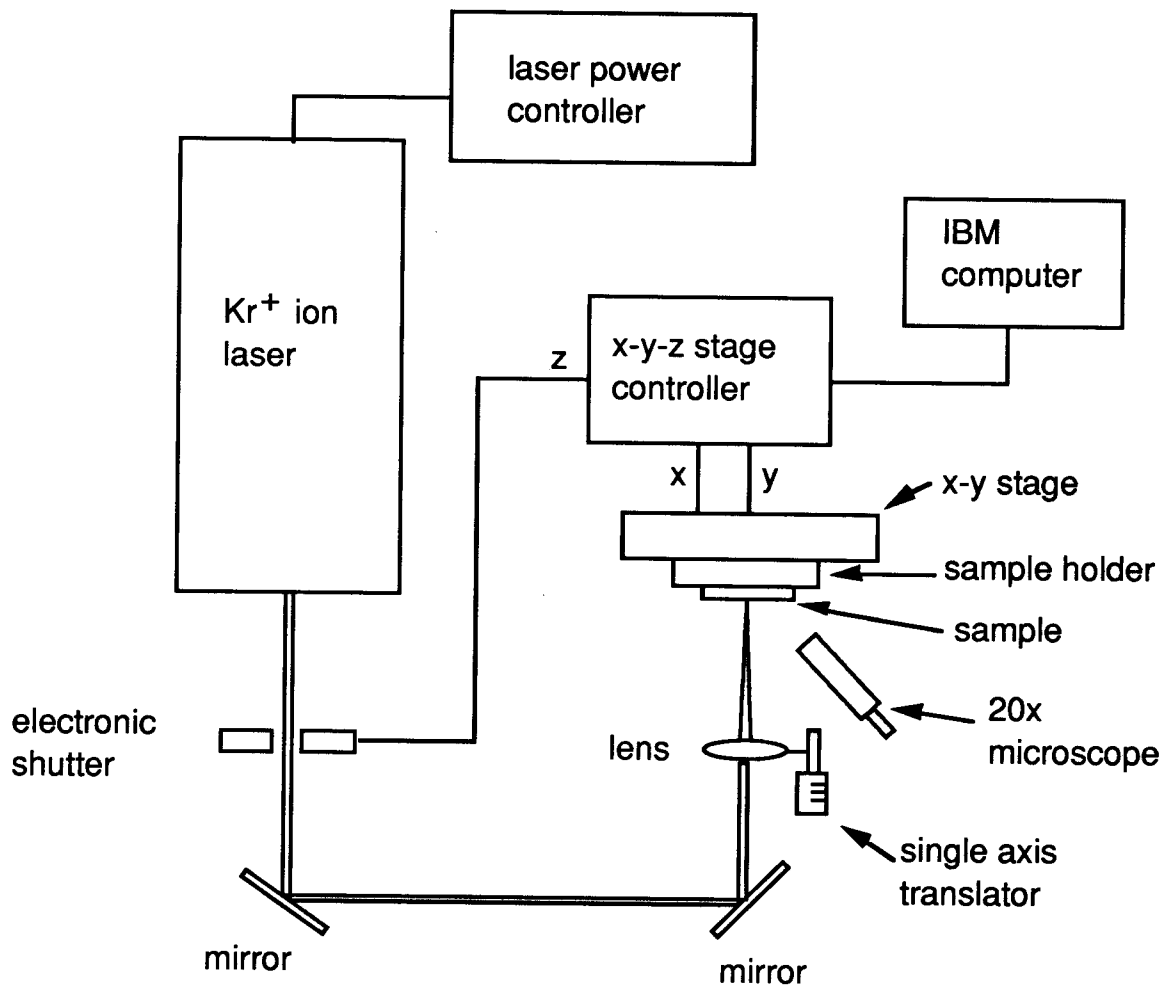

Figure 3.6. Experimental setup for dislocation-glide and -climb.

watts in a multimode operation and with wavelengths 647.1 and 676.4 nm (1.83 and 1.92 eV in photon energy).

Two mirrors are installed to adjust the x and y positions of the laser beam. A microscope objective lens (focal length = 2 cm), used to concentrate the laser beam, is installed on the single axis translator to adjust the beam size. The optical power of the laser is reduced by 30% following installation of the two mirrors and the lens. A 20X microscope is installed by the x-y translation stage to locate the laser beam spot on the sample. An electronic-shutter is installed in front of the laser to prevent sample exposure to the returning laser beam. The electronic-shutter is controlled using the z-port of the xyz translation stage controller, which is connected to an IBM computer by an RS232 cable. The sample is mounted on a sample holder, which is in turn mounted onto the x-y translation stage. The speed of the x-direction and the step size of the y-direction are controlled by the stage controller and the IBM computer.

During the dislocation-glide process, the shutter allows the laser beam to scan from 1 to 2 and 3 to 4, progressively, but not from 2 to 3 and 4 to 5, as shown in Fig. 3.7. (In reality, the x-y stage travels in either the x- or y-direction.) The scanning speed employed for the laser beam (x-direction) ranges from 30-50 um/sec, while the beam step-size (y-direction) ranges from 20-50 um. The laser beam waist is about 50 um, and the optical power density for the glide process is about 6.9×10^4 W/cm^2. The laser scanned area is

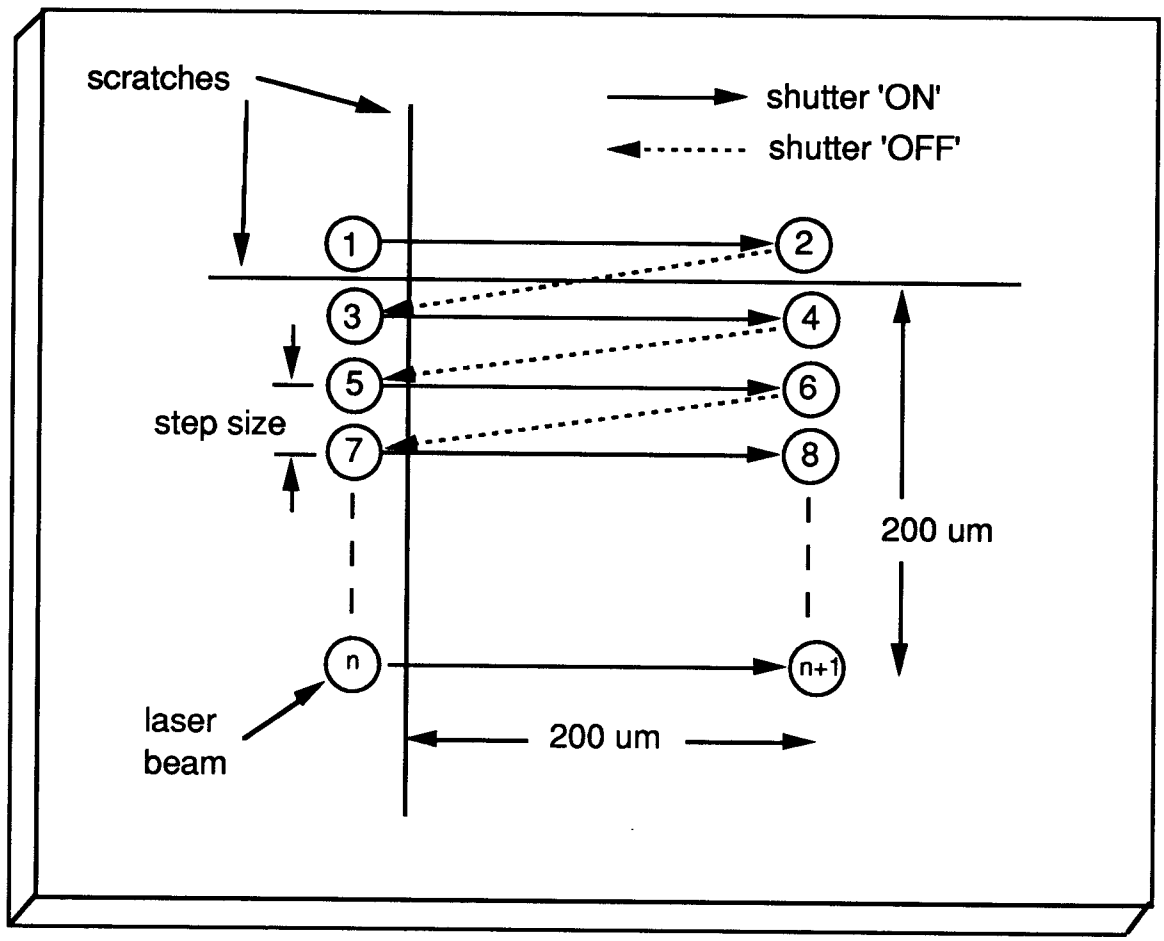

Figure 3.7. A schematic diagram showing the laser scanning. Solid and dotted lines indicate shutter on and off, respectively.

200 x 200 um.

For the dislocation-climb process, the laser beam size is increased in a range up to 280 um and irradiation on the previously glided-samples occurs for 2 to 20 hours. An unglided sample (sample #ODL34) with a check-pattern of scratches, as shown in Fig. 3.8, is irradiated by laser at an optical power density of 3400 w/cm^2. After the climb process,

an Au Schottky contact of 140 x 140 μm is formed by evaporation and lift-off.

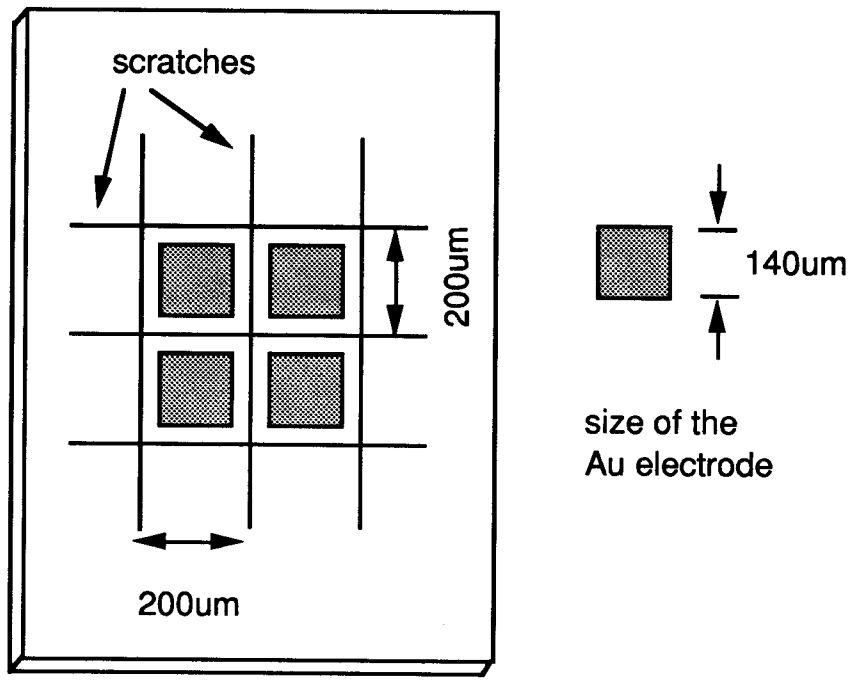

Figure 3.8. Unglided-sample with a check-pattern of scratches. After the climb process, Schottky contacts are formed.

One of the glided samples (sample #OPTXE) is illuminated with a Xenon (Xe) lamp for 97 days for a dislocation-climb experiment. The optical power of the Xe lamp is approximately 16 W/cm^2 with an appropriate lens.

The conditions of the first and the second experiments are shown in Tables 3.1 and 3.2, respectively. The principal difference between the first and the second experiment is in

the use of transverse laser modes. For the first experiment, either TEM_{01} or TEM_{10} modes are used, while a very high order mode is used for the second experiment. The transverse laser modes are shown in Fig 3.9.

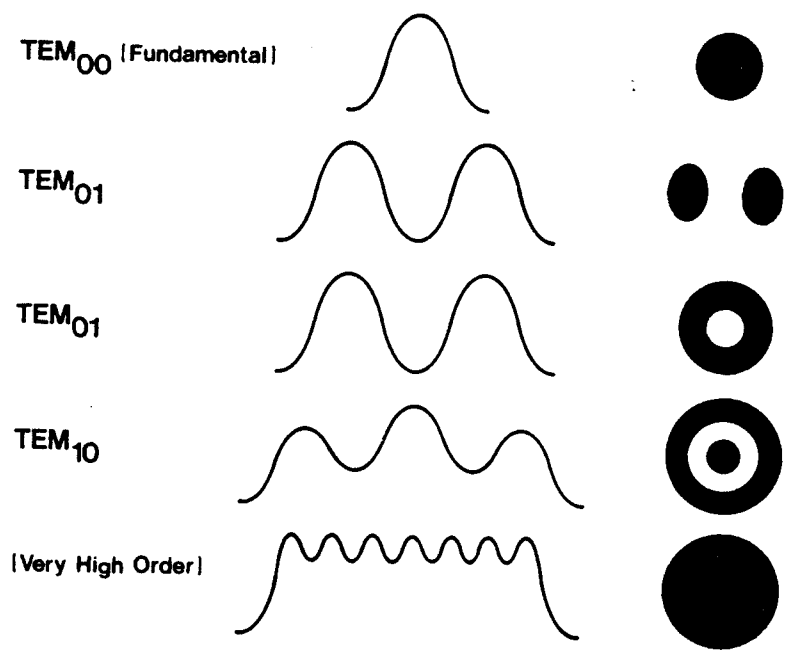

Figure 3.9. Transverse laser modes.

Table 3.1. Conditions for the first experiment.

		Samples								
		ASIS	NO16	NO3	NO17	OPTXE	NO10AS	NO10	ODL56	ODL34
Glide	beam waist	N/A	50 um	50 um	50 um	50 um	N/A	50 um	N/A	N/A
	power density	N/A	6.1×10^4 w/cm^2	7.1×10^4 w/cm^2	6.4×10^4 w/cm^2	4.5×10^4 w/cm^2	N/A	5.5×10^4 w/cm^2	N/A	N/A
	scanning speed	N/A	30 um/sec	30 um/sec	40 um/sec	30 um/sec	N/A	30 um/sec	N/A	N/A
	vert. step size	N/A	40 um	40 um	40 um	40 um	N/A	40 um	N/A	N/A
Climb	beam waist	N/A	280 um	280 um	280 um	~ 1 mm	N/A	N/A	N/A	280 um
	power density	N/A	2436 w/cm^2	2270 w/cm^2	2740 w/cm^2	16 w/cm^2	N/A	N/A	N/A	3400 w/cm^2
	radiation time	N/A	5 hrs	10 hrs	20 hrs	97 days	N/A	N/A	N/A	2 hrs
	total given energy	N/A	44 MJ/cm^2	88 MJ/cm^2	197 MJ/cm^2	134 MJ/cm^2	N/A	N/A	N/A	24.5 MJ/cm^2

Notes:

1) The laser beam is scanned twice for the NO17 sample.
2) The static beam is used for the climb process.
3) The Schottky contact area is 1.5×10^{-4} cm^2 for all samples, with the exception of samples ODL34 and ODL56. Each contact area of the samples ODL34 and ODL45 is 2×10^{-4} cm^2. Three contacts are connected in parallel.

Table 3.2. Conditions for the second experiment.

		Samples		
		DL0HR	DL5HR	DL10HR
Glide	beam waist	N/A	30 um	30 um
	power density	N/A	8.7×10^4 w/cm^2	8.7×10^4 w/cm^2
	scanning speed	N/A	40 um/sec	40 um/sec
	vert. step size	N/A	40 um	40 um
Climb	beam waist	N/A	280 um	280 um
	power density	N/A	1360 w/cm^2	1360 w/cm^2
	radiation time	N/A	5 hrs	10 hrs
	total given energy	N/A	25 MJ/cm^2	50 MJ/cm^2

The surface of the dislocation-glide and -climb samples are inspected with an optical microscope and scanning electron microscope (SEM) to determine whether or not the surface is damaged by the irradiation. The samples are then sent to R. Matson of the Solar Energy Research Institute (SERI) in Golden, Colorado for cathodoluminescence (CL) and electron beam induced current (EBIC) analysis to verify whether or not dislocation-glide and -climb had occurred.

The width of the laser beam waist is determined by a razor blade method. The laser beam is shaded by a razor blade edge installed on the micrometer stage, and the optical power throughput as a function of position is measured by a power meter. The beam size is taken from the positions of a micrometer corresponding to the optical power meter readings of 15 to 85% of the maximum optical power.

3.2.2. Schottky Barrier Diode Fabrication

For electrical characterization of the samples, a Schottky barrier diode is fabricated, as shown in Fig 3.10.

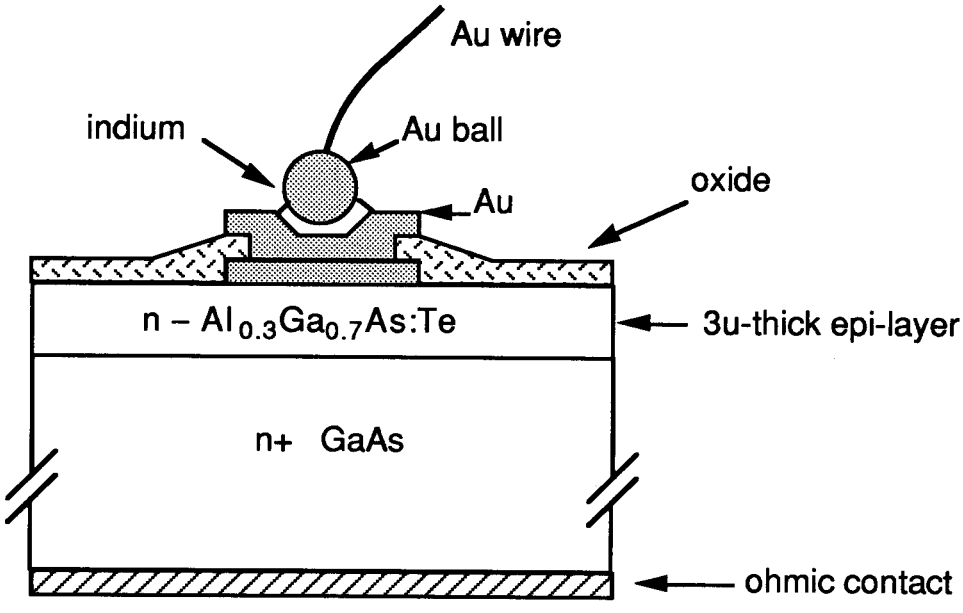

Figure 3.10. Schottky barrier diode structure.

A lift-off process is employed to define the Schottky contact on the sample. To fabricate a Schottky diode for the dislocation-glided and -climbed samples, a complicated process was necessary since a considerable amount of time is required to provide new dislocation-glided and -climbed samples if the Au wire bonding step fails (i.e., the Au layer could peel off during the bonding process unless a bonding

pad is formed on a deposited oxide). The steps required to fabricate the Schottky diode are shown in the Procedure 3.3.

Procedure 3.3. Schottky barrier diode fabrication steps:

1. Start with a lift-off process (refer to Procedure 3.2).
2. Deposition of silicon dioxide (SiO_2) on samples.
3. Spin HMDS onto the sample at 4000 rpm.
4. Spin photoresist onto the sample at 4000 rpm.
5. Softbake for 6 min. at 60°C.
6. Expose the sample to a mercury lamp for 9 seconds.
7. Hardbake the sample for 6 min. at 120°C.
8. Wet etch the sample in buffered HF for 1 min.
9. Rinse the sample with DI water and completely dry with N_2.
10. Lift-off process (refer to Procedure 3.2).
11. Evaporation of Ti and Au.
12. Dip the sample in an acetone bath (lift-off process).
13. Mount the sample on the DIP, using silver paste.
14. Au wire bonding.

The Schottky barrier diodes fabricated, listed in Tables 3.1 and 3.2, are electrically characterized by following methods:

a) Capacitance - voltage (C-V).
b) Deep level transient spectroscopy (DLTS).
c) Deep level admittance spectroscopy (DLAS).
d) Thermally stimulated capacitance (TSCAP).
e) Current - voltage (I-V).

3.2.3. Electrical Characterization

3.2.3.1. Capacitance - voltage measurements

To compare the net ionized positive charge concentration before and after optical-processing of the samples, high frequency C-V measurements are conducted for the Schottky diodes samples listed in Tables 3.1 and 3.2 at room (300°K) and cryogenic (30°K) temperatures by using an HP4280A 1MHz fast capacitance meter. Data acquisition is performed using an HP9326 desktop computer, which is interfaced to the capacitance meter and the temperature controller via an HP-IB bus. A schematic diagram of the C-V measurement setup is shown in Fig. 3.11.

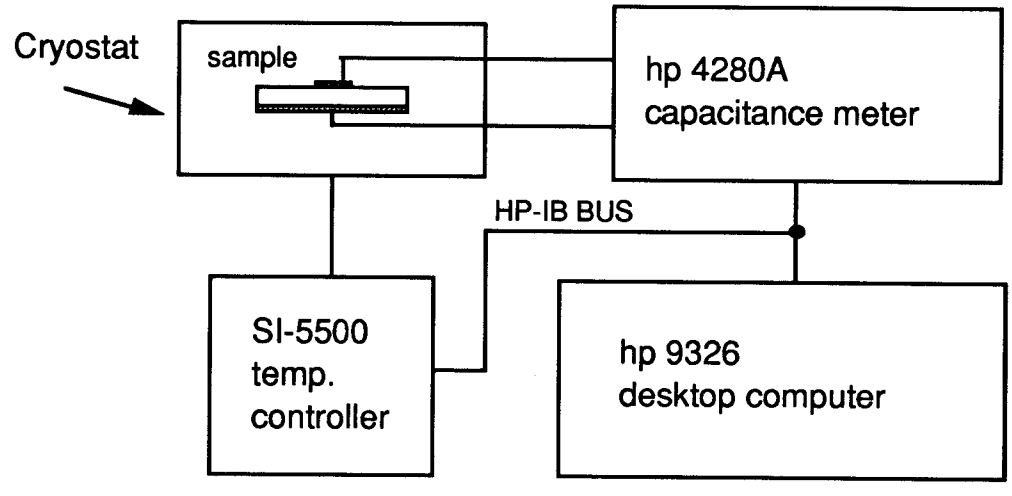

Figure 3.11. Schematic diagram for the C-V measurement setup.

The C-V meter internal voltage source is used to sweep the voltage from -3 V --> 0.1 V --> -3 V. The voltage incremental step is 0.1 V with a delay time of 0.1 second. The net ionized positive charge concentration of the sample is deduced from the slope of a $1/C^2$ - V plot while the built-in potential is deduced by extrapolating to the voltage abscissa and finding the intersection. A room temperature $1/C^2$ - V plot for $Al_{0.3}Ga_{0.7}As$:Te is shown in Fig. 3.12.

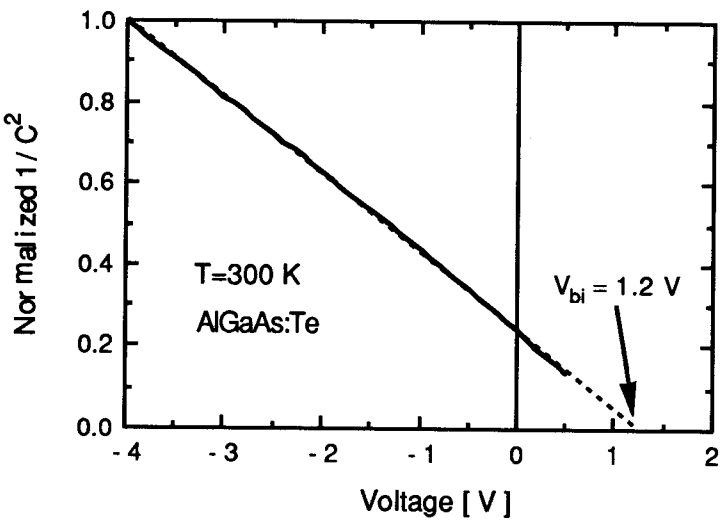

Figure 3.12. Room temperature $1/C^2$ vs. V plot for $Al_{0.3}Ga_{0.7}As$:Te.

The DX concentration profile plot was obtained using following formula [98],

$$N^+(x) = \frac{C^3}{q\,\varepsilon_s\,\varepsilon_o\,A^2}\,\frac{1}{\frac{dc}{dv}} \quad \text{and} \quad x = \frac{A\,\varepsilon_s\,\varepsilon_o}{C} \quad ,$$

where C = capacitance measured at different voltages.

q = electron charge.

ε_s = dielectric constant of the AlGaAs.

ε_0 = permittivity of free space.

A = Schottky contact area.

3.2.3.2. Deep Level Transient Spectroscopy Measurements

DLTS measurements [99-102] are performed on the samples listed in Tables 3.1 and 3.2 to cross-check with the DX concentrations obtained from C-V measurements. A schematic diagram of the DLTS setup is shown in Fig. 3.13. It consists of a pulse generator, a pulse bias noise clipper, an 1MHz fast capacitance meter, a dc power supply, a temperature controller, a helium closed-cycle cryostat, and an HP9326 desktop computer. The computer is interfaced to the pulse generator, the capacitance meter, and the temperature controller via an HP-IB bus.

The sample is mounted on the cold head of a helium closed-cycle cryostat. A negative bias of -1 V is applied to the Schottky barrier diode during the sample cooling. The temperature is scanned from 110 to 350°K using a temperature step of 3°K. A positive-going pulse (i.e., filling-pulse), whose height and width are 1.3 V and 50 msec, respectively,

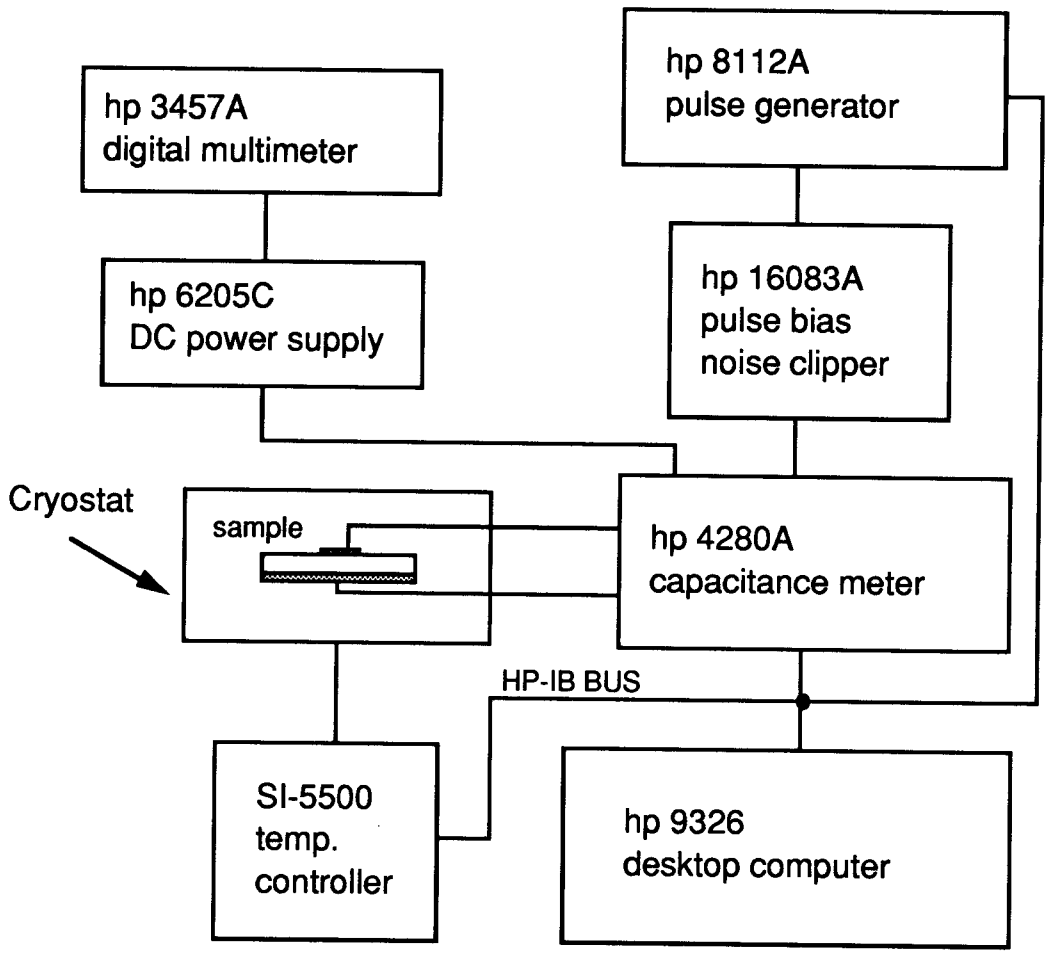

Figure 3.13. Experimental setup for DLTS measurements.

is applied to the Schottky sample prior to taking the capacitance transient data. The effective pulse height applied to the sample is 1.0 V since 0.3 V is dropped across the pulse bias noise clipper.

A diagram illustrating the charge density variations prior to, during, and following the filling-pulse is shown in Fig. 3.14. The solid lines represents the initial ($t<0^-$) and

final (t=∞) charge densities in the space-charge region of the sample. The depletion- and transition-region widths shrinks ((i) in Fig. 3.14) when the filling pulse is applied to the sample since the sample momentarily forward biased. A majority of the traps are filled with carriers during the filling pulse duration of 50 msec since the carrier capture time ($1/C_n \approx$ nano-seconds) is much shorter than the pulse duration time. The fine dotted line shown in Fig. 3.14 indicates the charge density during the filling pulse.

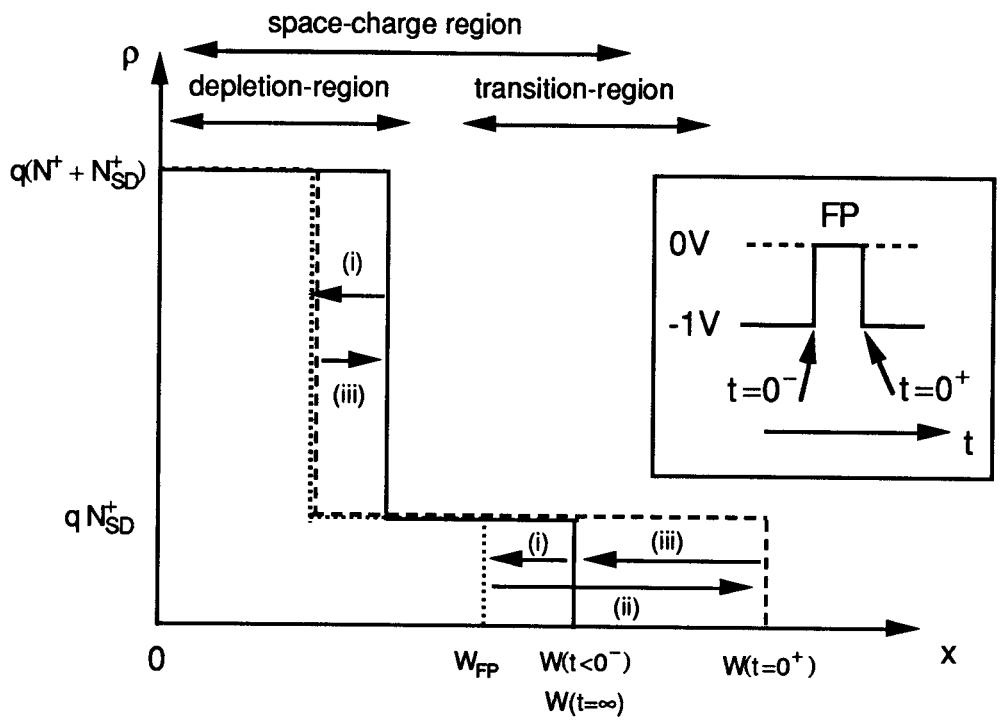

Figure 3.14. Illustration of the charge density variation prior to, during, and following the filling pulse.

The broken line represents the charge density at the falling edge (i.e., $t=0^+$ in the inset of Fig. 3.14) of the pulse. As soon as the filling pulse is removed, the shallow donor transition region expands (ii) to satisfy charge neutrality since the emission rate of the carriers trapped within the depletion region is small. That is, electrons trapped in deep states are slowly emitted to the conduction band. This slow electron emission in the depletion region causes both the depletion region expansion (iii) and the transition region shrinkage (iii), leading to capacitance transients as shown in Fig. 3.15.

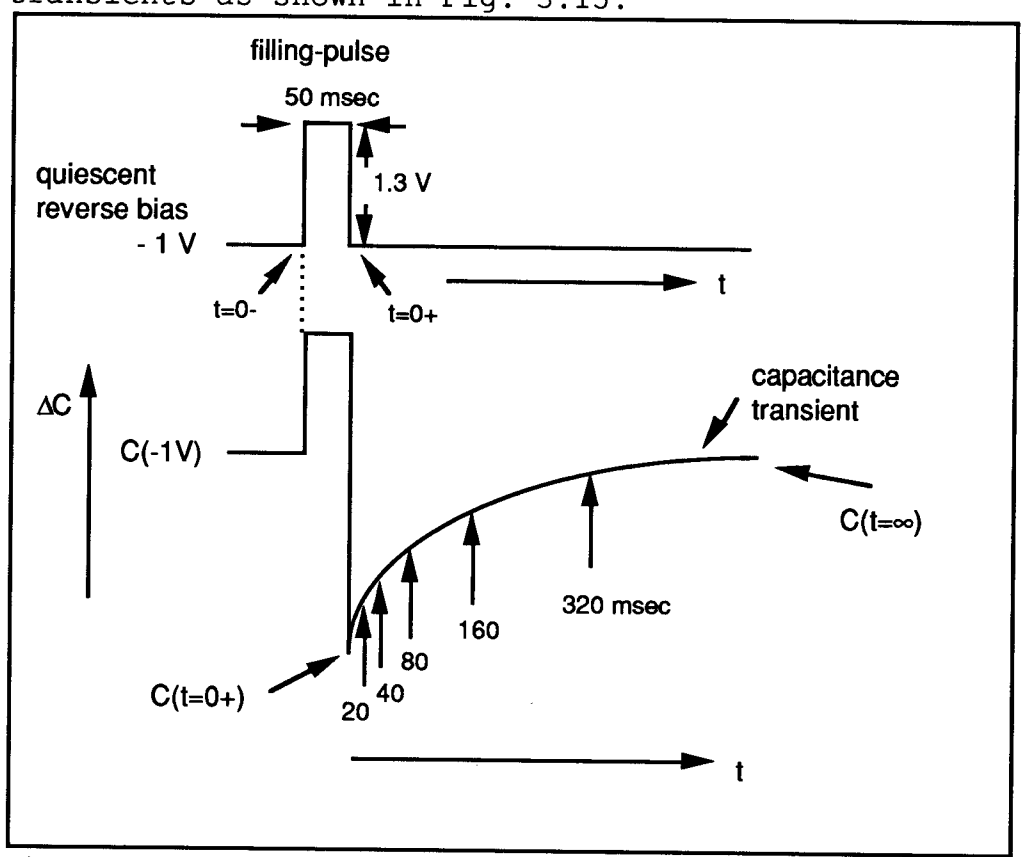

Figure 3.15. Capacitance transient following a filling-pulse. The capacitance transients are measured at time intervals of 20, 40, 80, 160, and 320 msec.

The capacitance transients are measured using an 1MHz fast capacitance meter at time intervals of 20, 40, 80, 160, and 320 msec and at different temperatures. In general, due to the violation of the normal DLTS assumptions the capacitance transients are nonexponential which can be caused by one or a combination of following [103]:

a) Deep level concentration comparable to the shallow donor concentration.

b) Nonuniform doping.

c) Nonabrupt junction.

d) Poole-Frenkel or tunneling effects.

To increase the signal-to-noise ratio, the capacitance transient is averaged 100 times at each temperature. The signal averaged capacitance transient is then stored and subsequently processed using the HP 9326 computer to obtain a DLTS signal and an Arrhenius plot. A DLTS spectra of the DL0AS sample for three different rate windows, 34.7, 17.3, and 8.7 sec^{-1}, is shown in Fig. 3.16.

For an n-type semiconductor the emission probability of electrons, e_n, is given by [104]

$$e_n = \sigma_n \upsilon_{th} N_c \exp(-E_A/k_BT)$$

where k_B is Boltzmann's constant, σ_n is the carrier capture cross-section, υ_{th} is the electron thermal velocity, N_c is the effective density of states of the conduction band, and E_A is

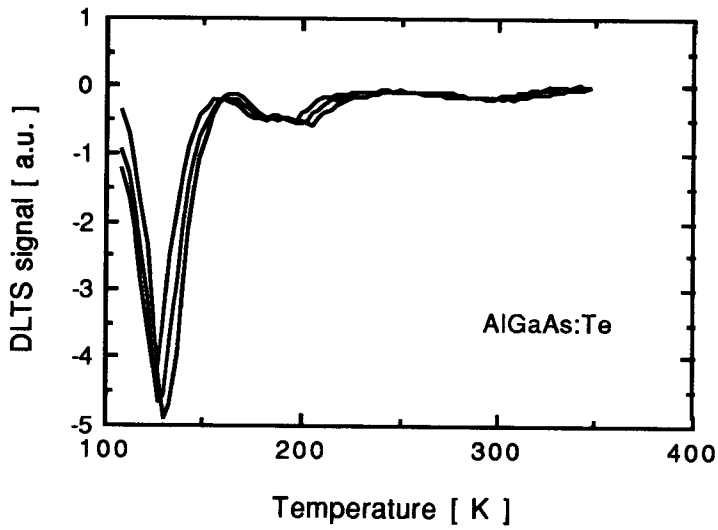

Figure 3.16. DLTS spectra of the DL0HR sample for three different rate windows, 34.7, 17.3, and 8.7 sec^{-1}.

the activation energy. The activation energy is defined as the energy separation between the conduction band and the trap level. A semi-log plot of emission probability normalized by the square of the temperature versus the inverse temperature (i.e., $\ln(e_n/T^2)$ vs. $1/T$) is called an Arrhenius plot.

Activation energy and capture cross-section of the DX center are deduced from the Arrhenius plot. The DX center concentration is estimated from the DLTS signal height and the area. Conventionally, the trap concentration, N_T, can be obtained from following formula [98],

$$N_T = \frac{2\ \Delta C}{C}\ (N_D^+ - N_A^-),$$

where $\Delta C = |C(\infty)-C(0+)|$,

C = room temperature capacitance, and

$(N_D^+ - N_A^-)$ = net positive charge concentration, which can be measured by the C-V technique. However, it should be noted that the above formula is valid only for $N_T << (N_D^+ - N_A^-)$ (see Appendix A).

3.2.3.3. Deep Level Admittance Spectroscopy Measurements

DLAS measurements [105-110] are conducted to cross-check the DX center concentrations obtained from C-V and DLTS measurements. The DLAS setup is shown in Fig. 3.17. It consists of an HP 4192A low frequency impedance analyzer, a temperature controller, a helium closed-cycle cryostat, and an HP9326 computer. The variable frequency of the analyzer ranges from 5 Hz to 13 MHz while its amplitude (i.e., oscillator (OSC) level) can be varied from 5 mV to 1 V.

The sample is mounted on the cold head of the cryostat, and is cooled down to 30°K in the dark. The temperature is scanned from 30 to 300°K using temperature steps of 2 or 3°K. The employed OSC level is 30 mV. The conductance (G) is measured as a function of frequency (i.e., 1000, 500, 250,

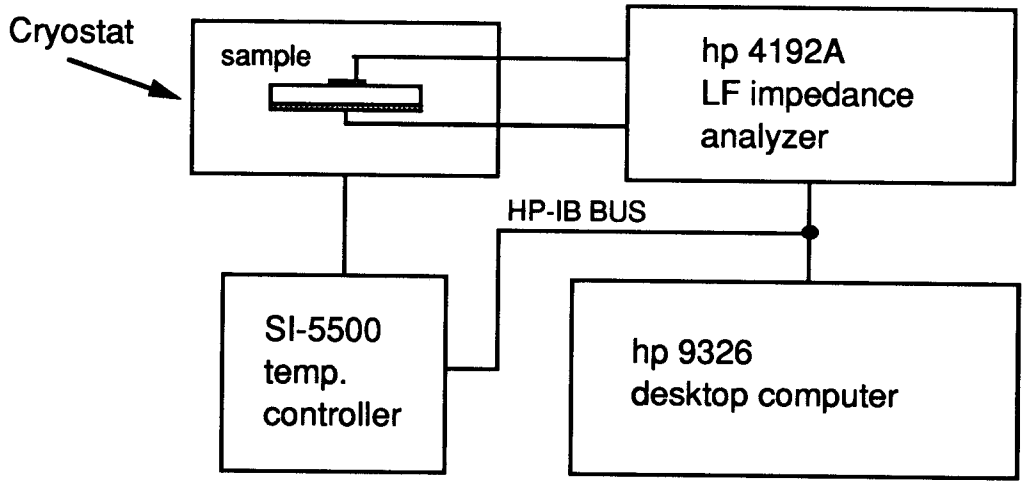

Figure 3.17. Experimental setup for DLAS measurements.

100, 50, 10, 5, and 1 kHz) at each fixed temperature. Conductance versus temperature (G-T) curves for a sample subjected to no optical-processing is shown in Fig. 3.18. Conductance-peaks appear when the applied frequency is equal

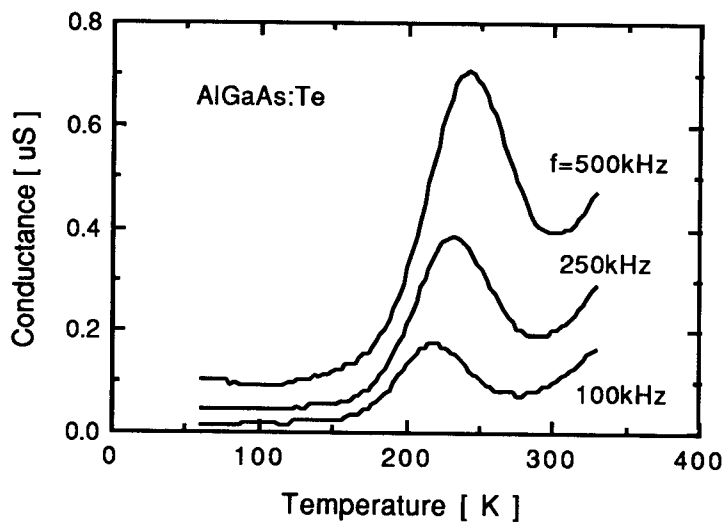

Figure 3.18. DLAS spectra of the DL0AS sample.

to the DX center emission probability (i.e., $\omega \approx e_n$).

The activation energy of the DX center is obtained from the slope of the Arrhenius plot and the capture cross-section from the intercept. The DX center concentrations of optically-processed samples and samples not subjected to any optical-processing are evaluated by comparing the conductance peak and area.

There are some differences between the DLTS and DLAS techniques for the detection of trap levels. That is, DLTS is a transient technique while DLAS is a steady-state measurement. The DLTS technique is best suited to the detection of midgap trap levels while the DLAS technique is primarily used for the detection of the shallow levels. The DLAS technique is insensitive to sample leakage since only the conductance peak temperature, T_p, is required to deduce the activation energy and capture cross-section. For a leaky sample the base line of the conductance curve is shifted to a higher value.

3.2.3.4. Thermally Stimulated Capacitance Measurements

TSCAP measurements [9] are conducted as a means of comparison of the DX center concentration obtained from C-V, DLTS, and DLAS measurements. The TSCAP setup is identical to the DLAS setup shown in Fig. 3.17. TSCAP traces for the NO17

sample are illustrated in Fig. 3.19. Curve 1 represents a reversible trace of capacitance where the sample is cooled and warmed at zero bias in the dark. Curve 2 shows the behavior of warming the sample at zero bias after the sample had been cooled at a bias of +0.9V. The bias condition of curve 3 is the same as curve 1, but the sample is illuminated with monochromatic light (~ 1.54 eV) during cooldown. At 30 K, the capacitance does not recover to the initial dark state even when the light is turned off. When the diode is warmed to ~ 100 K, the capacitance recovers to the dark state.

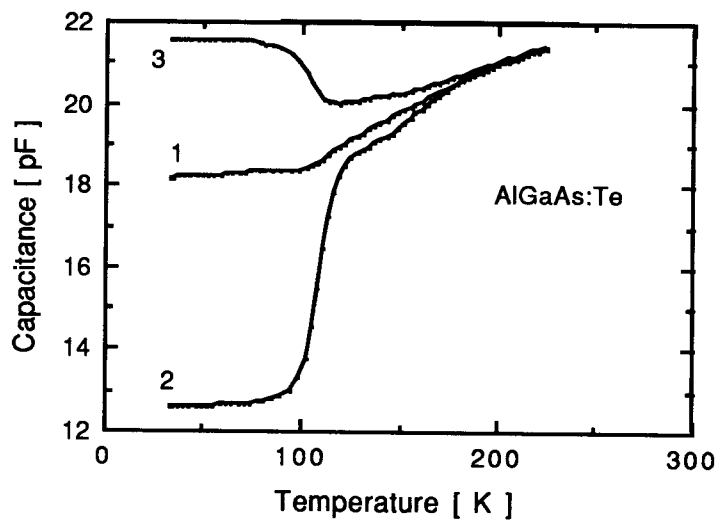

Figure 3.19. TSCAP traces for the NO17 sample. Cooling conditions are as follows: curve 1; in the dark at zero bias, curve 2; in the dark at zero bias after being cooled at a bias of +0.9 V, and curve 3; the same condition as curve 1, but illuminated with a photon energy of 1.54 eV during cooldown.

The DX concentration is estimated from the TSCAP measurements using the formula [9],

$$\frac{N_{DX}}{n} = \left(\frac{C_3}{C_2}\right)^2 - 1$$

where C_2 and C_3 indicate the 30 K capacitance of curve 2 and 3, respectively.

3.2.3.5. Current versus Voltage Measurements

The room and low (77 K) temperatures I-V measurements were conducted for the samples listed in Tables 3.1 and 3.2 using a HP 4145B semiconductor parameter analyzer.

Chapter 4. Minority Carrier Capture: Experimental Results and Discussion

4.1. Theoretical Background

In the current investigation, the MCC concept was applied to Te-doped $Al_xGa_{1-x}As$ and Si-doped $Al_xGa_{1-x}As$ in order to measure the low temperature hole capture cross-section of the DX center and to thus identify the DX center charge state at low temperature (e.g., below 80 K). The basic principle of the MCC technique is illustrated in Fig. 4.1.

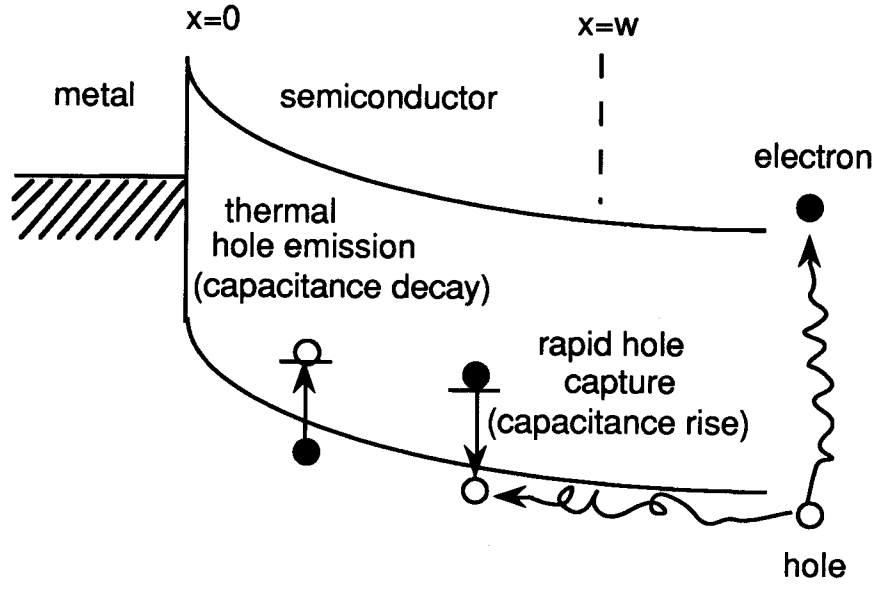

Figure 4.1. Basic principle of minority carrier capture [111].

When a zero- or reverse-biased Schottky barrier is uniformly illuminated with near-band-gap light, a short circuit photocurrent, composed of recombination and diffusion currents, is produced. The recombination current is generated when incident, above-bandgap photons create electron-hole pairs which, if created near the surface, are separated by the field in the space-charge region. Electron-hole pairs created within a diffusion length of the space-charge region edge can also contribute to the photocurrent if the photo-induced minority carrier diffuses into the space-charge region and then drifts across the space-charge region to the metal interface to contribute to a diffusion current. In n-type semiconductors only the holes (i.e., the minority carriers) diffuse into the space-charge region whereas the electrons are repelled by the potential barrier. Accordingly, the short circuit photocurrent is dominated by the diffusion current component as long as the minority carrier diffusion length is much larger than the width of the space-charge region, $L_p >> W$.

As shown in Fig. 4.1, the charge state of the deep levels, which are initially occupied by electrons in the space-charge region, is changed by the capture of injected holes. The hole-capture transient is monitored by measuring the capacitance transient with a high-frequency capacitance meter since positive charge builds up in the space-charge region. Thus, the depletion region shrinks and the capacitance increases.

Excitation of the Schottky diode with weakly absorbing near-band-gap light can result in several excitation processes. These interactions are shown in Fig. 4.2, with corresponding transition rate parameters listed in Table 4.1. In Fig 4.2, thermal and optical processes are indicated by straight and waved lines, respectively. The processes are described as follows:

Process 1: Optical absorption within a diffusion length of the barrier creating an excess hole population inside the barrier region.

Process 2: Optical absorption in the barrier creating electron-hole pairs separated by the field.

Process 3: Holes created by process 1 are captured by the electron-filled state (i.e., the most desirable outcome in MCC experimentation).

Process 4: Electrons created by process 2 are captured by empty (hole-filled) states.

Process 5: Direct electron photoionization.

Process 6: Direct hole photoionization.

Process 7: Thermal ionization of electrons.

Process 8: Thermal ionization of holes.

Note that processes 4, 6, and 8 tend to cause negative charge build-up in the depletion layer. Accordingly, the depletion width expands and the capacitance decreases. Conversely, processes 3, 5, and 7 tend to cause positive charge build-up

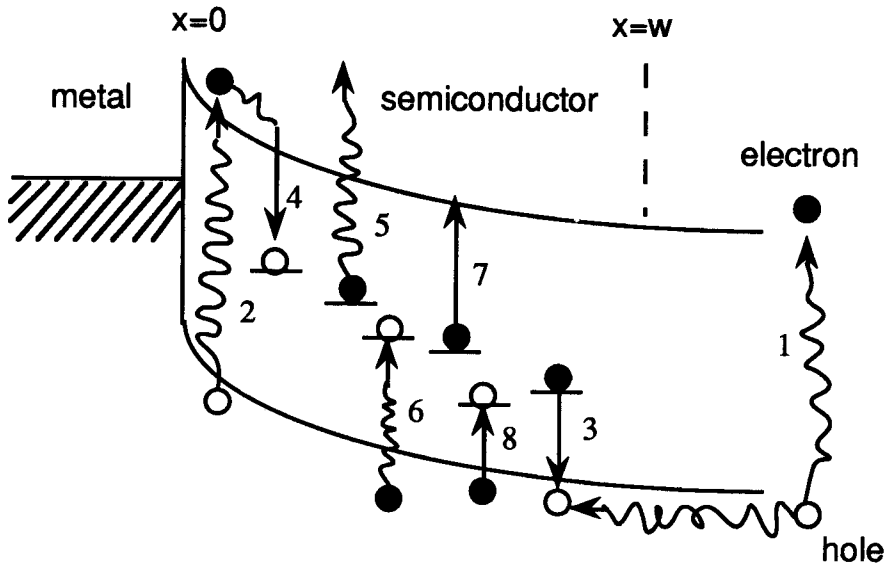

Figure 4.2. Optical interactions resulting from near bandgap illumination [111].

Table 4.1. Notation for transition probabilities corresponding to the optical interactions shown in Fig. 4.2 [111].

Transition	Process	Transition Probability per unit Time
Optical absorption	1 & 2	Proportional to $\phi\,\alpha$
Hole capture	3	$C_p = \sigma_p\, V_{th}(h^+)\, \Delta p$
Electron capture	4	$C_n = \sigma_n\, V_{th}(e^-)\, \Delta n$
Electron photoionization	5	$e_n^o = \phi\, \sigma_n^o$
Hole photoionization	6	$e_p^o = \phi\ \sigma_p^o$
Electron thermal ionization	7	$e_n^t = \sigma_n\, V_{th}\, N_c \exp\left(\frac{-(E_c - E_T)}{k_B\, T}\right)$
Hole thermal ionization	8	$e_p^t = \sigma_p\, V_{th}\, N_v \exp\left(\frac{-(E_T - E_v)}{k_B\, T}\right)$

in the depletion layer. Thus, the depletion width shrinks and the capacitance increases. In Table 4.1, standard notation is used, where ϕ and α denote, respectively, the photon flux and the absorption coefficient. The incremental values Δn and Δp denote excess carrier densities produced by the photocurrent.

If the total concentration of the deep level is N_T, then $N_T = n_T + p_T$, where n_T and p_T are, respectively, the instantaneous concentration of trapped electrons and holes. If the illumination activates all of the processes listed in Table 4.1, then the rate of change of trapped electron density, $\frac{dn_T}{dt}$, will be

$$\frac{dn_T}{dt} = \text{(processes involving an increase in the trapped } e^- \text{ concentration) - (processes involving a decrease in the trapped } e^- \text{ concentration)},$$

$$\frac{dn_T}{dt} = \text{(process 8 + process 6 + process 4) - (process 7 + process 5 + process 3)},$$

and

$$\frac{dn_T}{dt} = (e_p^t + e_p^o + c_n\Delta n)p_T - (e_n^t + e_n^o + c_p\Delta p)n_T \qquad (4\text{-}1)$$

where c_n and c_p are, respectively, the electron and hole capture rates and Δn and Δp denote the excess carrier densities produced by the photocurrent and the superscripts, t and o, denote thermal and optical processes, respectively. At temperatures below 80 K, the thermal ionization processes are ignored and $e_p^t = e_n^t \approx 0$. Note that in contrast to silicon and other binary compound semiconductors, process 6, hole

photoionization, does not occur for AlGaAs even after DX is ionized because of large lattice relaxation. That is, the PPC effect cannot be optically quenched, as observed by Nelson [2]. Accordingly, process 6 can be ignored and $e_p^o \approx 0$. If the hole diffusion length, L_p, is much larger than the space-charge width, W, then the diffusion component of the photocurrent dominates and $\Delta p >> \Delta n$. It is generally accepted that the electron capture cross-section (σ_n) of DX centers at low temperature is extremely small (hence, PPC occurs). Thus, the hole capture rate (process 3) dominates over the electron capture rate (process 4) and $c_p \Delta p >> c_n \Delta n$.

Given the above conditions, the rate equation (4-1) can be rewritten as

$$\frac{dn_T}{dt} = - (e_n^o + c_p \Delta p) \cdot n_T \qquad (4-2)$$

which can be solved to obtain

$$\ln n_T = - \frac{t}{\tau_1} + c \quad \text{where } \tau_1 = \frac{1}{e_n^o + c_p \Delta p} . \qquad (4-3)$$

The boundary condition of relevance is $n_T = N_T$ at $t = 0$; that is, the DX centers are filled with electrons. This condition can be achieved by application of a forward bias to the sample as it is cooled. Thus,

$$c = \ln N_T \qquad (4-4)$$

and

$$\ln n_T = - t/\tau_1 + \ln N_T . \tag{4-5}$$

Then, taking the exponential of both sides,

$$n_T = N_T \, e^{-t/\tau_1} \tag{4-6}$$

and

$$n_T = N_T - p_T . \tag{4-7}$$

Combining eqn. (4-6) and eqn. (4-7) yields

$$\frac{N_T - p_T}{N_T} = e^{-t/\tau_1} , \tag{4-8}$$

and

$$p_T(t) = N_T \, (1 - e^{-t/\tau_1}) . \tag{4-9}$$

The charge exchange kinetics are reflected directly in the high frequency capacitance per unit area of the barrier:

$$C(t) = \left(\frac{\varepsilon \, \rho^+(t)}{2 \, (V_{bi} \pm V)} \right)^{1/2} = B \, (\rho^+(t))^{1/2} = Bq^{1/2}[N^+_{net} + p_T(t)]^{1/2},$$

where

$$B = \left(\frac{\varepsilon}{2 \, (V_{bi} \pm V)} \right)^{1/2} \text{ and } \rho^+(t) = q \, [N^+_{net} + p_T(t)], \tag{4-10}$$

and where ρ^+ is the net positive space charge density in the space charge region, $V_{bi} \pm V$ is the total potential drop across the barrier, and N^+_{net} is the net positive charge concentration in equilibrium. When $t = 0$, that is, before turning on the light, $C(t)$ will be

$$C(0) = B \, q^{1/2} (N^+_{net})^{1/2} \tag{4-11}$$

since $n_T = N_T$ at $t = 0$, and $p_T = 0$.

Next, a expression for capacitance may be obtained from equns. (4-10) and (4-11) to give,

$$\frac{C^2(t) - C^2(0)}{C^2(0)} = \frac{B^2q\,[N^+_{net} + p_T(t)] - B^2q\,N^+_{net}}{B^2q\,N^+_{net}} = \frac{p_T(t)}{N^+_{net}} \,. \tag{4-12}$$

When the left term of eqn. (4-12) is manipulated, then

$$\frac{C^2(t) - C^2(0)}{C^2(0)} = \frac{[C(t) - C(0)]^2 + 2C(0)C(t) - 2C^2(0)}{C^2(0)} \,. \tag{4-13}$$

Let the capacitance change, $\Delta C(t)$, be defined as $\Delta C(t) = C(t) - C(0)$; then

$$\frac{C^2(t) - C^2(0)}{C^2(0)} = \frac{\Delta C^2(t) + 2C(0)C(t) - 2C^2(0)}{C^2(0)} \,, \tag{4-14}$$

which leads to two limiting cases. First, if the capacitance change is much less than the initial capacitance, i.e., $\Delta C(t) \ll C(0)$, then the expression can be simplified as

$$\frac{C^2(t) - C^2(0)}{C^2(0)} \approx \frac{2\,\Delta C(t)}{C(0)} = \frac{p_T(t)}{N^+_{net}} \,. \tag{4-15}$$

Therefore, the capacitance change as a function of time is expressed as

$$\Delta C(t) = \frac{1}{2}\,C(0)\,\frac{p_T(t)}{N^+_{net}} \,. \tag{4-16}$$

Second, if the capacitance change is greater than the initial capacitance, $\Delta C(t) > C(0)$, then the expression is

$$\frac{C^2(t) - C^2(0)}{C^2(0)} = \frac{\Delta C^2(t) + 2\ \Delta C(t)C(0)}{C^2(0)} = \frac{p_T(t)}{N^+_{net}} \qquad (4\text{-}17)$$

and the capacitance change as a function of time is expressed as

$$\Delta C^2(t) + 2\ \Delta C(t)C(0) = C^2(0)\ \frac{p_T(t)}{N^+_{net}}\ . \qquad (4\text{-}18)$$

For the current investigation, the capacitance change is larger than the initial capacitance. Thus, from eqns. (4-9) and (4-18),

$$\Delta C^2(t) + 2\ \Delta C(t)C(0) = \frac{N_T}{N^+_{net}}\ C^2(0)\ (1-e^{-t/\tau_{r1}}) \qquad (4\text{-}19)$$

where $\tau_{r1} = (e^{\circ}_n + c_p\Delta p)^{-1} \equiv$ capacitance rise-time measured under near-bandgap illumination (i.e., illumination at a photon energy slightly above bandgap where the absorption depth is large, ensuring that carrier generation occurs in the semiconductor bulk). The hole capture rate, c_p, can be expressed as,

$$c_p = \upsilon_{th}(h^+)\cdot\sigma_p \qquad (4\text{-}20)$$

so that

$$\tau_{r1}^{-1} = e_n^{\circ} + \upsilon_{th}(h^+)\cdot\sigma_p\cdot\Delta p \ . \qquad (4\text{-}21)$$

Solving eqn. (4-21) for the hole capture cross-section, σ_p, gives,

$$\sigma_p(T) = \frac{\tau_{r1}^{-1} - \tau_{r2}^{-1}}{\upsilon_{th}(h^+)\cdot\Delta p} \ , \qquad (4\text{-}22)$$

where τ_{r2}^{-1} is defined as e_n° . τ_{r2} is the measured capacitance rise-time under sub-bandgap illumination. In eqn. (4-22), τ_{r1} and τ_{r2} are experimentally measurable values, while $\upsilon_{th}(h^+)$ is the hole thermal velocity expressed by

$$\upsilon_{th}(h^+) = \sqrt{\frac{3\ k_B T}{m_p^*}} \ ,$$

where k_B = Boltzmann's constant and m_p^* = the effective mass of the hole.

It is then necessary to determined the injected hole concentration, Δp. If the hole diffusion length, L_p, is much larger than the depletion width, then the short-circuit current, J_{sc}, is considered to be composed of just diffusion current. Therefore,

$$J_{sc} = q\ D_p \left.\frac{dp}{dx}\right|_{x=0} \quad \text{where} \quad p = \Delta p\ e^{-x/L_p} \ , \qquad (4\text{-}23)$$

and

$$\left|\frac{dp}{dx}\right|_{x=0} = \left|\Delta p\cdot\left(-\frac{1}{L_p}\right)\cdot e^{-x/L_p}\right|_{x=0} = \frac{\Delta p}{L_p} \ . \qquad (4\text{-}24)$$

Thus, the short-circuit current density can be expressed as

$$J_{sc} = q\ \Delta p\ \frac{D_p}{L_p} \quad \text{where} \quad L_p = (D_p \tau_p)^{1/2} \tag{4-25}$$

therefore,

$$J_{sc} = q\ \Delta p \left(\frac{D_p}{\tau_p}\right)^{1/2} \tag{4-26}$$

and

$$\Delta p = \frac{J_{sc}}{q\ (D_p/\tau_p)^{1/2}} \tag{4-27}$$

Finally, the hole capture cross-section is obtained by combining eqn. (4-22) and eqn. (4-27), and is expressed as

$$\sigma_p(T) = \frac{q\ (\ \tau_{r1}^{-1} - \tau_{r2}^{-1}\ )\ (\ D_p/\tau_p\ )^{1/2}}{\upsilon_{th}(h^+)\ J_{sc}} \tag{4-28}$$

where τ_{r1} = capacitance rise time under near-bandgap illumination,

τ_{r2} = capacitance rise time under sub-bandgap illumination,

τ_p = minority carrier lifetime,

$\upsilon_{th}(h^+)$ = thermal velocity of holes,

D_p = hole diffusivity ($\mu_p\ k_B\ T/q$), and

J_{sc} = short-circuit current density.

Equation (4-28) is the expression used to evaluate the low temperature hole capture cross-section in the MCC experiment.

4.2 Experimental Results and Discussion

4.2.1. Low temperature hole capture cross-section evaluation

To evaluate the low temperature hole capture cross-section using eqn. (4-28), the parameters τ_{r1}, τ_{r2}, τ_p, $\upsilon_{th}(h^+)$, D_p, and J_{sc} must be determined. The parameters τ_{r1}, τ_{r2}, and J_{sc} are obtained from experiment, while the remaining parameters are obtained as follows. The hole thermal velocity,

$$\upsilon_{th}(h^+) = \sqrt{\frac{3\ k_B T}{m_p^*}} \ ,$$

is evaluated using $m_p^*(x = 0.3) = 0.666 m_0$ and the relevant temperature as summarized in Tables 4.2 and 4.3. The hole diffusivity is estimated using the Einstein relation,

$$D_p = \mu_p\ k_B\ T/q \ ,$$

and the hole mobility is assumed to be dominated by ionized impurity scattering so that μ_p is estimated using the Brooks-Herring equation [112],

$$\mu_p = \frac{64\sqrt{\pi}\ \varepsilon^2\ (2k_B T)^{3/2}}{N_I\ q^3\ \sqrt{m_p^*}} \left[\ln\left\{ \frac{96\pi^2\ m_p^*\ k_B^2\ T^2\ \varepsilon}{q^2\ h^2\ N_I} \right\} \right]^{-1} , \qquad (4\text{-}29)$$

where ε, h, k_B, m_p^*, and q are the dielectric constant, Planck's constant, Boltzmann's constant, the hole effective mass, and the electronic charge, respectively, and N_I is the

total concentration of ionized impurities. Finally, $\tau_p \approx 10$ nsec as reported by Ahrenkiel *et al.* [113].

The capacitance rise times, τ_{r1} and τ_{r2}, under the near- and sub-bandgap illumination are obtained from capacitance transient measurements as shown in Figs. 4.3 and 4.4, respectively, for Te- and Si-doped samples. The rise time is estimated from values of 10% to 90% of the capacitance transient. As can be seen from these figures, τ_{r2} is much longer than τ_{r1} for a Si-doped sample; This is attributed to a small electron photoionization cross-section, σ_n^o, for the Si-doped sample at a sub-bandgap photon energy of 1.38 eV. τ_{r2} and τ_{r1} are related to σ_n^o as $(\phi\ \sigma_n^o)^{-1}$ and $(\phi \cdot \sigma_n^o + \sigma_p \cdot \upsilon_{th}(h^+) \cdot \Delta p)^{-1}$, respectively. The reported values of σ_n^o at sub- and near-bandgap photon energies for a Si-doped $Al_{0.3}Ga_{0.7}As$ [63] are approximately 8×10^{-19} and 1×10^{-17} cm^2, and σ_n^o is insensitive to the Al mole fraction, x [63]. In contrast, σ_n^o at both near- and sub-bandgap photon energies for Te-doped $Al_{0.37}Ga_{0.63}As$ is approximately 4×10^{-17} cm^2 [9]. Thus, for the Si-doped sample, the large value of τ_{r2}, in excess of 150 sec as indicated in Table 4.3, arises from the very small value of σ_n^o for sub-bandgap photoexcitation.

All of the relevant parameters of eqn. (4-28), as well as the calculated capture cross-section for a variety of temperatures, are summarized in Tables 4.2 and 4.3 for Te- and Si-doped samples, respectively. As may be seen from these tables, the hole capture cross-sections evaluated for the Te- and Si-doped samples are approximately 2.0×10^{-19} cm^2 and 1.5

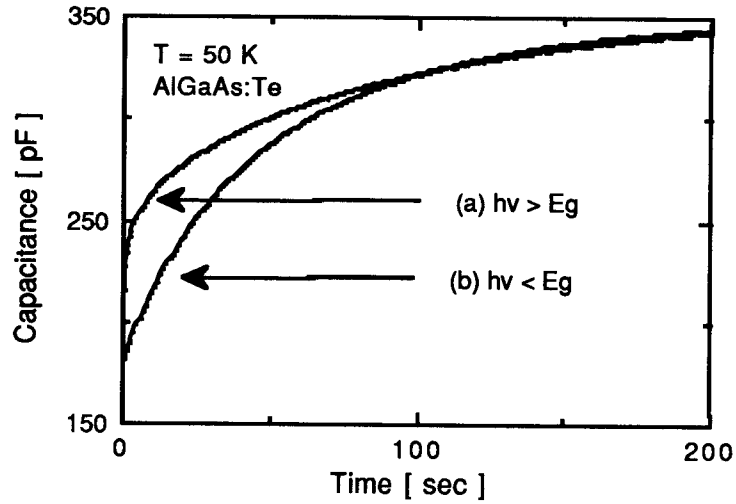

Figure 4.3. Capacitance rise time measured at 50 K for a Te-doped sample: (a) under near-bandgap illumination, hv = 1.97 eV, and (b) sub-bandgap illumination, hv = 1.38 eV. The energy bandgap of the n-$Al_{0.3}Ga_{0.7}As$ at 50 K is 1.94 eV.

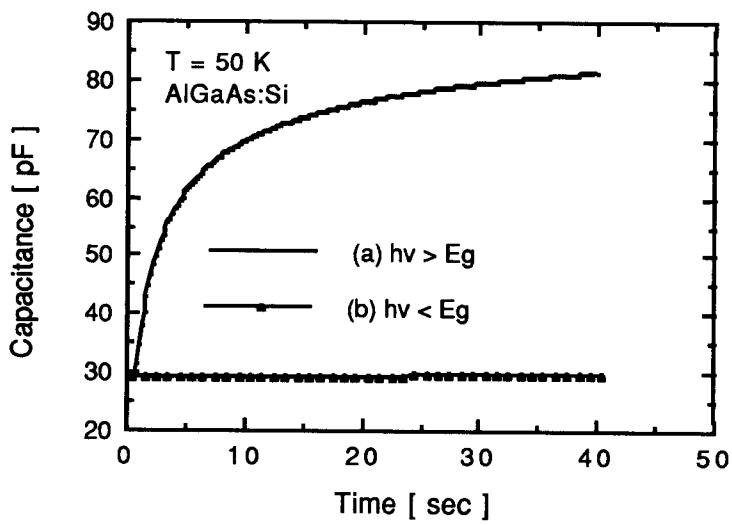

Figure 4.4. Capacitance rise time measured at 50 K for a Si-doped sample: (a) under near-bandgap illumination, hv = 2.07 eV, and (b) sub-bandgap illumination, hv = 1.38 eV.

Table 4.2. MCC experimental results for Te-doped n-$Al_{0.3}Ga_{0.7}As$.

Parameters	Temperature			
	30 K	50 K	60 K	70 K
τ_{r1} (sec)	95.7	99	105.6	108.9
τ_{r2} (sec)	124.3	125.4	128.7	132
J_{sc} (A/cm^2)	1.3×10^{-6}	1.3×10^{-6}	1.3×10^{-6}	1.3×10^{-6}
$\upsilon_{th}(h^+)$ (cm/sec)	4.5×10^{6}	5.8×10^{6}	6.4×10^{6}	6.9×10^{6}
D_p (V^2/cm-sec)	0.102	0.34	0.52	0.75
μ_p (V/cm-sec)	39.5	78.51	100.5	123.9
$\sigma_p(T)$ (cm^2)	2.10×10^{-19}	2.63×10^{-19}	2.36×10^{-19}	2.48×10^{-19}

Table 4.3. MCC experimental results for Si-doped n-$Al_{0.3}Ga_{0.7}As$.

Parameters	Temperature				
	40 K	50 K	60 K	70 K	80 K
τ_{r1} (sec)	20.0	22.7	23.6	20.8	19.0
τ_{r2} (sec)	> 150	> 150	> 150	> 150	> 150
J_{sc} (A/cm^2)	0.35	0.27	0.37	0.45	0.33
$\upsilon_{th}(h^+)$ (cm/sec)	5.2×10^{6}	5.8×10^{6}	6.4×10^{6}	6.9×10^{6}	7.4×10^{6}
D_p (V^2/cm-sec)	0.1526	0.2596	0.4012	0.5797	0.7976
μ_p (V/cm-sec)	44.2	60.2	77.5	96.0	115.6
$\sigma_p(T)$ (cm^2)	1.3×10^{-17}	1.66×10^{-17}	1.3×10^{-17}	1.4×10^{-17}	2.4×10^{-17}

x 10^{-17} cm^2, respectively, and are independent of temperature below ~ 70 K. Thus, while it can be concluded that both Te and Si DX centers have a small cross-section for minority carrier hole capture, there is a discrepancy in the magnitudes of these capture cross-sections.

This discrepancy can be explained in terms of nonradiative recombination by multiphonon emission (MPE) [114]. In general, the MPE capture cross-section, σ, is expressed by [114]

$$\sigma = Af(0) , \qquad (4-30)$$

where A = a term involving only the electronic matrix elements of the transition.

f(hv) = the optical lineshape for phonon-assisted absorption or emission transitions.

The temperature-dependence of MPE capture, f(0) is given by [115]

$$f(0) = \frac{e^{-E_{cap}/k_BT^*}}{\sqrt{4\pi\ E_R k_B T^*}} \qquad (4-31)$$

where E_R = relaxation energy,

E_{cap} = capture barrier, and

T^* = effective temperature.

The effective temperature, T^*, is defined as [114]

$$k_BT^* = \frac{h\omega}{4\pi}\coth\left[\frac{h\omega}{4\pi\ k_BT}\right]. \qquad (4-32)$$

At low temperature, the effective temperature, k_BT^*, is simplified as

$$k_BT^* = \frac{h\omega}{4\pi} , \qquad (4\text{-}33)$$

since

$$\coth\left[\frac{h\omega}{4\pi\ k_BT}\right] \approx 1 \qquad (4\text{-}34)$$

with

$$\frac{h\omega}{4\pi\ k_BT} \gg 1 .$$

Therefore, the MPE low-temperature capture cross-section can be expressed as

$$\sigma_{LT} = \frac{Ae^{-4\pi E_{cap}/h\omega}}{\sqrt{E_R\ h\omega}} , \qquad (4\text{-}36)$$

where $h\omega$ is an average phonon energy and the parameter, A, is an adjustable parameter which can vary up to one order of magnitude from the value of Henry and Lang [116] of 1.5 x 10^{-14} cm^2-eV which will be assumed in the subsequent analysis. To evaluate the theoretical low temperature capture cross-section, the parameters E_{cap}, $h\omega$, and E_R must be known; these values are not known, however, for nonradiative hole capture by MPE. As can be seen from an analysis of eqn. (4-36), σ_{LT} depends only weakly on E_R. Additionally, the average phonon

energy, $h\omega$, should not depend strongly on the dopant. Thus, according to MPE theory, differences in σ_{LT} are most likely associated with small differences in E_{cap}. As an illustrative example, if we employ $h\omega/2\pi$ = 10 meV and E_R = 0.75 eV, as used by Lang [114] in his MPE analysis of the DX center in Te-doped AlGaAs, we find that $\sigma_{LT} = 4.2 \times 10^{-19}$ cm^2 when E_{cap} = 0.06 eV whereas $\sigma_{LT} = 2.3 \times 10^{-17}$ cm^2 when E_{cap} = 0.04 eV. Thus, a two order of magnitude change in σ_{LT} can be accounted for by a 20 meV change in E_{cap}. Therefore, we conclude that the differing experimental values of the low-temperature capture cross-sections for Te- and Si-doped samples are consistent with MPE theory. In particular, these differences are likely due to small differences in the capture barrier, E_{cap}.

4.2.2. The charge state of the DX center

The charge state of the DX center is the subject of some controversy at present. Accordingly, verification of the charge state of the electron-occupied DX level is required. Low-temperature hole capture cross-sections measured by the MCC technique for Te- and Si-doped samples are shown in Fig. 4.5 and are compared to intermediate-temperature hole capture cross-sections [76] measured by DLTS. For comparative purposes, trends in the capture rate as a function of temperature according to the MPE theory as proposed by Ridley

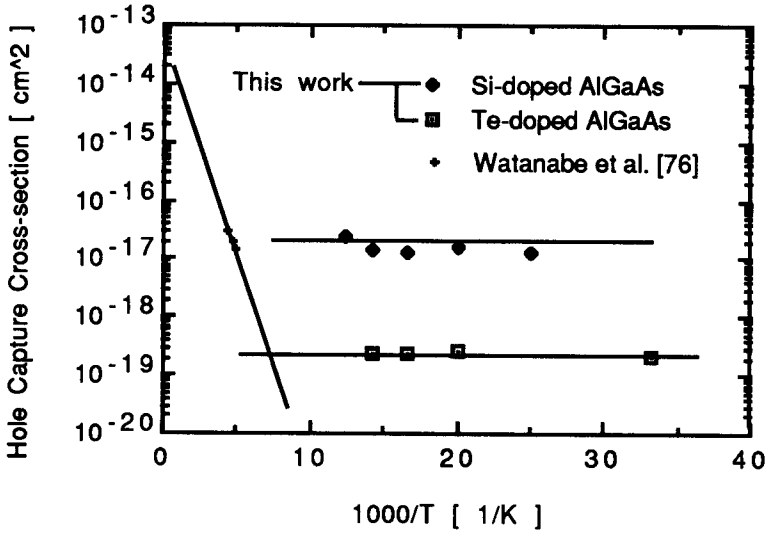

Figure 4.5. Low-temperature hole capture cross-sections obtained from MCC experiments for Te- and Si-doped samples. The data designated by +'s is from Watanabe [76], in which the DLTS technique was employed to measure the intermediate-temperature hole capture cross-section.

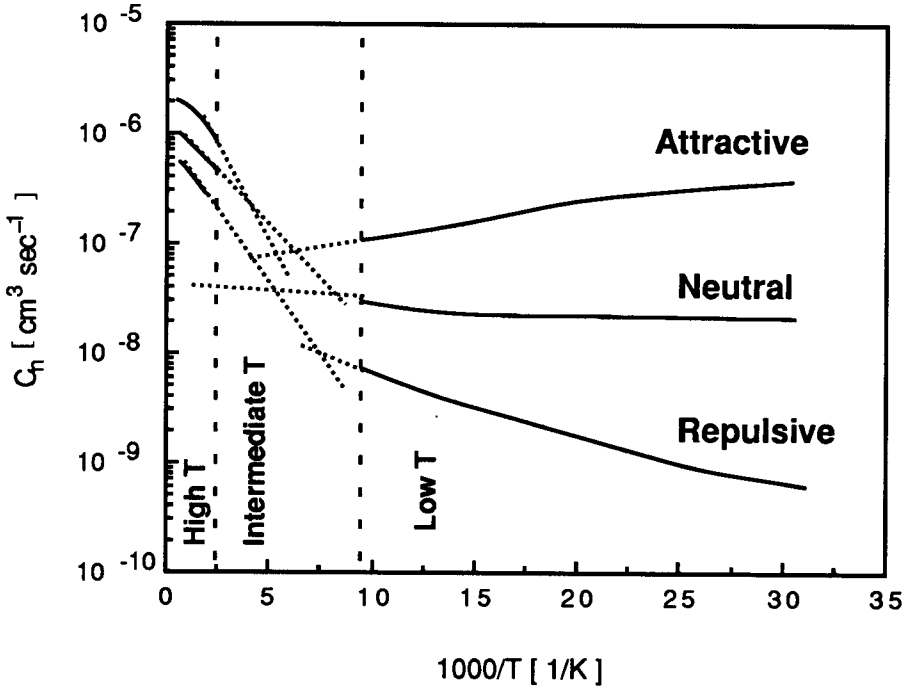

Figure 4.6. Capture rate as a function of the charge state of the deep level over a wide temperature range [117].

Table 4.4. A summary of experimentally determined low-temperature capture-cross section trends for GaAs and GaP

Semiconductor	Defect	Type of capture	Low temperature s (cm^2)	s - trend with decreasing temperature(a)	Nature of Coulombic interaction	References
GaAs	A	Hole	$> 5 \times 10^{-15}$	Increasing(220K)	Attractive	116, 119
GaAs	A	Electron	$\sim 5 \times 10^{-18}$	Constant	Unknown	116
GaAs	Cr	Electron	$< 10^{-19}$	Decreasing(250K)	Neutral	116, 119
GaAs	Fe	Electron	$< 10^{-19}$	Decreasing(250K)	Neutral	116, 119
GaAs	B	Electron	$\sim 10^{-21}$	Constant	Unknown	116
GaAs	B	Hole	$> 2 \times 10^{-15}$	Increasing(260K)	Attractive	116, 119
GaAs	E3	Electron	$< 5 \times 10^{-17}$	Decreasing(210K)	Unknown	116
GaAs	Cu	Hole	$> 2 \times 10^{-15}$	Increasing	Attractive	116, 119
GaAs	O, EL2	Electron	$< 5 \times 10^{-18}$	Decreasing(110K)	Neutral	116
GaP	O	Hole(σ_{p1})	4×10^{-21}	Constant	Neutral	116, 118
GaP	O	Hole(σ_{p2})	$> 10^{-14}$	Increasing(200K)	Attractive	116, 118
GaP	O	Electron(σ_{n2})	2×10^{-20}	Constant	Neutral	116, 118
GaP	ZnO	Electron	$< 10^{-15}$	Decreasing(180K)	Neutral(b)	116
GaP	0.95eV hole trap	Hole	$> 10^{-14}$	Increasing(80K)	Attractive	75
GaP	0.75eV hole trap	Hole	$> 10^{-12}$	Increasing(120K)	Attractive	75

Note:
(a): Increasing, decreasing, and constant refers to the trend in the experimental capture cross-section at the lowest measurement temperature. The lowest measurement temperature is indicated in parentheses for traps which do not show a constant capture cross-section.

(b): ZnO is a two-defect, isoelectronic trap in GaP. The Coulombic interaction during electron capture is more complicated than for a simple trap because of the dipole moment of the ZnO isoelectronic trap.

and Amato [117] are shown in Fig. 4.6. According to this theory, at low temperature the capture cross-section increases as temperature decreases for Coulombically attractive capture. In contrast, neutral capture is temperature-independent whereas repulsive capture yields a decreasing cross-section with decreasing temperature.

Additionally, Henry and Lang [116] and Hamilton *et al.* [75] show experimentally for fifteen defects in GaAs and GaP that the low temperature capture cross-section for Coulombically attractive centers is large (~ 10^{-13} - 10^{-16} cm^2) and increases with decreasing temperature while it is small (~ 10^{-18} - 10^{-21} cm^2) for neutral capture and is temperature-independent at low temperature as shown in Table 4.4.

In summary, MCC experiments indicate the low temperature minority capture cross-section to be approximately 2.0 x 10^{-19} and 1.5 x 10^{-17} cm^2 for Te- and Si-doped samples, respectively, and to be temperature-independent. The MPE theory of Ridley *et al.* [117] and the experimental trends of Henry and Lang [116] and of Hamilton et al. [75] indicate that because the MCC capture cross-sections are of the magnitude measured and temperature-independent, DX capture must involve a neutral charge state.

This conclusion, that DX hole capture involves a neutral charge state, appears to be in conflict with the DX model of Chadi and Chang [12]. According to the model of Chadi and Chang, the MCC process can be described by:

$$2\ h^+ + DX^- = d^+.$$

This is the reverse of the DX formation process which is described by:

$$d^+ + 2\ e^- = DX^-.$$

Thus, the MCC process would appear to involve Coulombically attractive capture in terms of the model of Chadi and Chang. However, the MCC experimental results can be reconciled with the model of Chadi and Chang if it is assumed that the MCC process can be described by a two-step process:

step 1: $h^+ + DX^- = DX^\circ$

step 2: $h^+ + DX^\circ = d^+$ (rate-limiting).

Step 2 is assumed to be the slower or rate-limiting process which dominates the overall MCC process.

In conclusion, the magnitude and temperature-dependence of the experimentally determined capture cross-sections indicate that the rate-limiting step for hole capture involves DX in a neutral charge state. This conclusion is motivated by MPE theory [114]. Thus, the results of the current investigation are comparable to the negative-U model [12] for DX if the rate-limiting step for hole capture is identified as due to capture into the neutral DX° state.

Chapter 5. Optically-Induced Dislocation-Glide and -Climb: Experimental Results and Discussion

In this chapter, optically-controlled dislocation-glide and-climb experiments are undertaken as a means of external gettering to reduce the DX concentration in AlGaAs device regions. The DX concentration, net ionized positive charge concentration, and free carrier compensation ratio are evaluated from C-V profiling, DLTS, TSCAP, and DLAS measurements. A comparison is made between samples which are subjected to optical processing and samples which are not subjected to any optical processing.

5.1 Optical power density threshold for dislocation glide

Initially, a laser power density of 1.5×10^5 W/cm^2 [87] was used for dislocation-glide. However, this power density caused irradiation damage to the sample surface. (It should be noted that the power density has to do with the size of the laser beam. The estimated power density depends upon how the beam size is measured.)

To find a power density which would not cause surface damage, the beam size was increased until surface damage to the sample was not observed. This readjusted optical power density was found to be 6.9×10^4 - 9.2×10^4 W/cm^2.

The CL image of a dislocation-glided sample is shown in Fig 5.1. The employed optical power density and beam size for the glided sample are 9.2 x 10^4 W/cm^2 and 45 μm, respectively, the scanning speed is 45 μm/sec, and the employed laser mode is TEM_{01} or TEM_{10}. As can be seen from the CL image, a misfit dislocation network is observed, which indicates the occurrence of dislocation-glide. Many dark dots are observed in the CL micrograph and are believed to be the ends of threading dislocations.

However, for samples listed in Table 5.2, a misfit dislocation network is not observed. The absence of dislocation-glide is attributed to the use of the laser which is in a very high order mode. The employed optical power density and beam size for glide of samples DL5HR and DL10HR are 8.7 x 10^4 W/cm^2 and 30 μm, respectively, and the scanning speed is 40 μm/sec.

5.2. A comparison of net charge concentrations deduced from various characterization methods before and after optical processing

A summary of the experimental results of the first and second dislocation-glide and -climb experiments for the samples listed in Tables 3.1 and 3.2 are shown in Tables 5.1 and 5.2. The principle difference between Table 5.1 (the first experimental results) and Table 5.2 (the second

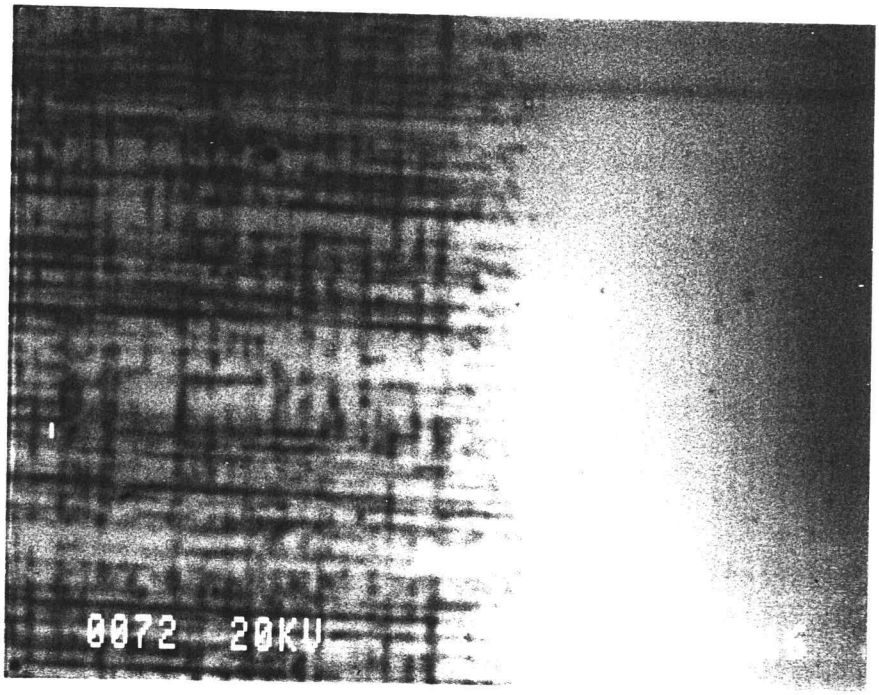

Figure 5.1. CL micrograph of glided sample. Misfit dislocation network formed after optical processing. The employed optical power density and beam size are 9.2×10^4 W/cm^2 and 45 μm, respectively, and the scanning speed is 45 μm/sec. The laser mode is either TEM_{01} or TEM_{10}.

experimental results) is in the nature of the laser mode. For the first experiment, either a TEM_{10} or a TEM_{01} mode is used, while a very higher order mode is used for the second experiment.

In Tables 5.1 and 5.2, the samples labeled ASIS, NO10AS, ODL56, and DL0HR are not subjected to any optical processing and are taken as references with respect to the subsequent samples with which they are grouped and which have undergone optical processing. N_{D1}^+ and N_{D2}^+ represent total ionized donor concentrations at 30 K and 300 K, respectively, and N_{A1}^- and N_{A2}^- indicate total negative charge concentrations (which may be attributed to the sum of ionized acceptors and negatively charged DX centers) at 30 K and 300 K, respectively. The DX concentration, N_{DX}, is assumed to be equal to the difference between the net ionized donor concentrations measured at 30 K and 300 K. The DX concentration is obtained by DLTS using the following formula [120],

$$N_{DX} = \frac{\delta C_{max}}{C_o} \frac{2N_D r^{r/(r-1)}}{(1-r)}$$

where $r=t_2/t_1$. C_o and δC_{max} are, respectively, the capacitance at t=0 and the capacitance difference between $C(t_2)$ and $C(t_1)$ (i.e., the rate window capacitance value) where the DLTS peak occurs. To obtain the DX concentration from TSCAP measurements, the following formula [9] is employed:

$$\frac{N_{DX}}{n} = \left(\frac{C_3}{C_2}\right)^2 - 1$$

where C_2 and C_3 indicate the 30 K capacitance of curve 2 and 3, respectively (refer to Fig. 3.19).

The free carrier compensation ratio, C%, is defined as the ratio of the net free carrier concentration (i.e., the

Table 5.1. Experimental results of the first optical dislocation-glide and -climb experiment.

Sample	Method	N_{DL} = $N_{D1}^+ - N_{A1}^-$ at 30 K [cm^{-3}]	N_{DH} = $N_{D2}^+ - N_{A2}^-$ at 300 K [cm^{-3}]	N_{DX} = $N_{DH} - N_{DL}$ [cm^{-3}]	C% (carrier compensation %) = $\frac{N_{DH} - N_{DL}}{N_{DH}}$
ASIS	DLTS	-	-	1.25×10^{17}	-
	TSCAP	-	-	1.92×10^{17}	-
	C-V	8.12×10^{16}	3.47×10^{17}	2.66×10^{17}	77%
NO16	DLTS	-	-	1.38×10^{17}	-
	TSCAP	-	-	2.42×10^{17}	-
	C-V	1.03×10^{17}	4.04×10^{17}	3.01×10^{17}	75%
NO3	DLTS	-	-	9.38×10^{16}	-
	TSCAP	-	-	1.88×10^{17}	-
	C-V	1.23×10^{17}	4.05×10^{17}	2.82×10^{17}	70%
NO17	DLTS	-	-	1.00×10^{17}	-
	TSCAP	-	-	2.07×10^{17}	-
	C-V	1.07×10^{17}	3.77×10^{17}	2.70×10^{17}	72%
OPTXE	DLTS	-	-	6.78×10^{17}	-
	TSCAP	-	-	1.13×10^{17}	-
	C-V	6.11×10^{16}	2.32×10^{17}	1.71×10^{17}	74%
NO10AS	DLTS	-	-	1.03×10^{17}	-
	C-V	8.84×10^{16}	3.90×10^{17}	3.02×10^{17}	77%
NO10	DLTS	-	-	7.24×10^{16}	-
	C-V	1.25×10^{17}	4.03×10^{17}	2.78×10^{17}	69%
ODL56	DLTS	-	-	1.10×10^{17}	-
	C-V	3.96×10^{16}	2.77×10^{17}	2.37×10^{17}	85%
ODL34	DLTS	-	-	1.12×10^{17}	-
	C-V	4.93×10^{16}	2.93×10^{17}	2.44×10^{17}	83%

difference in the total ionized donor concentration at 300 K and 30 K, $N_{DH}-N_{DL}$) to the room temperature carrier concentration. The reduction in the carrier concentration as temperature is decreased arises from compensation due to the DX center. Thus, the magnitude of the compensation ratio, C%, directly reflects the DX concentration and is the optimal indicator of the DX concentration because it is normalized in such a way that any inhomogenieties in the starting material are taken into account.

In the following sections, the experimental results summarized in Tables 5.1 and 5.2 are discussed in more detail.

Table 5.2. Experimental results of the second optical dislocation-glide and -climb experiment.

Sample	Method	N_{DL} = $N_{D1}^+ - N_{A1}^-$ at 30 K [cm^{-3}]	N_{DH} = $N_{D2}^+ - N_{A2}^-$ at 300 K [cm^{-3}]	N_{DX} = $N_{DH} - N_{DL}$ [cm^{-3}]	C% (carrier compensation %) = $\frac{N_{DH} - N_{DL}}{N_{DH}}$
DL0HR	DLTS	-	-	1.66×10^{17}	-
	TSCAP	-	-	2.09×10^{17}	-
	C-V	8.32×10^{16}	3.63×10^{17}	2.80×10^{17}	77%
DL5HR	DLTS	-	-	1.31×10^{17}	-
	TSCAP	-	-	1.67×10^{17}	-
	C-V	6.79×10^{16}	2.98×10^{17}	2.30×10^{17}	77%
DL10HR	DLTS	-	-	1.07×10^{17}	-
	TSCAP	-	-	1.72×10^{17}	-
	C-V	6.03×10^{16}	2.69×10^{17}	2.09×10^{17}	77%

5.2.1. DX concentration and compensation ratio for samples ASIS, NO16, NO3, and NO17

Samples NO16, NO3, and NO17 are subjected to both dislocation-glide and -climb. The net donor concentrations, N_{DL} and N_{DH}, obtained at 30 K and 300 K, respectively, from C-V profiling measurements increased with increasing dislocation-climb time as shown in both Table 5.1 and Fig. 5.2. However, note that this increase is not monotonic with dislocation-climb time since N_{DL} and N_{DH} for sample NO17 which is annealed for 20 hours are smaller than that of the sample NO3 which is annealed for 10 hours. Also, it should be pointed out that sample NO17 is subjected to optical dislocation-glide twice whereas the other samples are only optically glided once. Thus, these smaller values of N_{DL} and N_{DH} for sample NO17 are attributed to the fact that this sample underwent two optical glide scans.

As can be seen from Table 5.1, sample NO3 shows the lowest C%. Thus, sample NO3 which is subjected to optical-glide and -climb processing is compared to sample ASIS which is not subjected to any optical processing.

After optical processing, N_{DH} of sample NO3 increases by approximately 17% compared to that of sample ASIS while N_{DL} increases by approximately 51%. These increases in N_{DL} and N_{DL} arise from a reduction in DX compensation. That is, the DX concentration is reduced after optical processing.

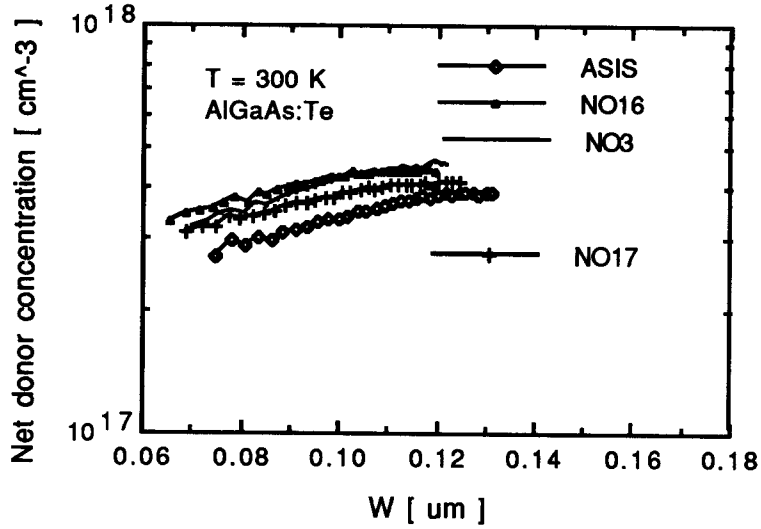

(a)

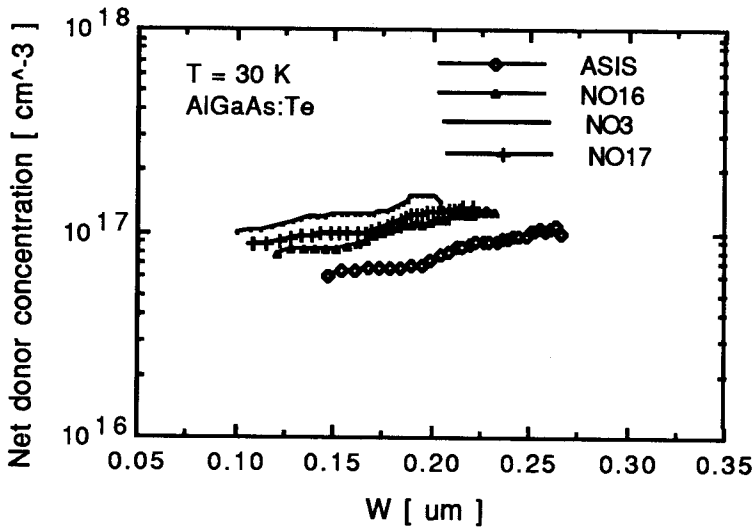

(b)

Figure 5.2. A comparison of C-V doping profiles at (a) 300 K; and (b) 30 K for the samples ASIS, NO16, NO3, NO17, and OPTXE. Sample ASIS is not subjected to any optical processing whereas samples NO16, NO3, and NO17 are subjected both optical-glide and climb.

This reduction in the DX concentration with optical processing is found from DLTS, TSCAP and DLAS analysis whereas C-V profiling measurement indicates the DX concentration to increase slightly with optical processing. The DX concentrations obtained from DLTS and TSCAP for sample NO3 are reduced by 25% and 2%, respectively, after dislocation-glide and -climb as indicated in Table 5.1. DLTS spectra for samples ASIS and NO3 are compared in Fig. 5.3 and clearly show a reduction in the DX concentration after optical annealing. As indicated in Table 5.1, this reduction in the DX concentration corresponds quantitatively, as estimated by DLTS, to a decrease in the DX concentration from 1.25×10^{17} cm^{-3} prior to optical processing to 9.38×10^{16} cm^{-3} after optical processing. Fig. 5.4 shows DLAS spectra in the temperature region between 140 K and 300 K at 500 kHz for samples ASIS and NO17. Qualitatively it is clear from Fig. 5.4 that the DX concentration is reduced after optical processing. A quantitative comparison of the DX concentrations before and after optical processing is not possible from DLAS measurements. Note also from Fig. 5.4, that the conductance curve which peaks at about 250 K decreases slightly after optical processing. In addition, the compensation ratio, C%, for sample NO3 as indicated in Table 5.1 is approximately 7% smaller than that of sample ASIS. This smaller C% indicates a reduction in DX concentration.

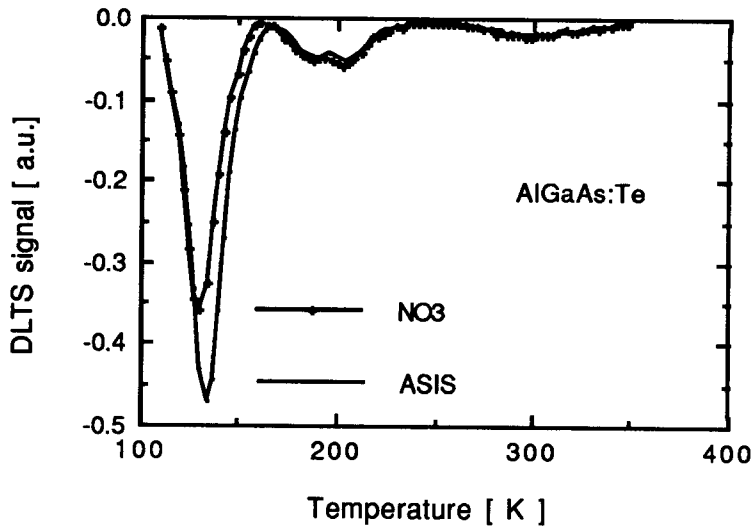

Figure 5.3. DLTS spectra for samples ASIS and NO3. Sample ASIS is not subjected to any optical processing whereas sample NO3 is subjected to optical-glide and -climb.

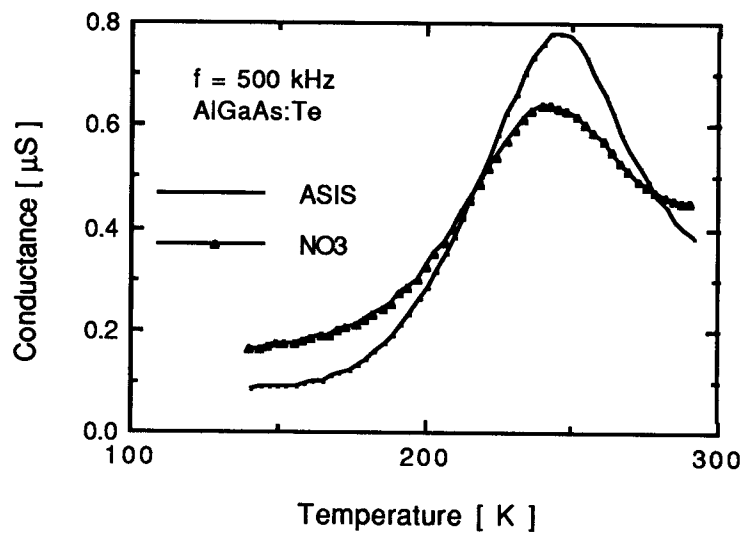

Figure 5.4. DLAS spectra measured at 500 kHz for samples ASIS and NO3. Sample ASIS is not subjected to any optical processing whereas sample NO3 is subjected to optical-glide and -climb.

However, the DX concentration of sample NO3 deduced from C-V measurement is increased by 6% after optical processing. It is believed that this apparent increase in the DX concentration as deduced by C-V profiling arises from the nonlinearity of the $1/C^2$ - V plot. Note that DLTS, DLAS, TSCAP, and C% analysis indicate a reduction in the DX concentration.

In conclusion, DLTS, TSCAP, DLAS, and C% analysis indicate a 2% - 25% reduction in the DX concentration after both dislocation-glide and -climb processes whereas only C-V analysis shows a 6% growth in the DX concentration. It should be noted that while the samples used in this experiment were all obtained from the same wafer, they were not taken from the same portion of the wafer. As shown in the next section, better agreement between carrier concentrations assessed from different experimental techniques is obtained when care is taken to compare samples which are in close physical proximity. This implies that concentration inhomogenieties can obscure an accurate comparison between optically processed and unprocessed samples.

5.2.2. DX concentration and compensation ratio for samples NO10AS and NO10

Sample NO10 is subjected to dislocation-glide only while sample NO10AS is a reference sample which undergoes no

optical processing. NO10 and NO10AS are samples which are in close physical proximity (i.e., two Schottky diodes are fabricated on one 2 x 1.5 mm size chip while each Schottky diode is fabricated on a different chip for the other samples. In the case where the material is not homogeneous, the samples should be close to each other for comparative purpose.)

DX concentrations obtained from DLTS and C-V measurements are reduced by 30% and 8%, respectively, after dislocation-glide processing (Table 5.1). DLTS spectra and the C-V doping profile for samples NO10AS and NO10 are shown in Figs. 5.5 and 5.6, respectively. N_{DH} and N_{DL} deduced by C-V

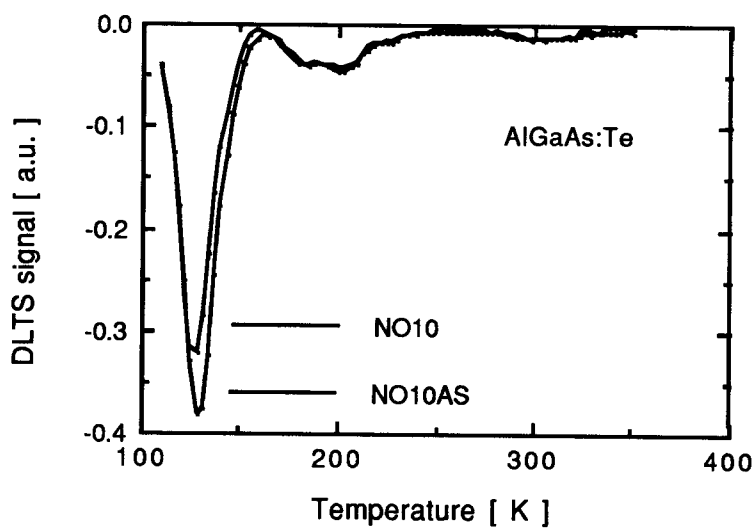

Figure 5.5. DLTS spectra of samples NO10AS and NO10. Sample NO10AS is subjected to no optical processing whereas sample NO10 is subjected to dislocation-glide processing.

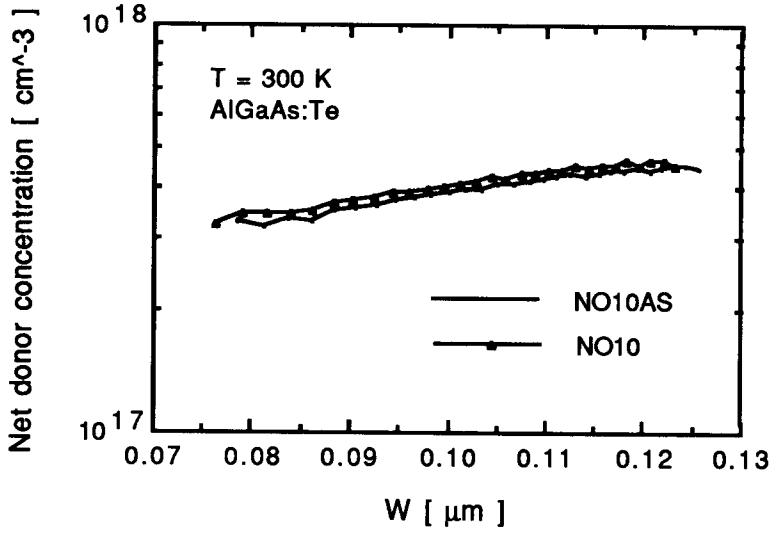

(a)

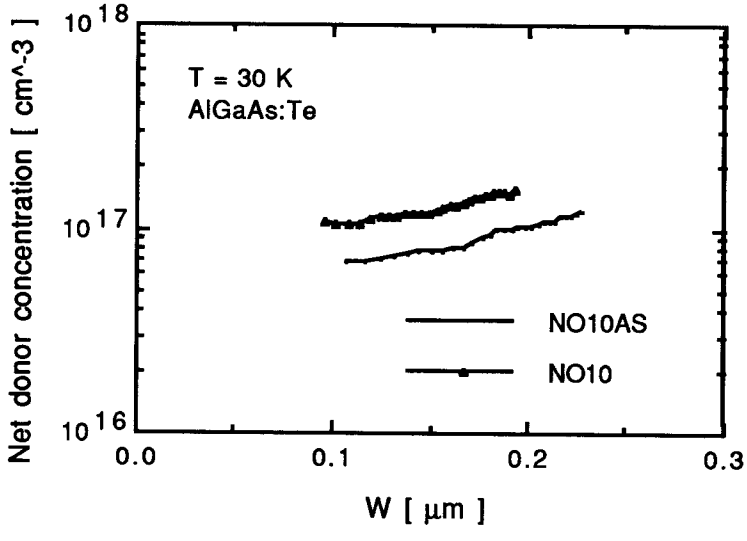

(b)

Figure 5.6. Doping profile of samples NO10AS and NO10 measured at (a) 300 K; and at (b) 30 K. Sample NO10AS is not subjected to any optical processing whereas sample NO10 is subjected to optical dislocation-glide processing.

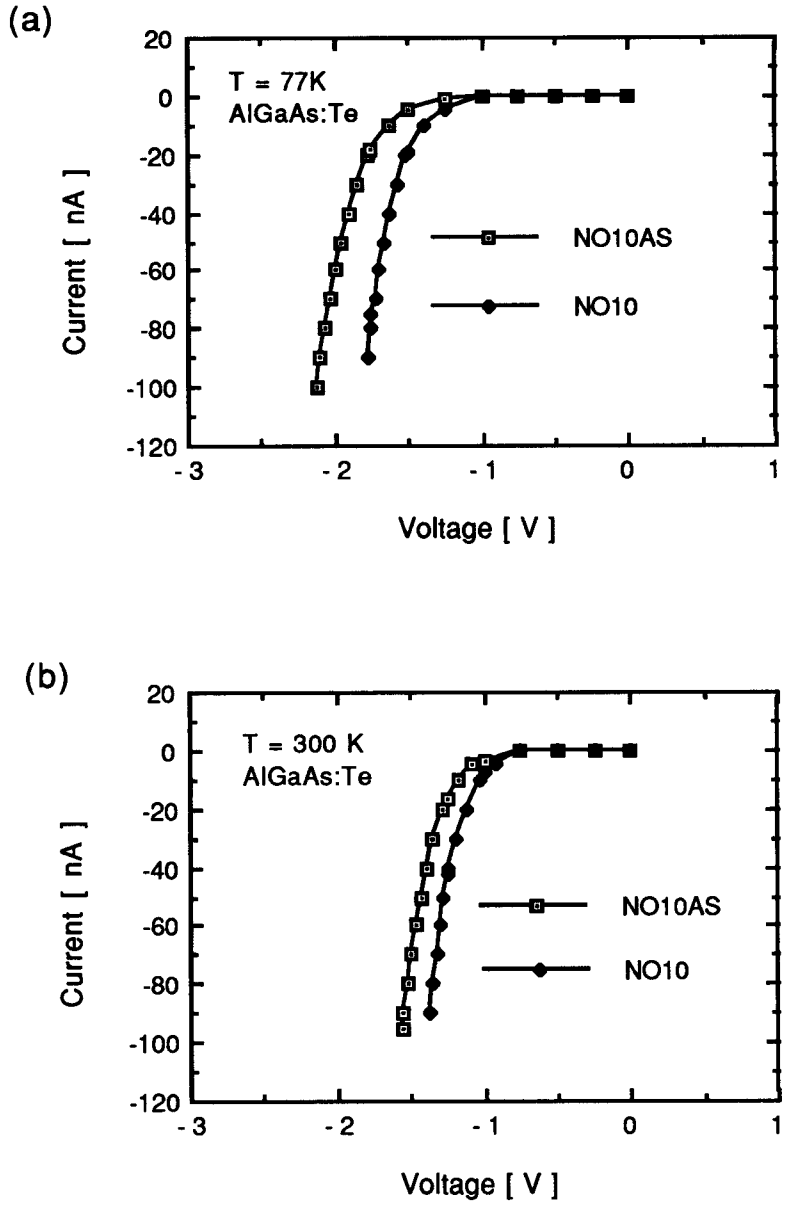

Figure 5.7. I-V characteristics of the samples NO10AS and NO10 at (a) 77 K; and (b) 300 K. Sample NO10AS is not subjected to any optical processing whereas sample NO10 is subjected to optical dislocation-glide processing.

profiling increase by 3% and 41%, respectively, after dislocation-glide due to less compensation and, hence, a reduction in the DX concentration. C% also decreases by 8% after optical dislocation-glide, which also indicates a reduction in the DX concentration.

I-V analysis of sample NO10 indicates a lower breakdown voltage (BV) than that of sample NO10AS as shown in Fig. 5.7. This lower BV is consistent with the observed increase in N_{DH} and N_{DL} after optical dislocation-glide processing which lowers BV [121].

In conclusion, DLTS, DLAS, C-V, and C% analysis indicate a reduction in the DX concentration of approximately 8% - 30% after dislocation-glide processing. However, it should be noted that dislocation-glide is a conservative motion. Thus, defects cannot be removed by dislocation-glide itself. Therefore, it is concluded that some dislocation-climb occurs concomitant with the dislocation-glide process.

5.2.3. DX concentration and compensation ratio for samples ODL56 and ODL34

Sample ODL34 is subjected to dislocation-climb only whereas sample ODL56 is a reference sample which underwent no optical processing. Note that the Schottky dot areas of samples ODL34 and ODL56 are approximately 3 times larger than

that of the other samples. As shown in Table 5.1, the DX concentrations obtained from DLTS and C-V analysis are increased by 1.8% and 3%, respectively, and N_{DH} and N_{DL} are increased by 6% and 24%, respectively, after dislocation-climb processing. These results indicate that there is less compensation by the DX center after optical dislocation-climb only. Also C% is reduced by 2% after dislocation-climb processing, which indicates less DX compensation. However, the magnitude of the reduction in the DX concentration for this sample, which is subjected to dislocation-climb processing only, is not as large as that of samples which are subjected to dislocation-glide processing only or to both dislocation-glide and -climb.

In conclusion, the DX concentration is relatively uneffected by dislocation-climb processing only.

5.2.4. DX concentration for sample OPTXE

Sample OPTXE is subjected to both dislocation-glide and -climb. A Kr-ion laser is used for dislocation-glide while a Xe lamp is used for dislocation-climb. The climb time is 97 days. After optical processing, N_{DH} and N_{DL} are reduced by 33% and 25%, respectively, compared to sample ASIS. This reduction in N_{DH} and N_{DL} indicates an enhancement of DX compensation. These results are in complete opposition to previous results. Therefore, further analysis of this sample

was not performed since it is the purpose of this work to investigate optical treatments which yield a decrease in the DX concentration. Although the reason for the observed reduction in N_{DH} and N_{DL} after dislocation-climb processing with the Xe lamp is not clear, this result suggests that the optical intensity during dislocation-climb may be an important factor in establishing the effectiveness of the climb process.

5.2.5. DX concentration and compensation ratio for samples DL0HR, DL5HR, and DL10HR

Samples DL5HR and DL10HR listed in Table 5.2, are subjected to both dislocation-glide and -climb. It should be noted that no misfit dislocation network is observed for these samples, which is an indication that no dislocation-glide occurred. This absence of dislocation-glide is attributed to the use of laser with a very high order mode, whereas either a TEM_{10} or a TEM_{01} mode is used for the samples listed in Table 5.1. As shown in Table 5.2, N_{DH} and N_{DL} deduced from C-V profiling decrease with increasing climb time. Therefore, further analysis of these samples was not performed for the same reason as that of sample OPTXE. However, it should be noted that C% is not changed for sample DL5HR or DL10HR compared to reference the sample DL0HR as indicated in Table 5.2.

In conclusion, the DX concentration for samples in which no dislocation-glide occurred is not changed and the absence of dislocation-glide is attributed to the use of a laser with a very high order mode.

5.3. Summary of optical dislocation-glide and -climb

In summary, the DX concentration is shown to be reduced by 2%-30% for samples subjected to optical dislocation-glide and -climb processing. The DX concentration is mainly established by the glide process but the samples subjected to dislocation-climb only are relatively uneffected. It should be noted that dislocation-glide and -climb depend strongly on the mode structure of the laser employed.

Note that a comparison of samples which have and have not undergone optical processing is best achieved if the samples are in close physical proximity because of inhomogenieties across the wafer in the starting material. Because of these inhomogenieties, the compensation ratio, C%, is the best indicator for the evaluation of DX concentration changes before and after optical processing since it is a normalized parameter which minimizes problems with uncertainties associated with inhomogenieties of the starting material.

Chapter 6. Conclusions and Recommendations for Future Work

In this thesis, two experimental approaches are employed in order to explore aspects of the nature of the DX center in AlGaAs. The minority carrier capture (MCC) technique is used to investigate the nature of the DX center in Te- and Si-doped $Al_{0.3}Ga_{0.7}As$. Additionally, optically-controlled dislocation-glide and -climb is utilized as a technique for external gettering to reduce the DX concentration in $Al_{0.3}Ga_{0.7}As$:Te device regions.

The major accomplishments of the MCC portion of this experimental investigation are:

1. The measured hole capture cross-sections for Te- and Si-doped $Al_{0.3}Ga_{0.7}As$ are approximately 2×10^{-19} and 1.5×10^{-17} cm^2, respectively, and are independent of temperature below ~ 70 K.

2. The differing experimental values of the low-temperature capture cross-sections for Te- and Si-doped samples are consistent with multiphonon emission (MPE) theory. In particular, these differences are likely due to small differences in the capture barrier, E_{cap}.

3. The magnitude and temperature-dependence of the experimentally determined capture cross-sections indicate that the rate-limiting step for hole capture involves DX in a neutral charge state. This conclusion is motivated by MPE theory [114]. Thus, the results of the current investigation are comparable to the negative-U model of Chadi and Chang [12] for DX if the rate-limiting step for

hole capture is identified as due to capture into the neutral DX^{o} state.

The primary results of the experimental investigation of optically-controlled dislocation-glide and -climb are:

1. The DX concentration as measured by C-V profiling, DLTS, TSCAP, and DLAS analysis is shown to be reduced by 2%-30% after optical processing.

2. The net donor concentration measured at 30 K and 300 K increases after optical processing. This increase in the net donor concentration is consistent with a decrease in the DX concentration because of compensation by the DX center.

3. Experimental results 1 and 2 support the DX model originally proposed by Lang *et al.*[9,10] and extended by Van Vechten [59,60]. According to this model, the DX center is a defect complex consisting of a donor and an arsenic vacancy. In terms of this model, increases in the net donor concentration arise from the removal of the compensating arsenic vacancy.

4. The DX concentration decreases markedly after optical dislocation-glide processing only. The dislocation-climb process appears to be less important for reduction of the DX concentration than the dislocation-glide process.

Although the DX concentration is reduced after optical processing, there are several tasks to consider for investigating the DX center in AlGaAs.

1. The use of different optical sources:

- Utilization of a pulsed laser instead of a CW laser. By using a pulsed laser, the high optical power density (on the order of a mega-watt) is easily obtained and surface damage due to continuous radiation may be avoided.

2. Use of low-doped samples:

   - The depletion layer of a highly doped sample is too small to investigate the interior of the epilayer. Therefore, a low doped sample can be used to investigate deeper into the epilayer. Additionally, optically-induced changes will, perhaps, constitute a larger fraction of the DX concentration so that optically-induced changes can be deduced in a more precise manner.

3. Fabrication of a HEMT device using samples which are subjected to dislocation-glide and -climb:

   - Fabrication of an active device, such as a HEMT, and operation at low temperature after dislocation-glide and -climb should yield improved device performance and demonstrate the utility of optically-induced processing for external gettering.

4. Transient decay of persistent photoconductivity (TDPPC) measurements:

   - TDPPC [50] is an alternative technique for assessing the presence of the DX center in AlGaAs. The advantage of this technique is that ohmic contacts are placed on the sample on the edges of an active area of the AlGaAs such that electrical analysis of the same area of the sample may accomplished before and after optical processing.

BIBLIOGRAPHY

[1] H. Kunzel, A. Fischer, J. Knecht, and K. Ploog," Investigation of Persistent Photoconductivity in Si-doped n-$Al_xGa_{1-x}As$ Grown by Molecular Beam Epitaxi," Appl. Phys. A., Vol. 32, p 69-78, 1983.

[2] R. J. Nelson," Long-Lifetime Photoconductivity Effect in n-type GaAlAs," Appl. Phys. Lett., Vol. 31, No. 5, p 351-353, 1977.

[3] H. P. Hjalmarson and T. J. Drummond," Deep donor Model for the Persistent Photoconductivity Effect," Appl. Phys. Lett., Vol. 48, No. 10, p 656-658, 1986.

[4] T. N. Theis and S. L. Wright," Origin of "residual" Persistent Photoconductivity in Selectively Doped GaAs/$Al_xGa_{1-x}As$ Heterojunctions," Appl. Phys. Lett., Vol. 48, No. 20, p 1374-1376, 1986.

[5] N. Chand, R. Fischer, J. Klem, T. Henderson, P. Pearah, W. T. Masselink, Y. C. Chang, and H. Morkoc," Beryllium and Silicon Doping Studies in $Al_xGa_{1-x}As$ and New Results on Persistent Photoconductivity," J. Vac. Sci. Technol. B. Vol. 3, No. 2, p 644-648, 1985.

[6] V. Narayanamurti, R. A. Logan, and M. A. Chin," Symmetry of Donor-Related Centers Responsible for Persistent Photoconductivity in $Al_xGa_{1-x}As$," Phys. Rev. Lett., Vol. 43, No. 20, p 1536-1539, 1979.

[7] A. G. Milnes," Semiconductor Heterojunction Topics: Introduction and Overview," Solid-State Electron., Vol. 29, No. 2, p 99-121, 1986.

[8] W. Timelthaler, W. Jantsch, and G. Weimann," Persistent 2D Photoconductivity and Deep Levels in $Al_xGa_{1-x}As$/GaAs Heterostructures," Semicond. Sci. Technol., Vol. 5, p 686-690, 1990.

[9] D. V. Lang, R. A. Logan, and M. Jaros," Trapping Characteristics and a Donor-Complex (DX) Model for the Persistent-Photoconductivity Trapping Center in Te-doped $Al_xGa_{1-x}As$," Phys. Rev. B., Vol. 19, No. 2, p 1015-1030, 1979.

[10] D. V. Lang and R. A. Logan," Large-Lattice-Relaxation Model for Persistent Photoconductivity in Compound

Semiconductors," Phys. Rev. Lett., Vol. 39, No. 10, p 635-639, 1977.

[11] D. J. Chadi and K. J. Chang," Theory of the Atomic and Electronic Structure of DX Centers in GaAs and $Al_xGa_{1-x}As$ Alloys," Phys. Rev. Lett., Vol. 61, No. 7, p 873-876, 1988.

[12] D. J. Chadi and K. J. Chang," Energetic of DX-Center Formation in GaAs and $Al_xGa_{1-x}As$ Alloys," Phys. Rev. B., Vol. 39, No. 14, p 10063-10074, 1989.

[13] K. M. Yu, K. Khachaturyan, E. R. Weber, H. P. Lee, and E. G. Colas," Substitutionality of Te- and Sn-related DX Centers in $Al_xGa_{1-x}As$," Phys. Rev. B., Vol. 43, No. 3, p 2462-2465, 1991.

[14] T. J. Drummond, R. J. Fischer, W. F. Kopp, H. Morkoc, K. Lee, and M. S. Shur," Bias Dependence and Light Sensitivity of (Al, Ga)As/GaAs MODFET's at 77 K," IEEE Trans. Electron Devices, Vol. ED-30, No. 12, p 1806-1811, 1983.

[15] R. J. Fischer, T. J. Drummond, J. Klem, W. Kopp, T. S. Henderson, D. Perrachione, and H. Morkoc," On the Collapse of Drain I-V Characteristics in Modulation-Doped FET's at Cryogenic Temperatures," IEEE Trans. Electron Devices, Vol. ED-31, No. 8, p 1028-1032, 1983.

[16] H. Wolf, L. Bliek, G. Weimann, and W. Schlapp," Low-Frequency Excess Noise in Large GaAs Heterostructures-Temperature and Frequency Dependence," Semicond. Sci. Technol., Vol. 3, p 1184-1192, 1988.

[17] V. K. Raman, J. Chang, and C. R. Viswanathan," Electrical Properties of GaAs/InGaAS High Electron Mobility Transistors," Int. J. Electronics, Vol. 69, No. 5, p 621-629, 1990.

[18] M. B. Das and P. K. Ghosh," Low-Frequency Emissions from Deep Levels in GaAs MESFETs," Electronic Letters, Vol. 10, No. 5, p 207-208, 1982.

[19] R. Fischer, T. J. Drummond, W. Kopp, H. Morkoc, K. Lee, and M. S. Shur," Instabilities in Modulation Doped Field-Effect Transistors (MODFETs) at 77 K," Electronic Letters, Vol. 19, No. 19, p 789-791, 1983.

[20] A. Thomasian, N. L. Saunders, L. G. Hipwood, and A. A. Rezazadeh," Mechanism of Kink Effect Related to Negative Photoconductivity in AlGaAs/GaAs HEMTs," Electronic Letters, Vol. 25, No. 11, p 738-739, 1989.

[21] B. Monemar and G. R. Woolhouse," Observation and Analysis of very Rapid optical Degradation of GaAs/AlGaAs DH Laser Material," Appl. Phys. Lett., Vol. 29, No. 9, p 605-607, 1976.

[22] E. F. Schubert, J. Knecht, and K. Ploog," Transient and Persistent Photoconductivity in n-$Al_xGa_{1-x}As$ and Selectively Doped n-$Al_xGa_{1-x}As$/GaAs Heterostructures," J. Phys. C, Vol. 18, p L215-L221, 1985.

[23] T. Ando," Self-Consistent Results for a GaAs/$Al_xGa_{1-x}As$ Heterojunction. I. Subband Structure and Light-Scattering Spectra," J. Phys. Soc. Japan, Vol. 51, No. 12, p 3893-3899, 1982.

[24] T. N. Theis," DX centers in GaAs and $Al_xGa_{1-x}As$: Device Instabilities and Defect Physics," Inst. Phys. Conf. Ser. No. 91, p 1-6, 1987.

[25] T. N. Theis and B. D. Parker," Charge Trapping in n-$Al_xGa_{1-x}As$ " Insulators " and Related Device Instabilities," Appl. Surface Science, Vol. 30, p 52-63, 1987.

[26] K. R. Hofmann and E. Kohn," Deep Donor Trapping Effects on the Pulsed Characteristics of AlGaAs/GaAs HEMTs," Electronic Letters, Vol. 22, No. 6, p 335-337, 1986.

[27] M. Nathan, P. M. Mooney, P. M. Solomon, and S. L. Wright," Room-Temperature Electron Trapping in $Al_{0.35}Ga_{0.65}As$/GaAs Modulation-Doped Field-Effect Transistors," Appl. Phys. Lett., Vol. 47, No. 6, p 628-630, 1985.

[28] D. V. Lang in *Deep Centers in Semiconductors*, edited by S. T. Pantelides, (Gordon and Breach Science, New york, 1986) p 489-539.

[29] P. M. Mooney," Deep Donor Levels (DX Centers) in III-V Semiconductors," J. Appl. Phys., Vol. 67, No. 3, p R1-R26, 1990.

[30] P. Bhattacharya," The Relationship of the DX Center in $Al_xGa_{1-x}As$ and other III-V Alloys with the Conduction Band Structure," Semicond. Sci. Technol., Vol. 3, p 1145-1156, 1988.

[31] *Physics of DX Centers in GaAs Alloys*, edited by J. C. Bourgoin, Solid State Phenomena, Vol. 10, 1990.

[32] A. J. Springthorpe, F. D. King, and A. Becke," Te and Ge-Doping Studies in $Ga_{1-x}Al_xAs$", J. Electronic Mat., Vol. 4, p 101-118, 1975.

[33] M. G. Craford, G. E. Stillman, J. A. Rossi, and N. Holonyak, Jr," Effect of Te and S Donor Levels on the Properties of $GaAs_{1-x}P_x$ near the Direct-Indirect Transition," Phys. Rev., Vol. 168, No. 3, p 867-882, 1968.

[34] P. M. Mooney, N. S. Caswell, and S. L. Wright," The Capture Barrier of the DX center in Si-doped $Al_xGa_{1-x}As$," J. Appl. Phys., Vol. 62, No. 12, p 4786-4797, 1987.

[35] M. Tachikawa, M. Mizuta, and H. Kukimoto," DX Deep Centers in $Al_xGa_{1-x}As$ Grown by Liquid-Phase Epitaxi," Jpn. J. Appl. Phys., Vol. 23, No. 12, p 1594-1597, 1984.

[36] P. M. Mooney, E. Calleja, S. L. Wright, and M. Heiblum," Effect of the Host Band Structure on Capture and Emission Processes at DX Centers in AlGaAs," Materials Science Forum, Vol. 10-12, p 417-422, 1986.

[37] E. Calleja, A. Gomez, and E. Munoz," Direct Evidence of the DX Center Link to the L-conduction-band Minimum in GaAlAs," Appl. Phys. Lett., Vol. 52, No. 5, p 383-385, 1988.

[38] N. Chand, T. Henderson, J. Klem, W.T. Masselink, and R. Fischer," Comprehensive Analysis of Si-doped $Al_xGa_{1-x}As$(x=0 to 1): Theory and Experiments," Phys. Rev. B., Vol. 30, No. 8, p 4481-4492, 1984.

[39] E. F. Schubert and K. Ploog," Shallow and Deep Donors in Direct-Gap n-type $Al_xGa_{1-x}As$:Si Grown by Molecular-Beam Epitaxy," Phys. Rev. B., Vol. 30, No. 12, p 7021-7029, 1984.

[40] T. Ishibashi, S. Tarucha, and H. Okamoto," Si and Sn Doping in $Al_xGa_{1-x}As$ Grown by MBE," Jpn. J. Appl. Phys., Vol. 21, No. 8, p L476-L478, 1982.

[41] T. Ishikawa, J. Saito, S. Sasa, and S. Hiyamizu," Electrical Properties of Si-doped $Al_xGa_{1-x}As$ Layers Grown by MBE," Jpn. J. Appl. Phys., Vol. 21, No. 11, p L675-L676, 1982.

[42] M. O. Watanabe, and H. Maeda," Electron Activation Energy in Si-doped AlGaAs Grown by MBE," Jpn. J. Appl. Phys., Vol. 23, No. 9, p L734-L736, 1984.

[43] H. P. Hjalmarson and T. J. Drummond," Long Lived Resonance States in Si-Doped AlGaAs," Materials Science Forum, Vol. 38-41, p 1091-1096, 1989.

[44] D. K. Maude, J. C. Portal, L. Dmowski, T. Foster, L. Eaves, M. Nathan, M. Heiblum, J. J. Harris, and R. B. Beall," Investigation of the DX Center in Heavily Doped n-type GaAs," Phys. Rev. Lett., Vol. 59, No. 7, p 815-818, 1987.

[45] M. A. Fisher, A. R. Adams, E. P. O'Reilly, and J. J. Harris," Resonant Electron Scattering due to the Central Cells of Impurities Observed in AlGaAs under Hydrostatic Pressure," Phys. Rev. Lett., Vol. 59, no. 20, p 2341-2344, 1987.

[46] T. N. Theis, P. M. Mooney, and S. L. Wright," Electron Localization by a Metastable Donor Level in n-GaAs: A New Mechanism Limiting the Free-Carrier Density," Phys. Rev. Lett., Vol. 60, No. 4, p 361-364, 1988.

[47] M. Tachikawa, T. Fujisawa, H. Kukimoto, A. Shibata, G. Oomi, and S. Minomura," Observation of the Persistent Photoconductivity Due to the DX Center in GaAs under Hydrostatic Pressure," Jpn. J. Appl. Phys., Vol. 24, No. 11, p L893-L894, 1985.

[48] A. K. Saxena," The Conduction Band Structure and Deep Levels in $Ga_{1-x}Al_xAs$ Alloys from a High-pressure Experiment," J. Phys. C, Vol. 13, p 4323-4334, 1980.

[49] M. Mizuta, M. Tachikawa, H. Kukimoto, and S. Minomura," Direct Evidence for the DX Center Being a Substitutional Donor in AlGaAs Alloy System," Jpn. J. Appl. Phys., Vol. 24, No. 2, p L143-L146, 1985.

[50] T. W. Dobson, L. V. A. Scalvi, and J. F. Wager," Transient Decay of Persistent Photoconductivity in $Al_xGa_{1-x}As$," J. Appl. Phys., Vol. 68, No. 2, p 601-605, 1990.

[51] D. V. Lang and R. A. Logan," Chemical Shifts of DX Centers in $Al_xGa_{1-x}As$," Inst. Phys. Conf. Ser. No. 43, p 433-436, 1979.

[52] N. Lifshitz, A. Jayaraman, R. A. Logan, and H. C. Card," Pressure and Compositional Dependences of the Hall Coefficient in $Al_xGa_{1-x}As$ and Their Significance," Phys. Rev. B., Vol. 21, No. 2, p 670-678, 1980.

[53] J. F. Rochette, P. Delescluse, M. Laviron, D. Delagebeaudeuf, J. Chevrier, and N. T. Linh," Low Temperature Persistent Photoconductivity in Two-

dimensional Electron Gas FETs," Inst. Phys. Conf. Ser. No. 65, p 385-392, 1982.

[54] M. I. Nathan," Persistent Photoconductivity in AlGaAs/GaAs Modulation Doped Layers and Field Effect Transistors: A Review," Solid-State Electron., Vol. 29, No. 2, p 167-172, 1986.

[55] C. Canali, C. Tedesco, E. Zanoni, F. Magistrali, and M. Sangalli," Electron Detrapping Enhanced by Electric Field in AlGaAs/GaAs HEMTs," Electronic Letters, Vol. 26, No. 5, p 313-315, 1990.

[56] T. N. Theis, B. D. Parker, P. M. Solomon, and S. L. Wright," Hot-electron Capture to DX Centers in $Al_xGa_{1-x}As$ at Low Al Mole Fractions ($x<0.2$)," Appl. Phys. Lett., Vol. 49, No. 22, p 1542-1544, 1986.

[57] M. O. Watanabe, K. Morizuka, M Mashita, Y. Ashizawa, and Y. Zohta," Donor Levels in Si-doped AlGaAs Grown by MBE," Jpn. J. Appl. Phys., Vol. 23, No. 2, p L103-L105, 1984.

[58] T. N. Theis, T. F. Kuech, L. F. Palmateer, and P. M. Mooney," Far-infrared Spectroscopy of Silicon Donors in $Al_xGa_{1-x}As$," Inst. Phys. Conf. Ser. No. 74, p 241-246, 1984.

[59] J. A. Van Vechten," Thermodynamics of Deep Levels in Semiconductors," Mat. Res. Soc. Symp. Proc., Vol. 46, p 83-103, 1985.

[60] J. A. Van Vechten," Mossbauer Spectra and the DX-Center Complex in AlGaAs," J. Phys. :Condens. Matter, Vol. 1, p 5171-5177, 1989.

[61] P. M. Mooney, R. Fischer, and H. Morkoc," Transient Capacitance Study of Electron Traps in AlGaAs Grown with As_2," J. Appl. Phys., Vol. 57, No. 6, p 1928-1931, 1985.

[62] P. M. Mooney, W. Wilkening, U. Kaufmann, and T. F. Kuech," Electron-Paramagnetic-Resonance Measurements of Si-Donor-Related Levels in $Al_xGa_{1-x}As$," Phys. Rev. B., Vol. 39, No. 8, p 5554-5557, 1989.

[63] P. M. Mooney, G.A. Northrop, T. N. Morgan, and H. G. Grimmeiss," Evidence for Large Lattice Relaxation at the DX Center in Si-doped $Al_xGa_{1-x}As$," Phys. Rev. B., Vol. 37, No. 14, p 8298-8307, 1988.

[64] J. C. M. Henning and J. P. M. Ansems," A New Model of Deep Donor Centers in $Al_xGa_{1-x}As$," Materials Science Forum, Vol. 10-12, p 429-434, 1986.

[65] J. C. M. Henning and J. P. M. Ansems," A New Model of Deep Donor Centers in $Al_xGa_{1-x}As$," Semicond. Sci. Technol., Vol. 2, p 1-13, 1987.

[66] P. Basmaji, A. Zaouk, P. Gibart, D. Gauthier, and J. C. Portal," Enhancement of Free-Carrier Concentration in n-type $Al_xGa_{1-x}As$ grown by Metalorganic Vapor Phase Epitaxi in the Temperature Range 850-950°C," Appl. Phys. Lett., Vol. 54, No. 12, 1989.

[67] A. Oshiyama and S. Ohnishi," DX Center: Crossover of Deep and Shallow States in Si-doped $Al_xGa_{1-x}As$," Phys. Rev. B., Vol. 33, No. 6, p 4320-4323, 1986.

[68] T. N. Morgan," Theory of the DX Center in $Al_xGa_{1-x}As$ and GaAs Crystal," Phys. Rev. B., Vol. 34, No. 4, p 2664-2669, 1986.

[69] K. L. I. Kobayashi, Y. Uchida, and H. Nakashima," A Model for DX Centers: Bond Reconstruction due to Local Random Donor-Host Atom Configurations in Mixed Semiconductor Alloys," Jpn. J. Appl. Phys., Vol. 24, No. 12, p L928-L931, 1985.

[70] A. K. Saxena," Photoconductivity Storage in $Ga_{1-x}Al_xAs$ Alloys at Low Temperatures," Solid State Electron., Vol. 25, No. 2, p 127-131, 1982.

[71] M. F. Li, Y. B. Jia, P. Y. Yu, J. Zhou, and J. L. Gao," Negative-U Property of the DX Center in $Al_xGa_{1-x}As$:Si," Phys. Rev. B., Vol. 40, No. 2, p 1430-1433, 1989.

[72] T. Fujisawa, J. Yoshino, and H. Kukimoto," Direct Evidence for the Negative-U Property of the DX Center as Studied by Hydrostatic Pressure Experiments on GaAs Simultaneously Doped with Ge and Si," Jpn. J. Appl. Phys. Vol. 29, No. 3, p L388-L390, 1990.

[73] B. Hamilton," The Detection of Minority carrier Traps by Optically Induced Charge Exchange in n-type GaP Schottky Barriers," Inst. Phys. Conf. Ser. No. 22, p 218-225, 1974.

[74] A. R. Peaker, B. Hamilton, D. R. Wight, I. D. Blenkinsop, W. Harding, and R. Gibb," Non-radiative recombination and Structural Defects in Gallium Phosphide," Inst. Phys. Conf. Ser. No. 33a, p 326-334, 1977.

[75] B. Hamilton and A. R. Peaker," Deep-State-Controlled Minority-Carrier Lifetime in n-type Gallium Phosphide," J. Appl. Phys., Vol. 50, No. 10, p 6373-6385, 1979.

[76] M. O. Watanabe, Y. Ahizawa, N. Sugiyama, and T. Nakanisi," Nonradiative Recombination Process at Deep Levels in AlGaAs Grown by MBE," Inst. Phys. Conf. No. 83, p 105-110, 1986.

[77] P. Petroff and R. L. Hartman," Rapid Degradation Phenomenon in Heterojunction GaAlAs-GaAs Lasers," J. Appl. Phys., Vol. 45, No. 9, p 3899-3903, 1974.

[78] H. Saito and T. Kawakami," The New Origine of Dark-Line Defects in Planar-Stripe DH lasers," IEEE J. Quantum Electron., Vol. QE-13, No. 8, p 564-567, 1977.

[79] C. H. Henry, P. M. Petroff, R. A. Logan, and F. R. Merritt," Catastrophic Damage of $Al_xGa_{1-x}As$ Double-Heterostructure Laser Material," J. Appl. Phys., Vol. 50, No. 5, p 3721-3732, 1979.

[80] H. Imai, T. Fujiwara, K. Segi, M. Takusagawa, and H. Takanashi," Degradation of Optically-pumped GaAlAs Double Heterostructures at Elevated Temperatures," Jpn. J. Appl. Phys., Vol. 18, No. 3, p 589-595, 1979.

[81] G. Bemski,"Quenched-In Recombination Centers in Silicon," Phys. Rev., Vol. 103, No. 3, p 567-569, 1956.

[82] A. Goetzberger and W. Shockley," Metal Precipitates in Silicon p-n Junctions," J. Appl. Phys., Vol. 31, No. 10, p 1821-1824, 1960.

[83] D. K. Sadana," Gettering & Precipitation Phenomena in Semiconductors," Mat. Res. Soc. Symp. Proc., Vol. 36, p 245-255, 1985.

[84] Y. Sugita and M. Tamura," Misfit Dislocations in Bicrystals of Epitaxially Grown on Silicon on Boron-Doped Silicon Substrates," J. Appl. Phys., Vol. 40, No. 8, p 3089-3094, 1969.

[85] P. M. Petroff, in *Semiconductors and Semimetals*, Part A, Vol. 22, Eds. R. K. Willardson and A. C. Beer (Academic Press, Inc, Orlando, San Diego, New York, London, Toronto, Montreal, Sydney, Tokyo, 1985) p 379-403.

[86] P. Petroff and R. L. Hartman," Defect Structure Introduced during Operation of Heterojunction GaAs Lasers," Appl. Phys. Lett., Vol. 23, No. 8, p 469-471, 1973.

[87] B. Monemar, R. M. Potemski, M.B. Small, J. A. Van vechten, and G. R. Woolhouse," Threshold for Optically Induced Dislocation Glide in GaAs-AlGaAs Double Heterostructures: Degradation via a New Cooperative Phenomenon ?," Phys. Rev. Lett., Vol. 41, No. 4, p 260-264, 1978.

[88] D. V. Lang and L. C. Kimerling," Observation of Recombination-Enhanced Defect Reactions in Semiconductors," Phys. Rev. Lett., Vol. 33, No. 8, p 489-492, 1974.

[89] D. V. Lang, P. M. Petroff, R. A. Rogan, and W. D. Johnston," Recombination-Enhanced Interactions between Point Defects and Dislocation Climb in Semiconductors," Phys. Rev. Lett., Vol. 42, No. 20, p 1353-1356, 1979.

[90] J. W. Matthews, A. E. Blakeslee, and S. Mader," Use of Misfit Strain to Remove Dislocations from Epitaxial Thin Films," Thin Solid Films, Vol. 33, p 253-266, 1976.

[91] S. O'Hara. P. W. Hutchinson, and P. S. Dobson," The Origin of Dislocation Climb during Laser Operation," Appl. Phys. Lett., Vol. 30, No. 8, p 368-371, 1977.

[92] P. W. Hutchinson, P. S. Dobson, B. Wakefield, and S. O'Hara," The Generaton of Point Defect in GaAs by Electron-Hole Recombination at Dislocations," Solid-State Electron., Vol. 21, p 1413-1417, 1978.

[93] J. A. Van Vechten," Origin of CW Laser Generated High Efficiency AlGaAs Microstructures," Physica, Vol. 16B, p 575-582, 1983.

[94] A. S. M. Salih, J. S. Ryu, G. A. Rozgonyi, and K. E. Bean," Extrinsic Gettering via Epitaxial Misfit Dislocations: Electrical Characterization," J. Electrochem. Soc., Vol. 133, No. 3, p 475-478, 1986.

[95] A. S. Salih, H. J. Kim, R. F. Davis, and G. A. Rozgonyi," Extrinsic Gettering via the Controlled Introduction of Misfit Dislocations," Appl. Phys. Lett., Vol. 46, No. 4, p 419-421, 1985.

[96] A. S. M. Salih, Z. Radzimski, J. Honeycutt, G. A. Rozgonyi. K. E. Bean, and K. Lindberg," Gated Diode Leakage and Lifetime Measurements of Misfit Dislocation Gettered by Si Epitaxy," Appl. Phys. Lett., Vol. 50, No. 23, p 1678-1680, 1987.

[97] T. J. Garosshen, C. S. Kim, and J. M. Galligan," On the Influence of Light on Dislocation Motion in Compound

Semiconductors," J. Electronic Mat., Vol. 19, No. 9, p 889-894, 1990.

[98] D. K. Schroder in *Semiconductor Material and Device Characterization* (John Wiley & Sons, Inc., New York, 1990) Chapter 2.

[99] D. V. Lang," Deep-level Transient Spectroscopy: A New Method to Characterize Traps in Semiconductors," J. Appl. Phys., Vol. 45, No. 7, p 3023-3032, 1974.

[100] G. L. Miller, D. V. Lang, and L. C. Kimerling," Capacitance Transient Spectroscopy," Ann. Rev. Mater. Sci. p 377-448, 1977.

[101] N. M. Johnson, D. J. Bartelink, R. B. Gold, and J. F. Gibbons," Constant-Capacitance DLTS Measurement of Defect-density Profiles in Semiconductors," J. Appl. Phys., Vol. 50, No. 7, p 4828-4833, 1979.

[102] D. S. Day, M. Y. Tsai, B. G. Streetman, and D. V. Lang," Deep-level-transient Spectroscopy: System Effects and Data Analysis," J. Appl. Phys., Vol. 50, No. 8, p 5093-5098, 1979.

[103] P. D. Kirchner, W. J. Schaff, G. N. Maracas, L. F. Eastman, T. I. Chappell, and C. M. Ransom," The Analysis of Exponential and Nonexponential Transients in Deep-Level Transient Spectroscopy," J. Appl. Phys., Vol. 52, No. 11, p 6462-6470, 1981.

[104] A. S. Grove in *Physics and Technology of Semiconductor Devices*, (John Wiley and Sons, Inc., New York, 1967) p 130.

[105] D. L. Losee," Admittance Spectroscopy of Impurity Levels in Schottky Barriers," J. Appl. Phys., Vol. 46, No. 5, p 2204-2214, 1975.

[106] S. Duenas, M. Jaraiz, J. Vicente, E. Rubio, L. Bailon, and J. Barbolla," Optical Admittance Spectroscopy: A New Method for Deep Level Characterization," J. Appl. Phys., Vol. 61, No. 7, 1987.

[107] T. Ohori, M. Takikawa, and J. Komeno," Frequency Dependence of Capacitance-Voltage characteristics caused by DX Centers in Si-doped AlGaAs," J. Appl. Phys., Vol. 63, No. 4, p 1223-1224, 1988.

[108] S. Subramanian," Frequency Dependence of Response of the DX Center in AlGaAs and its Influence on the Determination of the Band Discontinuity of GaAs/AlGaAs

Heterojunctions," J. Appl. Phys., Vol. 64, No. 3, p 1211-1214, 1988.

[109] M. Beguwala and C. R. Crowell," Characterization of Multiple Deep Level Systems in Semiconductor Junctions by Admittance Measurements," Solid-State Electron., Vol. 17, p 203-214, 1974.

[110] J. L. Pautrat, B. Katircioglu, N. Magnea, D. Bensahel, J. C. Pfister, and L. Revoil," Admittance Spectroscopy: A Powerful Characterization Technique for Semiconductor Crystals - Application to ZnTe," Solid-State Electronics, Vol. 23, p 1159-1169, 1980.

[111] A. R. Peaker and B. Hamilton in *Deep Centers in Semiconductors*, edited by S. T. Pantelides, (Gordon and Breach Science, New York, 1986) p 349-398.

[112] R. A. Smith in *Semiconductors*, (Cambridge Univ. Press 2nd Ed. 1978) p 253

[113] R. K. Ahrenkiel, D. J. Dunlavy, R. Y. Loo, and G. S. Kamath," Minority-Carrier Lifetime in n-$Al_{0.38}Ga_{0.62}As$," J. Appl. Phys., Vol. 63, No. 10, p 5174-5176, 1988.

[114] D. V. Lang," The Role of the Lattice in Deep Levels and Nonradiative Recombinations," J. Phys. Soc. Japan, Suppl. A, Vol. 49, p 215-222, 1980.

[115] R. Englman and J. Jortner," The Energy Gap Law for Radiationless Transitions in Large Molecules," Molecular Phys., Vol. 18, No. 2, p 145-164, 1970.

[116] C. H. Henry and D. V. Lang," Nonradiative Capture and Recombination by Multiphonon Emission in GaAs and GaP," Phys. Rev. B., Vol. 15, No. 2, p 989-1016, 1977.

[117] B. K. Ridley and M. A. Amato," A Model for the Interpretation of Measurements of Photoionization and Capture Cross Sections associate with Deep-Level Impurities," J. Phys. C, Vol. 14. p 1255-1269, 1981.

[118] P. J. Dean, M. S. Skolnick, C. Uihlein, and D. C. Herbert," New Aspect of the Oxygen Donor in Gallium Phosphide," J. Phys. C, Vol. 16, p 2017-2051, 1983.

[119] D. V. Lang and R. A. Rogan," Study of Deep Levels in GaAs by Capacitance Spectroscopy," J. Electronic Mat., Vol. 4, p 1053-1066, 1975.

[120] D. K. Schroder in *Semiconductor Material and Device Characterization* (John Wiley & Sons, Inc., New York, 1990) Chapter 7.

[121] S. M. Sze in *Physics of Semiconductor Devices* (John Wiley & Sons, Inc., New York, 1981) p 101.

Appendix

Appendix A

Derivation of $N_T = \frac{2\,\Delta C}{C}\,(N_D^+ - N_A^-)$

The capacitance per unit area, C(0), at t=0 (i.e., right after the falling edge of the filling pulse) is given by

$$C(0) = \frac{\varepsilon_o \varepsilon_s}{W(0)}$$

where $W(0) = \left[\frac{2\varepsilon_o \varepsilon_s (V_{bi}+V_R)}{q\ N_s}\right]^{1/2}$.

Therefore, $C(0) = \left[\frac{q\ \varepsilon_o \varepsilon_s\ N_s}{2\ (V_{bi}+V_R)}\right]^{1/2}$.

Let $A = \left[\frac{q\ \varepsilon_o \varepsilon_s}{2\ (V_{bi}+V_R)}\right]^{1/2}$, then $C(0) = \sqrt{\frac{N_s}{A}}$.

Likewise, the capacitance per unit area at t=∞, C(∞), is given by

$C(\infty) = \frac{\varepsilon_o \varepsilon_s}{W(\infty)}$, where $W(\infty) = \left[\frac{2\varepsilon_o \varepsilon_s (V_{bi}+V_R)}{q\ (N_s + N_T)}\right]^{1/2}$.

Therefore, $C(\infty) = \sqrt{\frac{N_s+N_T}{A}}$.

If we define $\Delta C = C(\infty) - C(0)$,

then $\Delta C = \sqrt{\frac{N_s+N_T}{A}} - \sqrt{\frac{N_s}{A}}$.

Therefore, $\Delta C = C(0) \left(\sqrt{\frac{N_s+N_T}{A} \cdot \frac{A}{N_s}} - 1 \right)$.

$$= C(0) \left(\sqrt{\frac{N_s+N_T}{N_s}} - 1 \right) = C(0) \left(\sqrt{1+\frac{N_T}{N_s}} - 1 \right) .$$

By binomial expansion,

if $\frac{N_T}{N_s} \ll 1$, then $\left(1 + \frac{N_T}{N_s}\right)^{1/2} \approx 1 + \frac{1}{2} \cdot \frac{N_T}{N_s}$.

Therefore, $\Delta C = C(0) \left(1 + \frac{N_T}{2N_s} - 1\right)$

where $N_s = N_D^+ - N_A^-$ for an n-type semiconductor.

The trap density, N_T, is given by

$N_T = \frac{2\ \Delta C}{C(0)}\ (\ N_D^+ - N_A^-\ )$.

Thus, this formula is valid only for $N_T << (\ N_D^+ - N_A^-)$.